



HAL
open science

A detailed Study of the Seismicity related to a Low-Angle Normal Fault in the Northern Apennines, Italy

David Essing

► **To cite this version:**

David Essing. A detailed Study of the Seismicity related to a Low-Angle Normal Fault in the Northern Apennines, Italy. Earth Sciences. Université Grenoble Alpes [2020-..], 2023. English. NNT : 2023GRALU015 . tel-04204948

HAL Id: tel-04204948

<https://theses.hal.science/tel-04204948>

Submitted on 12 Sep 2023

HAL is a multi-disciplinary open access archive for the deposit and dissemination of scientific research documents, whether they are published or not. The documents may come from teaching and research institutions in France or abroad, or from public or private research centers.

L'archive ouverte pluridisciplinaire **HAL**, est destinée au dépôt et à la diffusion de documents scientifiques de niveau recherche, publiés ou non, émanant des établissements d'enseignement et de recherche français ou étrangers, des laboratoires publics ou privés.

THÈSE

Pour obtenir le grade de

DOCTEUR DE L'UNIVERSITÉ GRENOBLE ALPES

École doctorale : STEP - Sciences de la Terre de l'Environnement et des Planètes

Spécialité : Sciences de la Terre et de l'Environnement

Unité de recherche : Institut des Sciences de la Terre

Etude détaillée de la sismicité liée à une faille normale à bas angle dans les Apennins du Nord de l'Italie

A detailed Study of the Seismicity related to a Low-Angle Normal Fault in the Northern Apennines, Italy

Présentée par :

David ESSING

Direction de thèse :

Michel CAMPILLO

Professeur, UGA

Piero POLI

CNRS

Directeur de thèse

Co-encadrant de thèse

Rapporteurs :

Olivier LENGLINE

MAITRE DE CONFERENCES HDR, Université de Strasbourg

Thomas FISCHER

PROFESSEUR, Univerzita Karlova v Praze

Thèse soutenue publiquement le **12 mai 2023**, devant le jury composé de :

Michel CAMPILLO

PROFESSEUR DES UNIVERSITES, Université Grenoble Alpes

Patricia GARZON MARTINEZ

DOCTEUR EN SCIENCES, German Research Centre for Geosciences

Olivier LENGLINE

MAITRE DE CONFERENCES HDR, Université de Strasbourg

Anne SOCQUET

PHYSICIEN, Université Grenoble Alpes

Thomas FISCHER

PROFESSEUR, Univerzita Karlova v Praze

Elisa TINTI

PROFESSEUR ASSOCIE, Università di Roma

Directeur de thèse

Examinatrice

Rapporteur

Présidente

Rapporteur

Examinatrice

Invités :

Piero POLI

PROFESSEUR ASSISTANT, University of Padova





Charte anti-plagiat

Art 1 : Définition du plagiat

Le plagiat consiste à reproduire un texte, une partie d'un texte, une illustration ou des idées originales d'un auteur, sans lui en reconnaître la paternité par un référencement bibliographique ou iconographique adéquat (Cf. art. 3).

Art 2 : Objet des travaux universitaires

Sont considérés comme travaux universitaires tous les documents réalisés par les étudiants et les enseignants, les chercheurs et les enseignants-chercheurs dans le cadre des activités de formation et de recherche. Ces travaux universitaires doivent toujours avoir pour ambition de produire un savoir inédit et d'offrir une lecture critique, nouvelle et personnelle du sujet.

Art 3 : Méthodologie de référencement bibliographique

La méthodologie d'un travail universitaire implique que les emprunts (par exemple par copier/coller) soient clairement identifiés et que le nom de l'auteur et la source de l'extrait soient mentionnés.

Les citations textuelles y compris dans une traduction personnelle, doivent obligatoirement être placées entre guillemets et être accompagnées d'une référence bibliographique à la suite de la citation, ou en note de bas de page.

Les emprunts non textuels (tableaux, graphiques, photos, formules scientifiques, etc.) doivent également être accompagnés d'une référence bibliographique à leur suite ou en note de bas de page.

En complément, toutes les références des documents cités, empruntés ou adaptés, doivent figurer en bibliographie.

Art 4 : Détection du plagiat

L'Université Grenoble Alpes est dotée d'un outil permettant de contrôler systématiquement les travaux universitaires et de détecter les similitudes, dans le but de rechercher le plagiat.

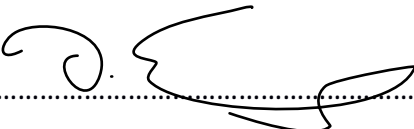
Art 5 : Sanctions disciplinaires pour plagiat

Les auteurs présumés de plagiat seront traduits devant la section disciplinaire compétente qui pourra prendre des sanctions pouvant aller jusqu'à l'exclusion définitive de tout établissement d'enseignement supérieur. La procédure disciplinaire n'exclut pas d'éventuelles poursuites judiciaires.

Art. 6 : Engagement

Les étudiants et les personnels s'engagent à ne pas commettre de plagiat dans leurs travaux universitaires. À cette fin, ils reconnaissent avoir pris connaissance des obligations décrites dans les articles 2 et 3 de la présente charte et s'engagent à s'y conformer.

Je certifie, Essing David(indiquer nom prénom)
avoir pris connaissance de la charte anti-plagiat et à la respecter.

Date et signature : 10.03.2023 

*“When you come here and I’m wasted
Lying on a field, dancin’ in the rain
Hidin’ in the back, loosening my grip
Wading in the water
Just trying not to crack, under the pressure”*

The War on Drugs

UNIVERSITÉ GRENOBLE ALPES

Abstract

A detailed Study of the Seismicity related to a Low-Angle Normal Fault in the Northern Apennines, Italy

by David ESSING

In extensional tectonic settings, where the brittle crust is pulled apart, normal faults with a dip angle below 30° , called low-angle normal faults (LANF), are geologically well recorded. They are thought to be responsible for accommodating large portions of the crustal extension. While in recent decades extensively studied at different places around the globe, basic questions regarding LANFs remain unanswered. For example, the precise way extension is accommodated, whether via slow deformation directly along the surface of the LANF or along high-angle faults in its hanging wall, is still debated. A related question is whether LANFs have the capacity to produce large earthquakes.

A well-studied LANF is the Alto Tiberina Fault in the Northern Apennines (Italy). The surface of the LANF is highlighted by continuous radiation of micro-seismicity. Above the LANF, within its hanging wall (HW), a network of syn- and antithetic high-angle faults frequently hosts transient swarm seismicity. In recent decades, a dense network of multi-parametric sensors (GNSS, seismic) was installed within the region which provides high-quality measurements.

In this work, I will leverage the high-resolution data offered by the dense network to help address the questions posed above. In chapter 3, I will apply a matched-filter approach to obtain a high-resolution earthquake catalog which is analysed from different perspectives. In the HW, the analysis reveals time periods of increased spatial- and temporal clustering during an aseismic deformation event. This reflects the heterogeneous evolution of aseismic slip together with the complexity of the shallow fault system. Along the LANF, seismicity occurs in a bimodal behavior, with diffuse seismicity active continuously, and intermittent bursts. Moreover, indication for repeating earthquakes (REs) is found in the extended catalog, which appears to be difficult to reconcile with a simple creep model based on a preliminary analysis.

In order to automatically extract meaningful information of the high-resolution earthquake catalog, in chapter 4, I use the space and time information of the detected seismicity and apply unsupervised clustering methods. This helps to find and extract earthquake clusters that are related to seismic bursts. A quantitative analysis of the seismic bursts indicates that the overall swarm of the HW could be composed of spatially and temporally confined (sub) events of aseismic slip.

Finally, in chapter 5, I reassess the REs found in chapter 3. The relocated REs and their refined source parameters reveal event clusters with short interevent times, difficult to reconcile with creep as a driving mechanism. Therefore I propose an alternative mechanisms to match the observations.

The thesis reveals that other mechanisms than slow deformation along the LANF could be responsible for accommodating the extension within the study area. Indeed, findings indicate that some parts of it could be released along high-angle normal faults within the shallow HW, which is in agreement with alternative models.

UNIVERSITÉ GRENOBLE ALPES

Résumé

Une étude détaillée de la sismicité reliée à une faille normale de bas angle dans les Apennins du Nord, Italie.

de David ESSING

Dans les contextes tectoniques d'extension, où la croûte se sépare et brise, on peut trouver des registres géologiques concernant les failles normales avec un angle de pendage inférieur à 30° , appelées failles normales à bas angle (LANF en anglais). Le consensus général est que ces failles accueillent une grande partie de l'extension de la croûte terrestre. Bien qu'elles ont été l'objet d'études intensives au cours des dernières années dans différents contextes géologiques, les questions fondamentales par rapport aux LANF restent d'actualité. Par exemple, il y a encore un débat par rapport à la manière précise dont l'extension est prise en compte, soit en forme de déformation lente subie directement au long de la surface du LANF, soit en forme de failles inverses secondaires dans l'éponte supérieure. Une question associée est de savoir si les LANF ont la capacité de produire de grands séismes.

La faille de l'Alto Tiberina, dans les Apennins du Nord (Italie), est une LANF bien étudiée. La surface de la LANF est bien décrite par sa production en continu de micro-sismicité. Au-dessus du LANF, dans l'éponte supérieure (HW en anglais), un réseau de failles syn- et antithétiques à angle élevé héberge fréquemment une sismicité transitoire en essaims. Au cours des dernières décennies, un réseau dense de capteurs multiparamétriques (GNSS, sismique) a été installé dans la région et fournit des mesures de haute qualité.

Dans ce travail de thèse, j'exploite les données à haute résolution produites par ce réseau dense pour essayer de répondre aux questions posées ci-dessus. Dans le chapitre 3, j'applique une approche par filtres-adaptés pour obtenir un catalogue à haute résolution de séismes qui sera analysé sous différents aspects. Dans le HW, l'analyse révèle des périodes d'augmentation des regroupements spatiaux et temporels lors d'un événement de déformation aisé. Cela correspond à l'évolution hétérogène du glissement aisé et la complexité du système de failles peu profondes. Tout au long du LANF, la sismicité a un comportement bimodal, avec une sismicité diffuse active en continu et des épisodes intermittents de fortes intensités. De plus, on trouve dans le catalogue élargi des pistes montrant des séismes répétitifs (REs), ce qui semble difficile à concilier avec un modèle de déplacement simple basé sur une analyse préliminaire.

Afin d'extraire automatiquement des informations significatives du catalogue à haute résolution, au chapitre 4, j'utilise les informations spatiales et temporelles de la sismicité détectée et j'applique des méthodes de re-groupement non supervisées. Cela permet de trouver et d'extraire des groupes de séismes liés aux essaims sismiques. L'analyse quantitative des essaims sismiques indique que l'essaim général du HW pourrait être composé de (sous) événements de glissement aisé limités dans l'espace et dans le temps.

Finalement, dans le chapitre 5, je réévalue les REs trouvés dans le chapitre 3. Les REs relocalisés et les paramètres de source améliorés révèlent des groupes d'événements avec des temps inter-événements courts difficiles à expliquer avec le fluage comme mécanisme moteur. C'est pourquoi je propose un mécanisme alternatif pour répondre aux observations.

La thèse révèle que d'autres mécanismes à part la déformation lente au long du LANF pourraient être à l'origine de l'extension dans la zone d'étude. En effet, les résultats indiquent que certaines déformations pourraient être libérées au long de failles normales avec des angles élevés dans le HW peu profond, ce qui est en accord avec d'autres modèles.

Acknowledgements

After three years filled with a mosaic of experiences—embracing both moments of elation and those of challenge—it is time to thank the people that made this adventure possible.

First and foremost, my deep gratitude goes to the members of the jury that took their time to attend my PhD defense: Tomáš Fischer, Olivier Lengliné, Anne Socquet, Elisa Tinti, and Patricia Martínez-Garzón. Your commitment evaluating this work, engaging in thoughtful discussions, and offering constructive feedback has been pivotal. I am genuinely thankful for your involvement on that special day.

I would like to express my sincere appreciation to my supervisor, Piero Poli. The profound learning and developing experience under your guidance has deeply impacted my way of thinking. Your mentorship, coupled with your ability to push boundaries, has been fundamental for my growth throughout this adventure.

In addition, I extend thanks to Michel Campillo for his time and interest over these three years. Our discussions have been enlightening and have added a layer of depth to my research.

David Marsan and William Frank, your willingness to engage in discussions and offer valuable advice have been truly invaluable.

To the broader ISTERre community, your support has played an essential role in my journey. The collaborative environment, coupled with the assistance I've received, has created an atmosphere that has enabled my progress.

Among the many kind-hearted individuals at ISTERre, I want to mention Josipa, Nour, Leoncio, Hugo, René, Peidong, Malcom, and Gino. Our interactions, whether they were walks, conversations, or shared breaks, have made this journey memorable.

To my family, who stood by me through challenges, your unwavering encouragement has been a source of motivation. Especially the difficulties of the past years have been made manageable by your presence.

Lastly, my deepest and most heartfelt gratitude goes to Melina, whose boundless patience and unwavering positivity have made this journey something very special. Your unending support and belief in me have been a driving force throughout these years.

Contents

Abstract	v
Résumé	vii
Acknowledgements	ix
1 Introduction	1
1.1 Study Area and Tectonic Background	1
1.2 Low-angle normal faults	4
1.2.1 General Introduction	4
1.2.2 The Alto Tiberina Fault	5
1.3 Seismicity along LANFs	8
1.3.1 General Types of Seismicity	8
1.3.2 Seismicity within the Study Area	10
Hanging Wall	10
LANF	10
1.3.3 The Alto Tiberina Near Fault Observatory	11
1.4 Open questions	12
2 Methods	15
2.1 Detecting Earthquakes	15
2.1.1 Traditional Methods	15
2.1.2 Matched-Filter Approach	16
2.2 Clustering	19
2.2.1 Earthquake clustering	19
2.2.2 Clustering in a General Way	20
Hierarchical Methods	21
Density based Methods	22
Clustering using HDBscan	22
3 Spatiotemporal Evolution of the Seismicity in the Alto Tiberina Fault System	27
3.1 Introduction	28
3.2 Detection of Seismicity	29
3.3 The Extended Seismic Catalog	32
3.4 Time and Space Evolution of the Seismicity	34
3.4.1 Time and Space Clustering of the Seismicity	36
3.4.2 Temporal Behavior of Template Families	38
3.4.3 Repeating Earthquakes (RE) Along the LANF	40
3.5 Discussion	41
3.5.1 The Shallow Seismicity	42
3.5.2 The Deep Seismicity	43
3.6 Conclusion	45

4	Swarms as a Cascade of Aseismic Transients	47
4.1	Introduction	48
4.2	Seismo-Tectonic Setting	50
4.3	Spatiotemporal Hierarchical Clustering	51
4.3.1	Clustering	51
4.3.2	Feature Preparation	54
4.4	Results	55
4.4.1	Separating Clustered Seismicity from the Background	55
4.4.2	Size and Duration of Seismic Bursts	56
4.4.3	Time Evolution of the Seismic Moment and Triggering of Seismicity	59
4.5	Discussion	62
4.6	Conclusion	64
5	Fast Reoccurring, Repeating Earthquakes	65
5.1	Introduction	66
5.2	Identification of Repeating Earthquakes	66
5.3	Estimation of Slip	69
5.4	Approximating the Fluid Pressure	72
5.5	Discussion	73
5.6	Conclusion	75
6	Conclusions & Outlook	77
6.1	Final Conclusion	77
6.2	Outlook	78
6.2.1	Automated Clustering of Large Seismic Catalogs	78
6.2.2	Combine GNSS Data with Seismic Catalogs	79
6.2.3	2023 Umbertide Sequence	80
A	Supporting Information for Chapter 3	83
B	Supporting Information for Chapter 4	91
C	Supporting Information for Chapter 5	101
D	Supporting Information for Chapter 6	107
	Bibliography	119

List of Figures

1.1	Simplified tectonic map of Italy and surrounding areas.	2
1.2	Map of the study area	3
1.3	Schematic figure of seismicity and geodetic measurements in the Gulf of Corinth	6
1.4	Combined Coulomb-Griffith diagram	7
1.5	Mainshock-aftershocks and swarm sequences	9
2.1	Pipeline of the matched-filter approach	17
2.2	Nearest-neighbor distances	20
2.3	Hierarchical clustering pipeline	23
2.4	Density-based clustering	24
2.5	HDBscan clustering pipeline	26
3.1	The study area in Italy	30
3.2	Waveforms of detected and template events	33
3.3	Time and space-time evolution of the seismicity	35
3.4	Magnitudes of the detected seismicity	37
3.5	Pairwise cross-correlation between event count time series	39
3.6	Interevent times of the detected seismicity	41
3.7	Locations and durations of detected families of similar events	43
4.1	The study area in Italy	49
4.2	HDBscan clustering pipeline	53
4.3	Overall and clustered seismicity	56
4.4	Clustered seismicity in space and time	58
4.5	Scaling properties of the extracted bursts.	59
4.6	Seismic moment of the bursts	60
4.7	Temporal evolution of the bursts	62
5.1	The study area in Italy	67
5.2	Waveforms of repeating earthquakes in the time and frequency domain	70
5.3	Slip rate and pore-fluid pressure change rate	73
5.4	Conceptual model to explain rapid repeating earthquakes	75
6.1	Combining seismic and GNSS data	80
6.2	Space and space-time evolution of the seismicity	81

Chapter 1

Introduction

1.1 Study Area and Tectonic Background

This research is going to focus on the seismicity along a specific section of Italy's Northern Apennines (Figure 1.1). To comprehend this seismicity, it is essential to understand the tectonic processes that formed the Italian peninsula and its mountain ranges in the past and the present.

The tectonic setting of the Italian peninsula is related to the convergence of the Eurasian and the Adriatic promontory of the African plate (Palano, 2015; Pauselli et al., 2006). This initially caused the formation of the Alps, followed by the formation of the Apennines and eventually led to the opening of the Tyrrhenian Sea (Jolivet et al., 1998).

The Alps formed due to the N-S convergence of the Eurasian and African plates, which began in the early Cretaceous (145 Ma) and continues to be currently ongoing (Palano, 2015).

The Apennines fold-and-thrust belt is thought to have formed as a result of the collision of the Adriatic lithosphere with the European continental margin (Sardinia-Corsica block), resulting in two distinct phases of deformation (Pauselli et al., 2006).

The first phase started in the Late Oligocene Early Miocene (23 Ma) and is dominated by compressional deformation, due to the westward subduction of the Adriatic-Ionina lithospheric slab (Palano, 2015). The compression gradually migrated from west to east and was accommodated by folding as well as slip on developed thrust faults. There is an ongoing debate about whether this period of deformation is still active in the eastern part of the Northern Apennines along the Romagna-Adriatic front (Di Bucci and Mazzoli, 2002; Frepoli and Amato, 1997).

The second period started during the Middle Miocene (15 Ma), with the opening of the Tyrrhenian Sea, that generated extensional deformation. This extensional deformation again propagated eastwards throughout time, starting from the Corsica Basin close to the Sardinia-Corsica Block (Figure 1.1) and is nowadays active along the axial part of the Northern and Central Apennines in the border region of Umbria and Marche (Pauselli et al., 2006).

The ongoing extension within the axial part of the Northern and Central Apennines at rates of mm/yr is mainly accommodated by slip along normal faults (Palano, 2015) and makes these regions among the most seismically active in Europe (Figure 1.1). In this part of Italy, the strongest historical (Boschi, 1998), as well as instrumental earthquakes are found such as the $M_w = 6.1$ 2009 in L'Aquila (Cabrera, Poli, and Frank, 2022; Chiaraluce et al., 2011), or the 2016 Central Italy earthquake sequence consisting of several $M_w > 5.9$ earthquakes (Chiaraluce et al., 2017).

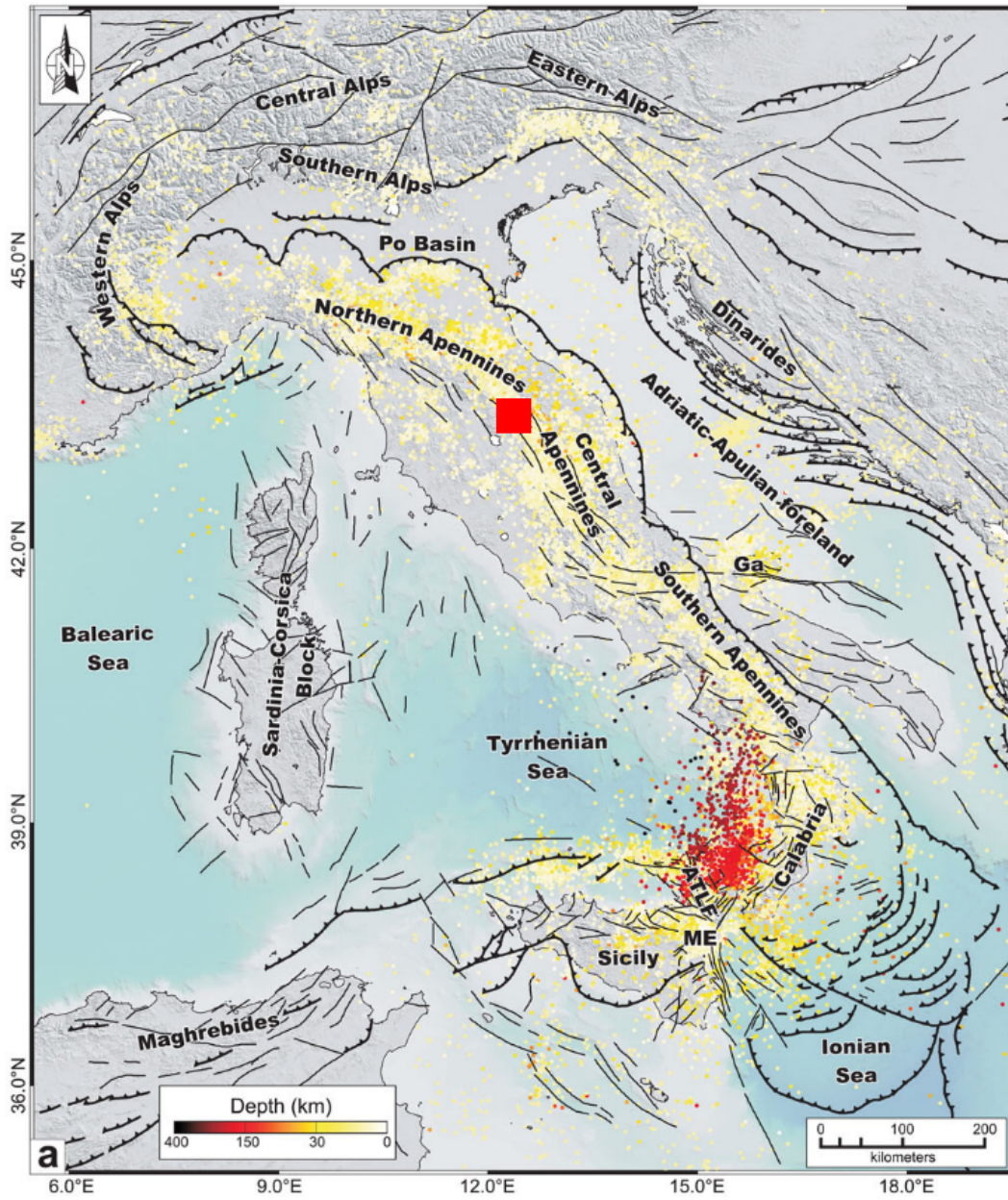


FIGURE 1.1: Simplified tectonic map of Italy and surrounding areas. The instrumental seismicity ($M > 2.5$) since 1983 is indicated for different depths. The study area of this thesis is highlighted by the red rectangle. Modified from Palano, 2015.

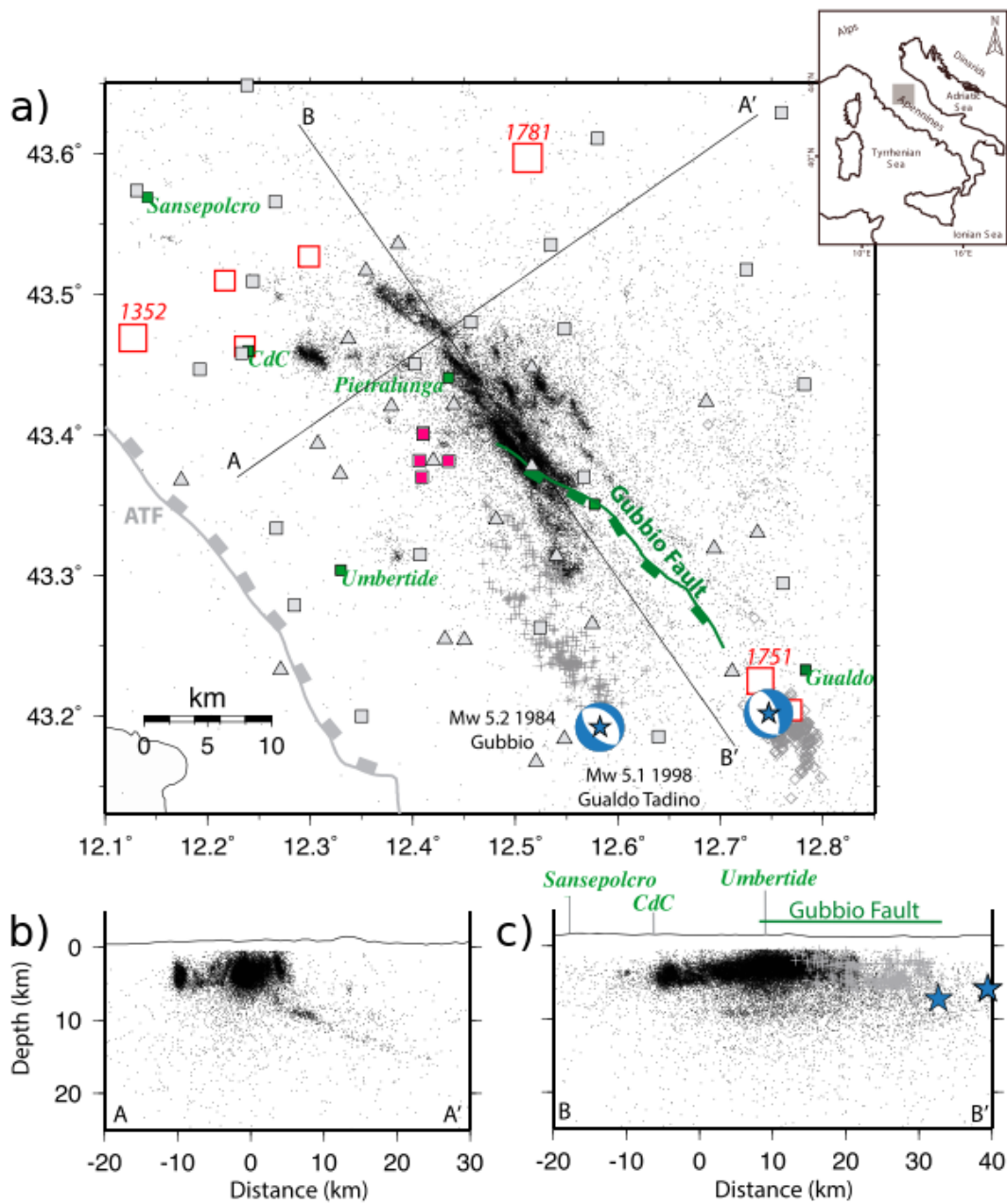


FIGURE 1.2: (a) Map of the study area. Black dots indicate the locations of $\sim 44,000$ earthquakes recorded from April 2010 to September 2014 (Valoroso et al., 2017). The pink squares are borehole seismic stations (Chapter 3), grey squares are permanent stations (Chapter 5), and the triangles are temporary stations of the TABOO seismic network (Chiaraluce et al., 2014). Red squares represent the location and size of the largest historical events occurred in the past 1,000 years (Rovida et al., 2011). The locations of the largest instrumental earthquakes (i.e., 1984 M_w 5.2 Gubbio and 1998 M_w 5.1 Gualdo Tadino) are indicated with blue stars and their focal mechanisms (Dziewonski, Franzen, and Woodhouse, 1985; Pondrelli et al., 2002). The grey and green lines are the surface projections of the Alto Tiberina and the Gubbio fault (Mirabella et al., 2011). (b) Cross-section, following the A-A' line in (a). (c) As (b), but following the B-B' line. Modified from Valoroso et al., 2017.

Nevertheless, from figure 1.2 which is based on historic earthquake catalogs, it appears that not all areas undergoing extensional deformation along the axial section of the Northern and Central Apennines have hosted $M > 6$ earthquakes (Deschamps, Scarpa, and Selvaggi, 1989; Piccinini et al., 2003). In an area that is bounded by the surface projection of the Alto Tiberina fault (ATF) and the Gubbio fault and the town of Pietralunga, there is no evidence for historical nor instrumental large earthquakes (Chiaraluce et al., 2007; Deschamps, Scarpa, and Selvaggi, 1989; Piccinini et al., 2003), despite there are surface traces of normal faults and an increased number of micro-seismicity (Chiaraluce et al., 2007; Valoroso et al., 2017). Therefore, the extension within this distinct area must be accommodated with mechanisms other than seismic slip (i.e., slip that radiates seismic energy) during moderate-to-large earthquakes.

And indeed, the inversion of GNSS data recorded within the study region have shown that extension could be accommodated via aseismic deformation, either along a low-angle normal fault (LANF; Anderlini, Serpelloni, and Belardinelli, 2016) or along high-angle normal faults within the hanging wall (HW) of the LANF (Gualandi et al., 2017). Furthermore, Lambotte et al. (2014) proposed a model for a region with a similar seismic activity and GNSS signals that uses a hypothetical non-elastic body at depth below the rift axis that would focus strain to the shallow parts of their study area (Chapter 1.2).

Even though, the area does not show evidence for moderate-to-large earthquakes, abundant micro-seismicity with a constant (Valoroso et al., 2017; Essing and Poli, 2022) to semi-constant rate (Vuan et al., 2020) along the LANF (Chapter 1.2) is found and could indicate the manifestation of a quasi-continuously active mechanism (Anderlini, Serpelloni, and Belardinelli, 2016; Collettini, 2011). The HW of the LANF on the other hand, shows reoccurring swarm seismicity which could be the manifestation of an intermittent driving mechanism (Chapter 1.3, Gualandi et al., 2017).

1.2 Low-angle normal faults

1.2.1 General Introduction

Faults with dip angles smaller than 30° , nowadays known as low-angle normal faults or extensional detachments, were first discovered almost one century ago in the United States' Basin and Range province (Longwell, 1945; Ransome, Emmons, and Garrey, 1910). Since then, they have been further studied in the Basin and Range province (Anderson, 1971; Wernicke, 1981), with new discoveries made in the Gulf of Corinth in Greece (Rietbrock et al., 1996), Mai'iu in Papua New Guinea (Abers, Mutter, and Fang, 1997; Biemiller et al., 2020), and the Apennines in Italy (Chiaraluce et al., 2007), among other locations (Collettini, 2011). Within these extensional regimes, LANFs are proposed to be key-structures to accommodate and release extensional stress (Collettini and Holdsworth, 2004; Jolivet et al., 2010)

According to Collettini (2011), the fault structure of LANFs can range from a relatively thick (0.5 – 5km) shear zone consisting mainly of mylonitic rocks (e.g., Whipple LANF (Davis, Lister, and Reynolds, 1986), South Mountains LANF (Davis, Lister, and Reynolds, 1986), or the Tinos LANF (Jolivet et al., 2010)) to a discrete fault core of several meters thickness, characterised by small fractures and veins like the Zuccale LANF (Collettini and Holdsworth, 2004).

Numerous LANFs at shallow crustal depth exhibit fault gouges or foliated catclasites composed of sub-rounded quartz, feldspar, and carbonate clasts in a heterogeneous fine-grained matrix (Collettini, 2011). Deformation could be accommodated internally by rolling and sliding grains alongside one other (Hayman, 2006; Smith et al., 2011). The rolling and sliding would additionally powder the grains, that therefore could potentially act to channel fluids from larger depths (Collettini, 2011).

As initially said, LANFs are found in regimes of active tectonic extension, where the maximum principle stress (i.e., the largest normal stress σ_1) follows the vertical direction. While proposed as key-structures for accommodating significant amounts of the resulting stress in extensional regimes (Collettini and Holdsworth, 2004; Jolivet et al., 2010), there is still a debate on how this exactly occurs in nature. Therefore, several models are proposed (Anderlini, Serpelloni, and Belardinelli, 2016; Briole et al., 2000; Cianetti et al., 2008; Lambotte et al., 2014; Le Pourhiet, Burov, and Moretti, 2003; Rigo et al., 1996).

In one model the extensional stress is partially released by stationary deformation along the LANF detachment (Anderlini, Serpelloni, and Belardinelli, 2016; Rigo et al., 1996). Figure 1.3a shows the illustration of the model, that is supported by the inversions of GNSS velocities measured at a station network installed in the vicinity of the ATF (Anderlini, Serpelloni, and Belardinelli, 2016) and the Gulf of Corinth (Briole et al., 2000).

Contrary to that model, Lambotte et al. (2014) argue that a non-elastic body at depth could concentrate the spatial distribution of elastic strain upwards, leading to similar GNSS measurements at the surface (Figure 1.3b). The latter model would result only in relatively small to non existing deformation along the LANF interface (Lambotte et al., 2014).

While the presented models are able to explain the surface displacement, we will see in chapter 1.3 that difficulties remain explaining the abundant seismicity radiated from different LANFs (Abers, Mutter, and Fang, 1997; Biemiller et al., 2020; Collettini, 2011; Briole et al., 2000). This difficulties arises because the well-established Anderson-Byerlee frictional fault reactivation theory predicts that in an extensional regime (i.e., σ_1 in vertical direction) with a coefficient of friction (μ_s) of 0.6 – 0.85 (Byerlee, 1978), initiating a new fault with a dip angle $> 30^\circ$ is more convenient than reactivating an existing fault with a dip angle $< 30^\circ$ (Collettini and Sibson, 2001; Sibson, 1985).

1.2.2 The Alto Tiberina Fault

A well-studied LANF is the Alto Tiberina Fault (ATF) in the Northern Apennines in Italy (Figure 1.2). Located within the tectonically active extensional part of the Apennines, the fault system is thought to accommodate large portions of the overall tectonic extension of ~ 3 mm/yr within the region (Anderlini, Serpelloni, and Belardinelli, 2016; Serpelloni et al., 2005).

The structure of this fault is well characterized by several seismological studies, as deep seismic reflection profiles (Barchi, 1998), controlled source seismic imaging (Mirabella et al., 2004), and seismic tomography (e.g., Chiarabba and Amato, 2003; Pauselli et al., 2006; Piana Agostinetti, Giacomuzzi, and Chiarabba, 2017). Further studies characterized the ATF using gravitational (Boncio, Brozzetti, and Lavecchia, 2000), magnetic (Collettini and Barchi, 2002), and heat flow measurements (Mirabella et al., 2004). These studies reveal a 60 km, NNW trending major

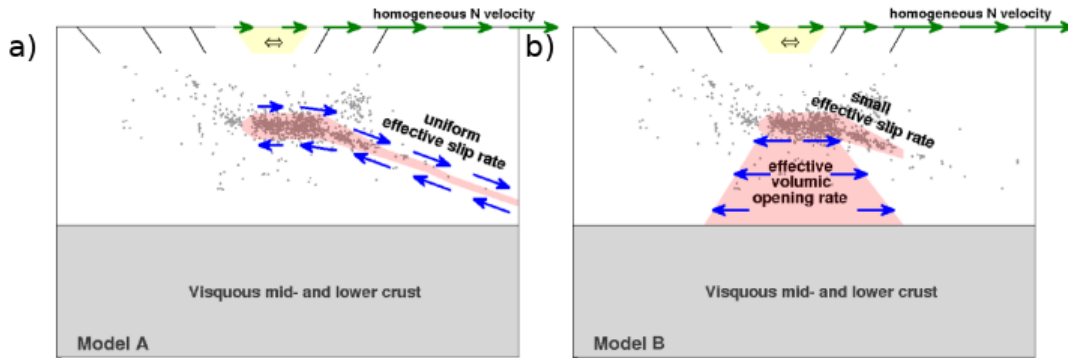


FIGURE 1.3: Schematic figure of detected seismicity and geodetic measurements (green arrows) in the Gulf of Corinth that can be explained by the following two conceptual models: (a) exhibits a model with uniform slip on the surface of the detachment, (b) model with a non-elastic body below the rift axis. High angle faults within the shallow part of the study area are shown by black lines. Modified from Lambotte et al., 2014.

fault that dips $15^\circ - 20^\circ$ from the surface to 12 – 14 km depth (Chiaraluce et al., 2007).

Because direct information of the geology and other characteristics of the ATF is sparse and could only be retrieved at boreholes (Mt. Civitello and San Donato), the Zuccale LANF, which is part of the same fault system, serves as an exhumed equivalent to the ATF (Collettini, 2011).

The Zuccale LANF was formed 13 Ma, under a regional stress field with vertical σ_1 when the extensional deformation (Chapter 1.1) was active in an area farther west to the location of the ATF (Collettini, De Paola, and Gouly, 2006). The analysis of the exhumed analogue indicates a highly strained fault core with a complex network of hydro-fractures probably caused by cyclic build-up and release of over-pressure (Collettini, De Paola, and Gouly, 2006), as well as a small frictional coefficient of $\mu_s \sim 0.2$ for the weak portion of the fault gouge (Collettini et al., 2011).

Along the ATF, Chiaraluce et al. (2007) discovered considerable micro-seismicity radiated within a 500 – 1000 m thick fault zone below 4 km depth. It was first discovered at a constant rate (Chiaraluce et al., 2007), although a more recent study has indicated a variable rate along shallow portions of the LANF (Vuan et al., 2020), which may be related to deformation (Gualandi et al., 2017) and swarm activity in the hanging wall (Valoroso et al., 2017).

Possible mechanisms that are able to explain the seismicity along the LANF could be related to aseismic deformation (Anderlini, Serpelloni, and Belardinelli, 2016). However also the reported fluids (Chiodini and Cioni, 1989) within the study area must be considered to built potential models, which validity has impact on the seismic risk of the study area.

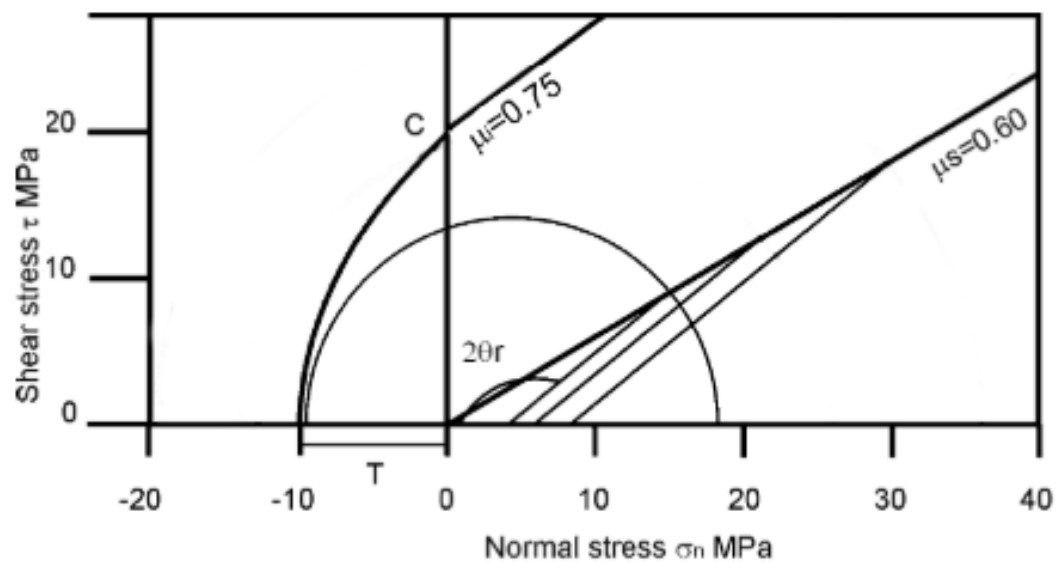


FIGURE 1.4: Combined Coulomb-Griffith diagram of shear stress τ against normal stress σ_n . Plot indicates the required differential stress ($\sigma_1 - \sigma_3$) necessary for the reactivation of the Alto-Tiberina fault ($\theta_r = 70^\circ$, obtained from $90^\circ - 20^\circ$ with $20^\circ =$ dip angle of ATF) for the re-shear condition ($\mu_s = 0.6$) plotted for a pore fluid factor $\lambda_v = 0.94$. Smaller values for the pore fluid factor λ_v would increase the radius of the Mohr-Circle which would therefore either intercept the Griffith parabola (leading to extensional fractures) or the Coulomb criterion (leading to the formation of a new fault). Modified from Collettini and Barchi, 2002.

1.3 Seismicity along LANFs

As we have seen in the former section, several scenarios exist to explain the way extension is accommodated and released along LANFs. Evidence for the presented scenarios was mainly coming from GNSS measurements. Another way to shed light on the mechanisms is to look into the seismicity that is radiated from a LANF system.

1.3.1 General Types of Seismicity

The seismicity within a given region consists basically of two types (Gardner and Knopoff, 1974). The first type of seismicity is the background seismicity, which happens randomly within the region and at random times. The mechanism leading to this type of seismicity is thought of being related to large tectonic processes (Hainzl and Ogata, 2005).

Contrary to the first type, the second type of seismicity is clustered in space and time. Therefore, there should be a direct relationship causing the occurrence of events in a constrained period of space and time. Clustered seismicity can be further separated into two categories.

The first type of clustered seismicity is caused by a large magnitude event, resulting from the background seismicity. This large magnitude event modifies the nearby stress field (Freed, 2005), triggering follow-up seismicity that is smaller in terms of magnitude. The largest earthquake is called a mainshock, while the following, triggered earthquakes are called aftershocks. The ensemble of the mainshock together with its aftershocks (i.e., the sequences) is then called a mainshock-aftershocks sequence (MS-AS). Besides stress transfer triggering (Freed, 2005), additional mechanisms exist to trigger aftershocks such as post-seismic relaxation (Perfettini and Avouac, 2004) or fluid over-pressure (Miller et al., 2004).

Aftershock behaviour can be described with different empirical laws (Båth, 1965; Utsu, Ogata, et al., 1995). For example, according to Båth (1965), the difference in magnitude between the mainshock and the largest aftershock is found to be larger than 1 or 1.4 magnitudes, as seen in figure 1.5. Additionally, the exponential decay of the aftershock rate as a function of time (Figure 1.5c) can be described by the Omori-Utsu law (Utsu, Ogata, et al., 1995).

The second type of clustered seismicity is called an earthquake swarm and generally defined as sequences of - relative to the background rate - increased seismicity rate within a certain area, a short time interval, and no influential dominating earthquake (Mogi, 1963). Other characteristics that identify swarms from MS-AS include the migration of the seismicity over time, large spatial extent of swarms compared to their overall seismic moment, or a weak correlation between the number of events and the largest magnitude in a swarm (Bachura et al., 2020; Passarelli et al., 2018; Vidale and Shearer, 2006).

While studying a swarm of about a hundred events felt in western Bohemia in January-February 1824, Austrian geologist Josef Knett (1899) introduced the German term 'Schwarmbeben', which translates as earthquake swarm. Based on laboratory measurements and seismicity patterns in Japan, Mogi (1963) proposed that, whereas mainshock-aftershock earthquake sequences occur in homogeneous regions with uniform stress fields, swarm sequences are limited to regions with an exceptionally heterogeneous distribution of material properties and stress concentrations. These properties lead to a lack of a single, well-developed fault plane, capable of sustaining higher strain that allows to eventually rupture into a larger earthquake (Mogi,

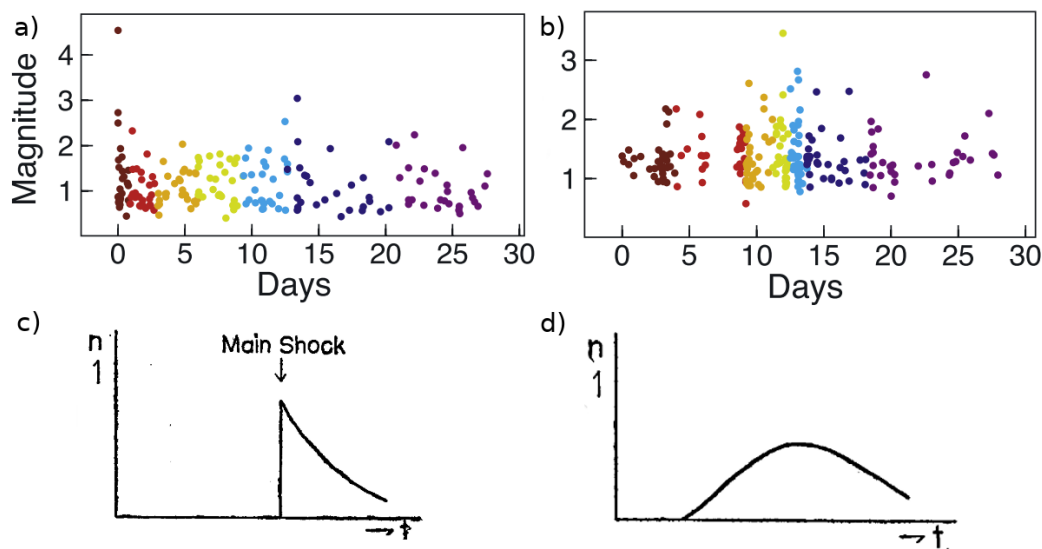


FIGURE 1.5: Magnitude as a function of time for a (a) mainshock-aftershocks sequence and (b) swarm like sequence. Modified from Vidale and Shearer, 2006. Sketch of the seismicity rate (n) as a function of time (t) for a (c) mainshock-aftershocks sequence and (d) swarm like sequence. Modified from Mogi, 1963.

1963). Scholz (1968) confirmed the correlation between swarm-like sequences and material heterogeneities with additional laboratory experiments.

In the last century, swarms were discovered in various tectonic environments such as areas of recent volcanism (Hill, 1977), ocean ridges (Roland and McGuire, 2009) and human induced activity (Schoenball and Ellsworth, 2017). Therefore, different types of mechanisms driving the seismicity have been proposed.

Intraplate swarms, such as encountered within the study area have been found in the Vogtland, a border region between Germany and Czech Republic (Fischer et al., 2014), the Gulf of Corinth in Greece (Duverger et al., 2018), Western Alps in the border region of Italy and France (Beaucé et al., 2019), and within the Apennines (Piccinini et al., 2003; Valoroso et al., 2017), among others.

Swarms in extensional regimes like in Greece and Italy might be linked to tectonic processes of extension (Lambotte et al., 2014; Gualandi et al., 2017). Different mechanisms that could drive the related seismicity in these regions have been proposed. For example, pore-fluid pressure diffusion could lower the effective normal stress on the rupture plane which leads to the migration and expansion of rupture patches (Shapiro, Huenges, and Borm, 1997). Radiation of seismicity could also be due to direct hydraulic fracturing (Hainzl, Fischer, and Dahm, 2012). However, also slow-slip events or aseismic creep could be responsible for seismicity by redistributing elastic stress throughout a large fault region (Peng and Gomberg, 2010). The latter mechanism could be itself also driven by over-pressurized fluids (Guglielmi et al., 2015).

As demonstrated, in recent years during the increased use of fluid injection for geothermal projects (Kwiątek et al., 2019), hydraulic fracturing in shale formations (Schoenball and Ellsworth, 2017) and wastewater disposal (Goebel et al., 2016), human activity can also generate clustered seismicity.

1.3.2 Seismicity within the Study Area

Within the study area, seismicity can be found at different depths. As the seismicity seems to behave slightly different depending on where it is radiated from, we will further outline the details of this different behavior. The shallower seismicity highlights high angle normal faults (dip $\sim 50^\circ$) within the HW of the LANF and is radiated during time periods of increased activity. The deeper seismicity highlights the LANF, and exhibits a more constant behavior of seismic radiation.

Hanging Wall

During seismic surveys in 1987 (Deschamps, Scarpa, and Selvaggi, 1989) and 2000-2001 (Piccinini et al., 2003), a temporary increase of micro-seismicity ($M_L < 3$) was detected within the study area. Precise locations of the 2000-2001 micro-seismicity could reveal that it originates mainly from high-angle normal faults within the HW of the ATF (Piccinini et al., 2003).

The absence of a large magnitude ($M > 5$) events in recent decades makes the enhanced micro-seismicity in the HW a peculiar case in terms of its underlying driving mechanism. Even though, the largest events of these swarm sequences could potentially trigger small aftershock sequences, other mechanisms than stress transfer triggering by a mainshock (Freed, 2005), should be considered in order to keep the seismicity rate up to the observed level. In the study area two obvious mechanisms exist that could play a key role.

In the ongoing debate on how the extension is accommodated within the study area (Anderlini, Serpelloni, and Belardinelli, 2016; Vuan et al., 2020), Gualandi et al. (2017) found evidence for a slow deformation process overlapping in time and space with a swarm sequence in 2013-2014. This slow deformation could be seen as a possible driving mechanism. Here, the migration in space of the slow deformation front would change the stress at the tip of the front and could thereby potentially trigger seismicity along seismogenic asperities (Frank et al., 2016).

Studies indicated the abundant presence of fluids in the region (Chiodini and Cioni, 1989; Chiodini et al., 2004). Pore-fluid overpressure at 85% of the lithostatic pressure was found at depth within the San Donato borehole (Chiaraluce et al., 2014). Additionally, passive seismic studies found low velocity layers and related them to abundant fluids at depth (Piana Agostinetti, Giacomuzzi, and Chiarabba, 2017).

Fluids can trigger seismicity in different ways. Either they are able to directly induce seismicity by tensile crack opening, if the pore-fluid pressure reaches large values (Shapiro, Huenges, and Borm, 1997). Or, fluids facilitate the slow rupture which is then able to load seismically active asperities that themselves radiate seismic waves (Guglielmi et al., 2015).

LANF

Seismicity along the LANF is observed within a ~ 1000 m thick volume between ~ 6 to ~ 12 km depth (Chiaraluce et al., 2014; Valoroso et al., 2017). Ongoing debate on the seismicity rate posits that it is either quasi-constant (Valoroso et al., 2017) or modulated by processes within the HW (Vuan et al., 2020).

Constant or not, the recorded seismicity along the LANF radiates only small magnitude seismicity rarely reaching $M_L > 2.5$ (Chiaraluce et al., 2014; Valoroso et al., 2017). This is as well reflected in its frequency-magnitude distribution which is found to have a b-value > 1 (Valoroso et al., 2017).

Several mechanisms are proposed to drive this seismicity (Chiaraluce et al., 2014). The mechanism could be related to an extremely weak fault zone, that allows slip directly along the low-angle surface. It could also be related to strain localisation slightly above the LANF, or a complex architecture where different potential mechanisms (i.e., tectonic stress, stress redistribution due to the surrounded creep or pore-fluid overpressure) lead to slip along rate-weakening fault patches.

Seismic slip directly along the LANF surface is unlikely due to the found $\mu_s < 0.2$ that causes aseismic behavior (Collettini and Barchi, 2002). Seismic slip can be obtained through the introduction of fault patches with $\mu_s > 0.6$ and a large dip angle ($> 30^\circ$). Along small dip angles ($< 30^\circ$), one possibility to generate seismic slip is by increased pore-fluid pressure (P_f) up to > 0.95 of the lithostatic pressure (Figure 1.4; Collettini and Barchi, 2002). As seen in figure 1.4, an increase of the pore fluid pressure shifted the smallest and largest principal normal stresses towards negative and smaller values, respectively. This configuration would allow for the re-shearing of an existing fracture. One could argue that this type of behavior is difficult to reconcile with the established rate-and-state friction law, which predicts a stabilisation of slip with an increased fluid pressure (Dieterich, 1979). However, recent laboratory studies have shown that increased fluid over-pressure could promote a transition from velocity-strengthening to velocity-weakening behavior (Scuderi, Collettini, and Marone, 2017).

In another LANF model, the seismicity is related to constant loading due to creep within a matrix of minerals with extremely small $\mu_s < 0.2$ (Collettini et al., 2011). The small μ_s leads to aseismic behavior of the matrix, that is creep without the radiation of seismic waves. Within the creeping matrix, lenses of competent rock with a proper $\mu_s > 0.6$ are loaded due to the surrounding creep. Loading leads to the fact that these lenses of competent rock are brought to failure along high angle fractures within, which subsequently leads to the radiation of seismicity (Collettini et al., 2011).

Models provided by Lambotte et al. (2014), on the other hand, involve a non-elastic body at depth that concentrates the elastic strain upwards and produces only minor quantities of slip over the surface of the LANFs. Assuming those models are valid, very small slip would occur along the surface of the LANFs, which might not be able to load the competent rock lenses until failure and thereby radiate seismicity. Therefore, other mechanisms that could be related to the release of overpressurized fluids trapped within the foot-wall of the LANF, are proposed for radiating seismicity (Collettini and Barchi, 2002; Baisch and Harjes, 2003).

1.3.3 The Alto Tiberina Near Fault Observatory

In order to better investigate the seismicity along the ATF, The Alto-Tiberina Near Fault Observatory (TABOO) was installed in recent decades and provides a dense network of multi-parameter measurements within the study region (Chiaraluce et al., 2007).

Successively installed starting from 2010, the observatory consists of GNSS sensors and additional seismic sensors installed at the surface and within three boreholes at different depths (182 m at station BAT1, 204 m at station BAT2, and 150 & 250 m at station BAT3). While the surface sensors provide data sampled at 100 Hz, borehole sensors provide data at 500 Hz (Chiaraluce et al., 2014). The collected data is publicly available, distributed by the Italian National Institute of Geophysics and Volcanology (INGV).

Due to additional boreholes at Mt. Civitello (4.9 km depth, Latorre et al., 2016) and San Donato (4.2 km depth Latorre et al., 2016), a detailed geological model

could be extracted. This model was already used to derive precise velocity models of this region (Chiaraluze et al., 2007; Latorre et al., 2016; Mirabella et al., 2011).

The San Donato borehole additionally provided direct evidence for fluids and pore-fluid overpressure at about 100 MPa (85% of the lithostatic pressure) at a depth of 4.7 km (Chiodini and Cioni, 1989).

1.4 Open questions

Even though the ATF system might be one of the best studied LANF worldwide, several questions remain open. For example, there is still an ongoing debate on how the overall system accommodates and releases the strain, introduced by the extension of the region.

It has been suggested, that this could be done via deformation along the LANF (Anderlini, Serpelloni, and Belardinelli, 2016), along high angle normal faults within the HW (Gualandi et al., 2017), or a coupled system with interaction between the HW and the LANF (Vuan et al., 2020). Models that were developed in similar regions of extension, predict strain localisation to shallower parts by a non-elastic body at depth (Lambotte et al., 2014). In the latter model, only small amounts of strain will be released along the LANF.

The validity of each model has different impact on the seismic risk of the study area. If, for example deformation is accommodated along the LANF, this could load locked asperities ($\mu_s > 0.6$) over time into a state in which they could produce a larger earthquake (Anderlini, Serpelloni, and Belardinelli, 2016; Valoroso et al., 2017). Similarly, seismic asperities could be loaded until failure within the HW if the strain is released there. In this model, similar to the model proposed by Lambotte et al. (2014), a potential mechanism driving the LANF seismicity is needed.

To answer the question about validity of the proposed models, we will use the micro-seismicity radiated from different locations of the study area (LANF and the HW). This seismicity will be used as a window, allowing us to shed light into the mechanisms active at depth.

Within the HW of the ATF system, we will further shed light into the mechanism responsible for the seismicity radiated during swarms. Swarms are of general interest due to several reasons.

First, some larger earthquakes have been preceded by a swarm like increase of seismicity in close vicinity to the imminent mainshock (Cabrera, Poli, and Frank, 2022; Kato et al., 2012). Therefore, swarms have been interpreted as the manifestation of a process of slow rupture initiation (Kato et al., 2012). Second, assuming a swarm as the manifestation of a slow-slip event in general could help to better understand large, fast earthquakes as they could share some characteristics (Peng and Gomberg, 2010). The third point of interest related to swarms is the apparent connection to fluids (De Barros et al., 2020; Fischer et al., 2014), which are abundant within the region (Chiodini et al., 2000). As in recent decades, fluid injection projects have lead to an increase of seismicity (Schoenball and Ellsworth, 2017), a better understanding of the physical mechanism is necessary to reduce the seismic hazard associated with large-scale injection projects. Therefore, the relationship between fluid injection and seismicity needs to be better understood (Danré, De Barros, and Cappa, 2022).

To answer the former mentioned open questions, a detailed picture of the earthquakes within the region is derived. For this aim, a high-resolution catalog is created first. Therefore a matched filter approach will be applied (Chapter 2), that exploits waveforms of known earthquakes in order to detect previously undetected earthquakes with similar waveforms. Applying this technique, a high resolution (in terms of space and time) earthquake catalog is obtained that will be analysed to get insights into large space and time scale processes (Chapter 3).

To obtain more detailed insights about processes acting within the HW, a clustering approach will be applied that exploits recent unsupervised machine learning algorithms (Chapter 2). This will help to extract a more detailed picture of the space and time evolution of the seismicity, which could provide indication about possible driving mechanisms of the swarm activity (Chapter 4).

Then, in chapter 5 the focus will be on the seismicity along the LANF in order to answer questions regarding its driving mechanism. Therefore peculiar repeating earthquakes (Uchida, 2019) are further analysed. These events, radiated from several locations exhibit relatively short times between consecutive earthquakes, a fact that is difficult to reconcile with loading due to creep along the LANF.

Finally, in chapter 6 I will conclude the findings resulting from the different chapters (3, 4, 5) with overall perspectives for future work.

Chapter 2

Methods

2.1 Detecting Earthquakes

2.1.1 Traditional Methods

For decades the most widely used method to detect earthquakes was a power detector (Freiberger, 1963). This approach relates the average power within a short time window (STA) to the average power within a longer time window (LTA). A new event is detected if the ratio ever surpasses a specified threshold. These type of approaches work efficiently for larger earthquakes, which produce a high STA/LTA ratio. On the other hand, small magnitude earthquakes which produce signals only slightly above the noise level are difficult to detect with this method (Gibbons and Ringdal, 2006). An additional issue is that instead of earthquakes, transient noise sources might be detected, leading to false-detections.

Within recent decades statistical approaches were developed (Küperkoch et al., 2010), and with the advent of machine-learning in seismology, methods using trained convolutional neural networks (CNN) are becoming more popular for earthquake detection and phase picking (Zhu and Beroza, 2019; Majstorović, Giffard-Roisin, and Poli, 2021). These approaches show promising results when compared with picks done by national earthquake agencies (Münchmeyer et al., 2022). However, so far, these approaches only work as single station approaches which again limits the detection possibility to a certain magnitude limit.

To overcome the limiting noise level and be able to detect events even below, cross-correlation or matched-filter techniques have shown a promising performance (Gibbons and Ringdal, 2006). These type of techniques exploit waveforms of earthquakes that were detected by conventional methods (i.e., templates) and cross-correlate them against continuous seismic data in order to find similar events. The so called matched-filter approaches are highly sensitive to the waveform of the template event. As globally observed earthquakes show large variation in waveforms, these type of techniques were not widely used in seismology at first (Gibbons and Ringdal, 2006).

However, in recent decades, with the advancements in computational power and the finding of earthquakes with similar waveforms (e.g., repeating earthquakes, aftershock sequences, swarm seismicity), the use of matched-filter techniques became and more favorable.

To further lower the detection threshold of matched-filter techniques, array-processing techniques can be used in such a way that the summation of coherent signal and cancellation of incoherent noise is ensured (Gibbons and Ringdal, 2006).

First attempts of array-based matched-filter approaches were done by Anstey (1964) where it was shown that the identification of a synthetic signal buried in noise via waveform correlation is possible. However, it took some more decades to finally apply these approaches to earthquake data.

First tests of an array matched-filter approach were done using the NORES, NOR-SAR and Hagfors seismic arrays in Scandinavia (Gibbons and Ringdal, 2004; Stevens et al., 2004). In that study, small, underground explosions in Central Sweden at around 150 km away from each array were monitored. One of these explosions was used as a template to subsequently scan the time series at all seismic sensors. While the conventional methods (STA-LTA) were able to detect only the largest event, the matched-filter approach was able to extract all of them. Additionally, the matched-filter approach did not detect anything else within a time period of 2 years, highlighting the remarkable low false detection rate of this technique (Gibbons and Ringdal, 2004). After this first study, further tests with proper seismic events were conducted in order to test the capability of the proposed approach for natural events (Gibbons and Ringdal, 2006).

A growing number of matched-filter experiments have been performed in recent years. In particular, this technique has been applied in regions where the seismicity occurs in a confined volume and seems to be driven by a shared or similar physical mechanisms. For instance to study earthquake swarms (Cochran et al., 2018; Poli et al., 2022; Shelly and Thelen, 2019).

2.1.2 Matched-Filter Approach

The matched-filter (also called template matching) approach relies on a priori knowledge about the seismicity within a certain area, as well as the velocity structure (i.e. travel times) of that given zone. Combining this knowledge, one can predict the phase arrivals of a given set of well-known earthquakes at stations suitable for the matched-filter approach. The phases of interest, which in this work are the P- and the S-phase, will be extracted at every station that should be used. As seen in figure 2.1a, the travel time differences from the source to each stations (i.e., move-out) is considered as it implicitly contains the information of the velocity structure of the subsurface structure. The collection of waveforms recorded at different stations, together with their move-outs, now serves as a template. Once the template is constructed, it can be used to scan the continuous waveforms. This scanning is performed by moving (cross-correlating) the template waveform along the continuous time series. At each sample, the correlation coefficient (CC) between the template window and the continuous data is calculated. This is done at each station and the resulting CC values are averaged which yields the mean CC function (see Figure 2.1b), from which new detections can be extracted.

To extract new detections from the mean CC function, a statistical measure of its mean is introduced (Figure 2.1b), which in this work is the median absolute deviation (MAD). By introducing a threshold, based on the MAD, we can turn the matched filter approach into an earthquake detector. At every time step that the estimated MAD exceeds this threshold, a new detection is found. In figure 2.1b, the threshold is set at 12 times the MAD, which will be the threshold used in chapter 3. This threshold is a rather conservative value when compared to previous works (Brown, Beroza, and Shelly, 2008; Shelly, 2020).

The waveforms of the template together with its new detections, sorted by a decreasing mean CC, can be seen in figure 2.1c. The waveforms seem remarkably similar, as one would expect. This is valid even for portions that were not included in the template, such as the highlighted part within the S-phase coda of the shown waveforms (2.1c). This waveform similarity illustrates the fact that these seismic events shared (at some point) the source mechanism and the velocity structure where the waves traveled through.

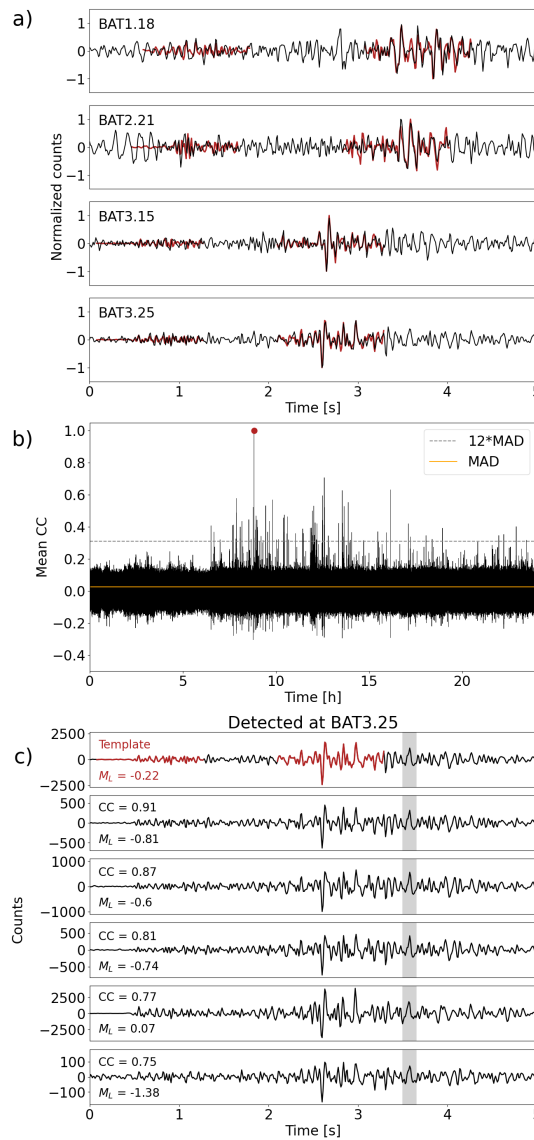


FIGURE 2.1: (a) Normalised continuous waveforms (black) recorded at the vertical components of four seismic stations installed within three boreholes within the study area (Figure 1.2). Numbers within station names indicate the depth of the seismic sensor within the borehole. The template waveform (red) is indicated at a sample step where it identifies a new detection within the continuous waveforms. (b) The mean correlation coefficients (CC) over the station array. The auto-detection, which is the sample step from which the template was retrieved, is shown by the largest peak at $meanCC = 1$ (red dot). The median absolute deviation (MAD) is indicated by an orange horizontal line. The threshold for event detection ($12 * MAD$) is indicated with a dashed grey, horizontal line. (c) The top row shows the waveforms of the template (red) together with the full waveform of that seismic event. Rows below show new detections sorted by a decreasing mean CC. All waveforms are extracted from the vertical component of *BAT03.25*. The mean CC is indicated together with the estimated local magnitude (M_L). Waveform similarities outside the template window are highlighted in grey.

Once the new detections are extracted, a first-order approximation of the local magnitude (M_L) can be estimated. This can be done by estimating the ratio between the average root mean square (RMS) of the time windows containing the P- and S-phases of the new detections and the respective RMS related to the detecting reference template.

By assuming that detected events are collocated to their template, the origin times of each new detected event can be estimated by back-projecting the travel-times of the template. This fundamental assumption, however, is not entirely correct, as we shall discover in chapter 3 and 4, which show that templates are sensitive to a certain volume surrounding their location, depending on the frequency band and the signal duration.

The use of cross-correlation methods over a station network (e.g. a matched filter approach), has shown to be optimal to detect earthquakes even below the noise level (Sánchez-Reyes et al., 2020; Shelly et al., 2006). Therefore, it is especially powerful when it comes to the detection of micro-seismicity, which is usually believed to be driven by the same mechanisms and therefore producing similar waveforms (Cochran et al., 2018; Poli et al., 2022; Shelly and Thelen, 2019).

A well-known drawback of strategies such as the matched-filter approach is the fact that they rely on a given set of known earthquakes. Such list of earthquakes are usually taken from the available local, regional or global seismic catalogues. Such earthquake catalogues are the basis for constructing the templates, as they provide origin times and locations of the events. As a result, if no seismicity is listed for a specific region, even if it exists, the matched-filter techniques are blind to it. It is therefore advised to cover the whole study area with templates, thus use as many templates as available.

However, then the approach is computationally expensive, especially when compared to recent automatic picking methods. This is due to the fact that in matched-filter approaches, the continuous time series is scanned with every template, while automated pickers scan only once at each station.

2.2 Clustering

2.2.1 Earthquake clustering

As seen in chapter 1, the ensemble of earthquakes within a certain region consists of background and clustered seismicity (Gardner and Knopoff, 1974), where the clustered seismicity can be further subdivided into seismicity that is triggered by post-seismic processes after a mainshock (Freed, 2005; Miller et al., 2004; Perfettini and Avouac, 2004) or by a process like aseismic deformation (Guglielmi et al., 2015) or fluid migration (Shapiro, Huenges, and Borm, 1997). Several methods exist that are able to quantify the degree of clustering within earthquakes (Kagan and Jackson, 1991) and further separate background from clustered seismicity (Baiesi and Paczuski, 2004; Davis and Frohlich, 1991; Frohlich and Davis, 1990; Zaliapin et al., 2008; Zaliapin and Ben-Zion, 2013a; Zaliapin and Ben-Zion, 2013b).

Kagan and Jackson (1991) introduced an approach to quantify the temporal clustering of seismicity. They measure the coefficient of variation C_v (the ratio of the standard deviation σ and the average) of the distribution of the times in between consecutive events, to determine the degree of temporal clustering of a given seismic sequence. Their estimates can be summarised by defining reference values for the C_v . For instance a $C_v = 0$ indicates periodic, a $C_v = 1$ Poissonian (i.e., random), and a $C_v > 1$ indicates clustered seismicity. While their approach works well in quantifying the degree of clustering (Cabrera, Poli, and Frank, 2022; Cochran et al., 2018; Sánchez-Reyes et al., 2020), it is not possible to use it to further separate (i.e., de-cluster) the seismicity into clustered and unclustered seismicity.

From now on, we will denote this separation of events by the term "de-clustering", and further briefly introduce the development of methods, that are nowadays used to do so.

One of the first approaches of de-clustering was done using fixed space-time windows with a pre-assigned main event (Gardner and Knopoff, 1974). However, this approach requires to define a certain space-time window size, and is further not able to handle aftershocks of aftershocks (Helmstetter and Sornette, 2002).

To perform de-clustering in a more quantitative way, first methods were introduced by Davis and Frohlich (1991) and Frohlich and Davis (1990) following a Single-Link Cluster analysis (SLC). Their approach connects earthquakes by a chain of minimum length (i.e., the nearest neighbors) depending on the distance metric (d_{st}) which they defined as

$$d_{st} = \sqrt{d^2 + C^2 t^2}, \quad (2.1)$$

where d is the minimum epicentral distances and t the minimum time between two consecutive events. C is a parameter that, depending on the study area, may be used to up- or downscale the temporal distances between events. It was set to 1 in their study (Davis and Frohlich, 1991; Frohlich and Davis, 1990). To find clusters, one can now set a certain d_{st} threshold, and disconnect earthquakes with distances above it. This ensures that given groups of seismicity disconnect from other groups, thereby opening distinct clusters of seismicity.

To estimate distances between nearest neighbours, Baiesi and Paczuski (2004) introduced a slightly different distance metric. More precisely they proposed

$$\eta_{ij} = C t d^{d_f} \Delta m 10^{-mb_i}, \quad (2.2)$$

thus including the distance d and time t between events. In their approach they

additionally considered the fractal appearance of earthquake epicenters d_f , consequently the expected number of events of magnitude within Δm of m_i , occurring in the specific space-time domain limited by events j and i . They further considered the Gutenberg-Richter (G-R) distribution for the number of earthquakes of magnitude m in a certain area $P(m) \sim 10^{-bm}$. Finally, C is a constant depending on the overall seismicity.

Zaliapin et al. (2008) extended the approach of Baiesi and Paczuski, 2004. By analysing the joint distributions of the nearest-neighbor distance η_{ij} , they found a bi-modal distribution (Figure 2.2a). In their approach, they defined nearest neighbor following

$$\eta_{ij} = \begin{cases} t_{ij}(r_{ij})^{d_f} 10^{-b(m_i-m_0)} & , t_{ij} > 0; \\ \infty & , t_{ij} \leq 0. \end{cases} \quad (2.3)$$

Again we find the time t between events and the spatial distances r considering the fractal appearance d_f as well as the normalisation with the G-R distribution.

To further study the observed bi-modal distribution of η_{ij} , Zaliapin and Ben-Zion (2013a) and Zaliapin and Ben-Zion (2013b) analysed the distributions of time T and the space distances R between nearest events (η_{ij}), both normalized by the magnitude

$$\begin{aligned} T_{ij} &= t_{ij} 10^{-bm_i/2}, \\ R_{ij} &= r_{ij}^d 10^{-bm_i/2}. \end{aligned} \quad (2.4)$$

As seen in figure 2.2b, the joint distribution exhibits two denser areas, separated by a diagonal line. The lower left part of the joint distribution (i.e., small values for T and R) represent nearest neighbor distances of clustered seismicity while the upper right part (i.e., large values for T and R) indicate stationary seismicity (Zaliapin et al., 2008).

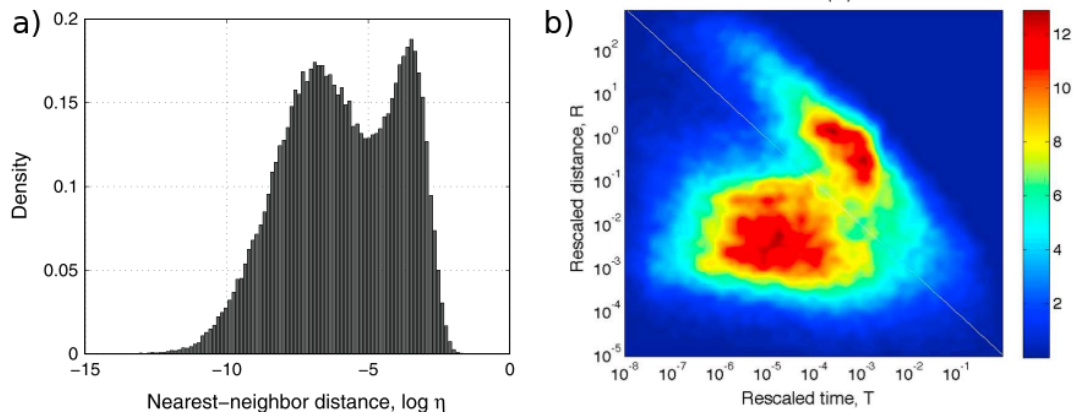


FIGURE 2.2: (a) Histogram of the normalized nearest-neighbor distances η . (b) The joint distribution of the rescaled time T and space R components. Modified from Zaliapin and Ben-Zion (2013a).

2.2.2 Clustering in a General Way

Chapter 4's objective is to extract clusters of seismicity from a large seismic dataset. Therefore, it is necessary to establish a rather automatic strategy to define such

clusters. To do that, unsupervised learning techniques will be applied. These techniques have been recently developed in the field of machine learning and the application in seismology start to be of great interest (Majstorović, Giffard-Roisin, and Poli, 2021; Sánchez-Reyes et al., 2020).

Clustering or cluster analysis is a general term for a vast number of statistical approaches. The basic idea of these strategies is to find a way to subdivide a global set of observations into sub-groups. Such subdivision has to be based in the similarity of multiple characteristics of such observations (Wilmink and Uytterschaut, 1984). These subgroups are commonly referred to as clusters. There is no universal definition of the term of cluster, however, observations within resulting clusters should show internal cohesion and external isolation (Cormack, 1971). One significant benefit of cluster analysis is that most statistical approaches do not require a priori knowledge of the number of clusters or the structure. As a result, cluster analysis is tempting as an exploratory tool; nevertheless, consideration should be given to the best statistical approach to apply to a certain data-set.

First attempts of clustering were published by Tryon (1939). With the advent of increased computational power in the 1960s, clustering was first applied to scientific fields like botany and ecology (Williams and Lambert, 1959). With the most recent increase of computational power even private computers are now able to conduct large scale data analysis. This, and the availability of open access machine-learning libraries (e.g., sci-kit learn Pedregosa et al., 2011), are a reason why clustering has become an important exploratory tool in data science in general.

As indicated, clustering is a general term for a vast number of different statistical approaches that can be divided into hierarchical, k-group, and density methods among many others. In the following part, two basic clustering approaches are introduced which will be used in a combined way to analyze seismic catalogs. The combination of the two is applied in chapter 4 in order to extract meaningfully clusters of seismicity from a high-resolution earthquake catalog.

Hierarchical Methods

Hierarchical methods build a hierarchy of observations and clusters based on a distance measured between them (Ward Jr, 1963; Wilmink and Uytterschaut, 1984). Once a certain similarity measure is defined, the observations or clusters with the shortest distance in between (i.e., the highest similarity) are brought together. This step basically connects the nearest neighbours. The resulting distances can be represented by a hierarchy, which is called a dendrogram (Figure 2.3d).

In figure 2.3 one can see an example of hierarchical clustering from a seismological study (Sánchez-Reyes et al., 2020). In this example Sánchez-Reyes et al. (2020), exploited the similarity of the waveforms (measured in terms of the correlation coefficient between waveforms) of several hundreds of earthquakes as a distance measure which was then used as an input to perform hierarchical clustering. The resulting hierarchy (Fig 2.3d), represented as a simplified dendrogram, reflects the main distances between the observations or clusters. As it is simplified, here the branches (starting at a distance of 0) represent subgroups of events (number of events inside the subgroup are indicated within the parenthesis). From that tree, it is possible to estimate the separation distance between a certain subgroup of the green cluster and a subgroup of the pink cluster. The separation distance is the distance needed to climb up and down the hierarchy that connects the green and the pink cluster.

Without any final decision on the distance threshold for clustering, this hierarchical representation shows that the green cluster is fairly separated from the other

clusters (red, blue, brown, purple), which are themselves relatively close in distance. The horizontal line shows the distances threshold to divide the tree into five clusters at a distance of 5.5 (Sánchez-Reyes et al., 2020).

An examination of the temporal evolution of the distinct clusters reveals different types of seismic behavior (2.3b). For example, events belonging to the green clusters mainly occur before the largest event of the sequence, which is indicated by the red vertical line in figure 2.3b. This is noteworthy, since no temporal information was given into the hierarchical clustering approach.

Figure 2.3c shows the stacked waveforms recorded at a given station, of the five resulting clusters. It is clear that different clusters exhibit different P-S differential times as well as different P-wave arrivals, indicating a different spatial origin of the earthquakes of different clusters.

Density based Methods

Density based clustering methods scan the feature space for areas of lower and higher densities of observations (Ester et al., 1996). The density is measured by taking into account the number of observations in close vicinity (Figure 2.4a). For these type of strategies, it is important to define a hyper-parameter related to the distance (i.e., radius) within which the algorithm will be looking for other observations. The second hyper-parameter is related to the number of neighbouring observations inside that radius (i.e., the density).

By doing so, two types of observations arise. Core observations that have the required amount of observations within the defined distance and outlier events which do not meet the required number. Clusters are identified by combining all observations in an isolated area of high density (i.e., that meet the previously established requirements). Areas of high density will end up being surrounded by other regions with lower densities. The familiarity of this clustering technique with the concept of detecting outliers makes it particularly interesting for earthquake catalog applications, where we anticipate that both clustered and background seismic activity should be present (Cesca, 2020; Piegari, Hermann, and Marzocchi, 2022).

Piegari, Hermann, and Marzocchi (2022) used this approach and applied it to synthetic and real earthquake catalogs, considering the 3D space information of every earthquake as observations for clustering (Figure 2.4b). The synthetic data-set seen in figure 2.4b consists of five groups following predefined structures and a last group following a (unstructured or noisy) uniformly distributed function. As one can see by the color-coded events, the clustering approach is able to extract denser areas, while events in sparse areas (grey dots) are considered as outliers.

Clustering using HDBscan

In chapter 4 a clustering algorithm called Hierarchical Clustering and Density-Based Spatial Clustering of Applications with Noise (HDBscan, Campello, Moulavi, and Sander, 2013) is applied to an earthquake catalog. HDBscan combines the two introduced types of clustering approaches that are hierarchical clustering (Ward Jr, 1963) and density-based clustering (Ester et al., 1996).

The first step in the clustering pipeline of HDBscan consists of the transformation of the feature space from the original space (Figure 2.5a) to the mutual reachability distance space (Eldridge, Belkin, and Wang, 2015). This feature space transformation is used first to measure the density in the feature space to then push

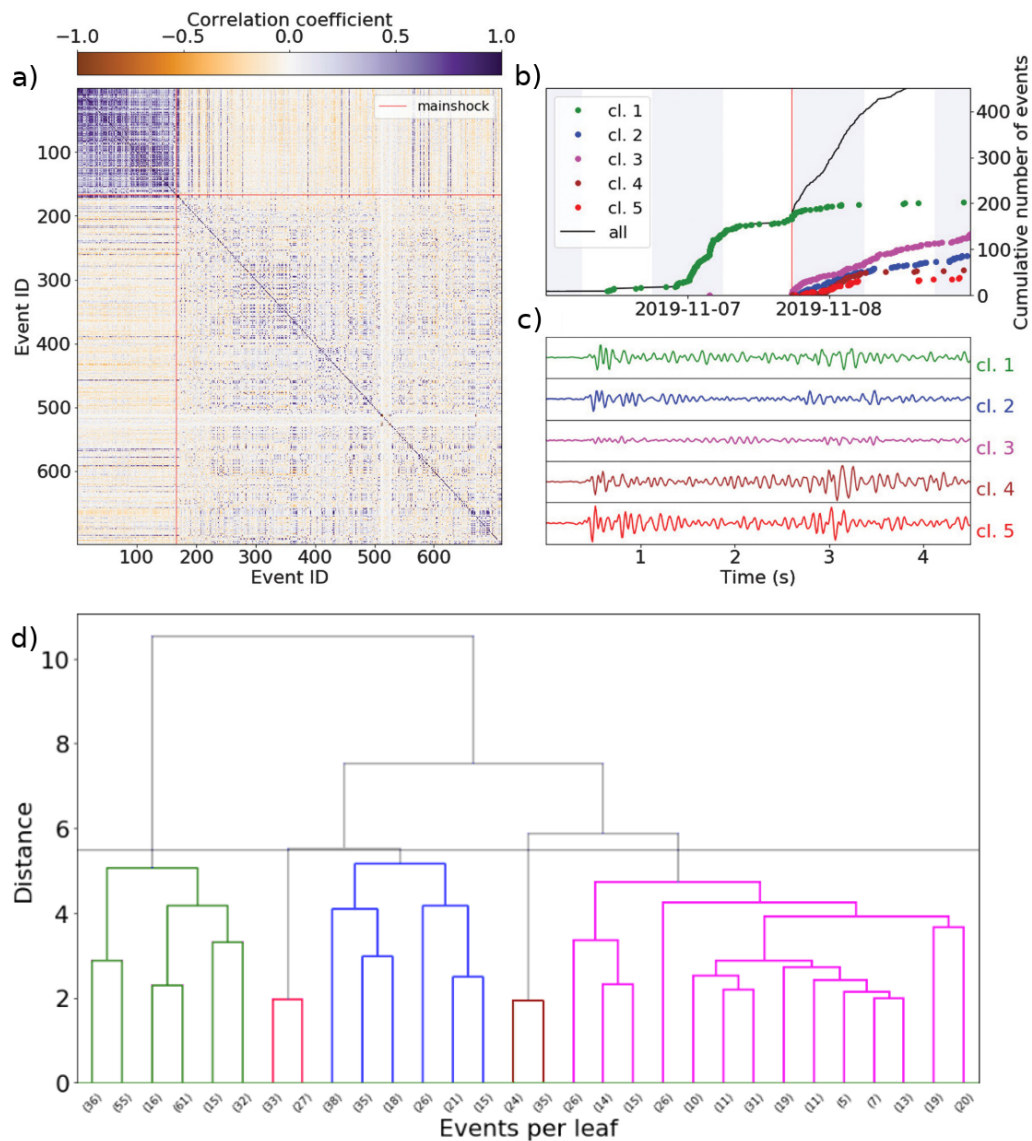


FIGURE 2.3: (a) Pairwise correlation coefficients between the waveforms of 714 seismic events. The matrix is used as an input to perform hierarchical clustering. (b) Cumulative event number for the five resulting clusters, indicated by the color code. (c) Characteristic normalized waveforms of the five clusters revealed in the earthquake sequence. Traces are obtained after stacking all individually normalized waveforms of each cluster. (d) Dendrogram obtained from the waveform-based hierarchical clustering. A distance threshold of 5.5 is indicated by the grey horizontal line, resulting in 5 clusters. The color code used for every branch represents the five different cluster identified as in (b) and (c). Modified from Sánchez-Reyes et al., 2020.

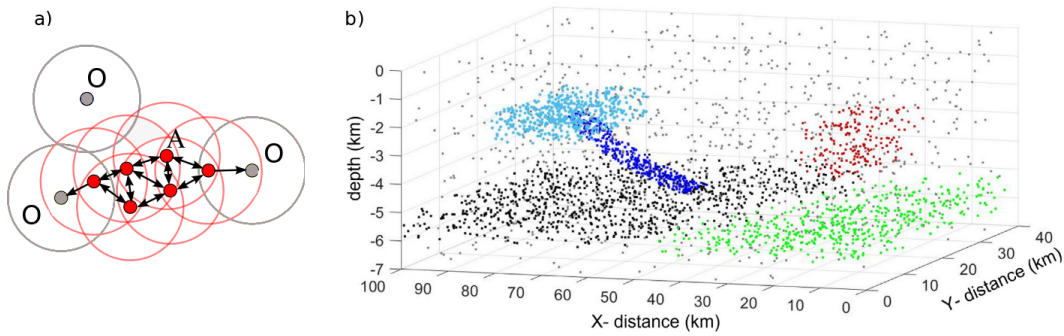


FIGURE 2.4: (a) Example of the measurement of density in the feature space. The number of events within a certain radius (hyper-parameter 1) are counted. If the number exceeds a certain threshold (hyper-parameter 2), events are defined as core events (red dots). If the number of events within the distance threshold is not exceeded, events are defined as outlier events (grey dots). (b) Spatial distribution of a synthetic data set. The color-coded structures indicate their affiliation to areas of higher event density (i.e., clusters), while grey dots indicate their affiliation to sparse areas. Modified from Piegari, Hermann, and Marzocchi (2022)

features in sparse areas farther apart, while leaving features in dense areas untouched. Within the mutual reachability distance space, the algorithm then connects the nearest neighbors using Prim's algorithm (Prim, 1957). This results in a minimum spanning tree (MST), where the connections between points (edges) are weighted according to their mutual reachability distances (Figure 2.5a). In figure 2.5a in the upper right part one can see that some points are connected, even though their distance in the original space seems larger compared to other points in closer vicinity. This is happening in sparse areas and it is the manifestation of the former mentioned space transformation into the mutual reachability distance.

The estimated MST is converted into a hierarchy, where events and group of events are connected according to their mutual reachability distance (Campello, Moulavi, and Sander, 2013). As shown in figure 2.5b, the hierarchy can be represented as a dendrogram. With the use of a global threshold for the mutual reachability distance, thus the densities of the feature space, one could start with the extraction of clusters (Cesca, 2020; Piegari, Hermann, and Marzocchi, 2022).

However, this might not be satisfactory as clustering of seismicity can happen on different space and time scales, which can be interpreted as different event densities. Therefore, HDBscan expands the clustering pipeline.

Figure 2.5b shows that if the mutual reachability distance is reduced from 90 to 50, single events (black lines), split apart from the hierarchical tree. These are events that HDBscan classifies as outliers. By further lowering the mutual reachability distances from 40 to 30, entire networks (marked by 1, 2, and 3) of events split apart (Figure 2.5b). The implementation of a hyper-parameter called minimum cluster size now allows to use these networks as potential new clusters if the number of events within exceeds the introduced hyper-parameter (Campello, Moulavi, and Sander, 2013). This step condenses the built hierarchical tree (Figure 2.5c). Now distances between clusters are indicated by the inverse of the mutual reachability distance (λ), and potential clusters are represented by colored areas. The horizontal width of each cluster in figure 2.5c indicates the number of events within, which decreases with the increase of λ , due to the drop out of single events.

In figure 2.5c one can see that several potential sets of cluster exist, depending on the decision whether to consider clusters with smaller λ values (parent cluster) or the descendant clusters with larger λ values (offspring cluster). HDBscan decides this in an automated way by estimating the stability of each cluster by comparing the sum $\Sigma(\lambda_p - \lambda_{birth})$ of the parent and the offspring clusters (Campello, Moulavi, and Sander, 2013). Here λ_p is the value at which a certain point splits off while λ_{birth} the value at which a cluster is opened. If the sum of the offspring clusters now has a larger value than the parent cluster, the offspring clusters are maintained as clusters. Vice versa, the offspring clusters would be merged into the parent cluster. Figure 2.5c, for example illustrates cluster 1 and 2, where the decision was made favoring the offspring clusters.

The whole pipeline of HDBscan follows a single-linkage approach, as used for other clustering methods in seismology (Davis and Frohlich, 1991; Frohlich and Davis, 1990; Zaliapin et al., 2008; Zaliapin and Ben-Zion, 2013a; Zaliapin and Ben-Zion, 2013b). An advantage of HDBscan is that the algorithm does not require a global density threshold due to the individual selection of clusters to be considered. Indeed, in the example presented, a pure density-based approach would not have found this set of clusters where the event densities of cluster 1 and 2 are comparable but relatively dense with respect to cluster 3 (Figure 2.5a, d). Thus, HDBscan helps to extract clusters with different levels of densities.

HDBscan can be controlled by either just the introduced minimum cluster size hyper-parameter or an additional hyper-parameter called minimum samples. The latter hyper-parameter defines how conservative the clustering will be in determining outliers. In chapter 4, there is a brief discussion of the stability of the clustering outcome related to a change of the hyper-parameter.

An advantage of the algorithm is that observations do not necessarily need to end up in clusters but can be defined as outliers, analogue to background seismicity (Chapter 1). The additional capability of finding clusters of different event densities is another advantage when applied to earthquake catalogs, where seismicity in different regions might cluster more or less strong in feature domains (e.g., space, time, among others).

Another advantage of the algorithm is that it is realised in a very efficient way that allows to perform clustering of large data-sets as will be seen in chapter 4.

The advantages come with the cost of not having total control of the extracted clusters, as in the last clustering step, HDBscan decides which cluster to extract based on the stability measure which itself is not straightforward.

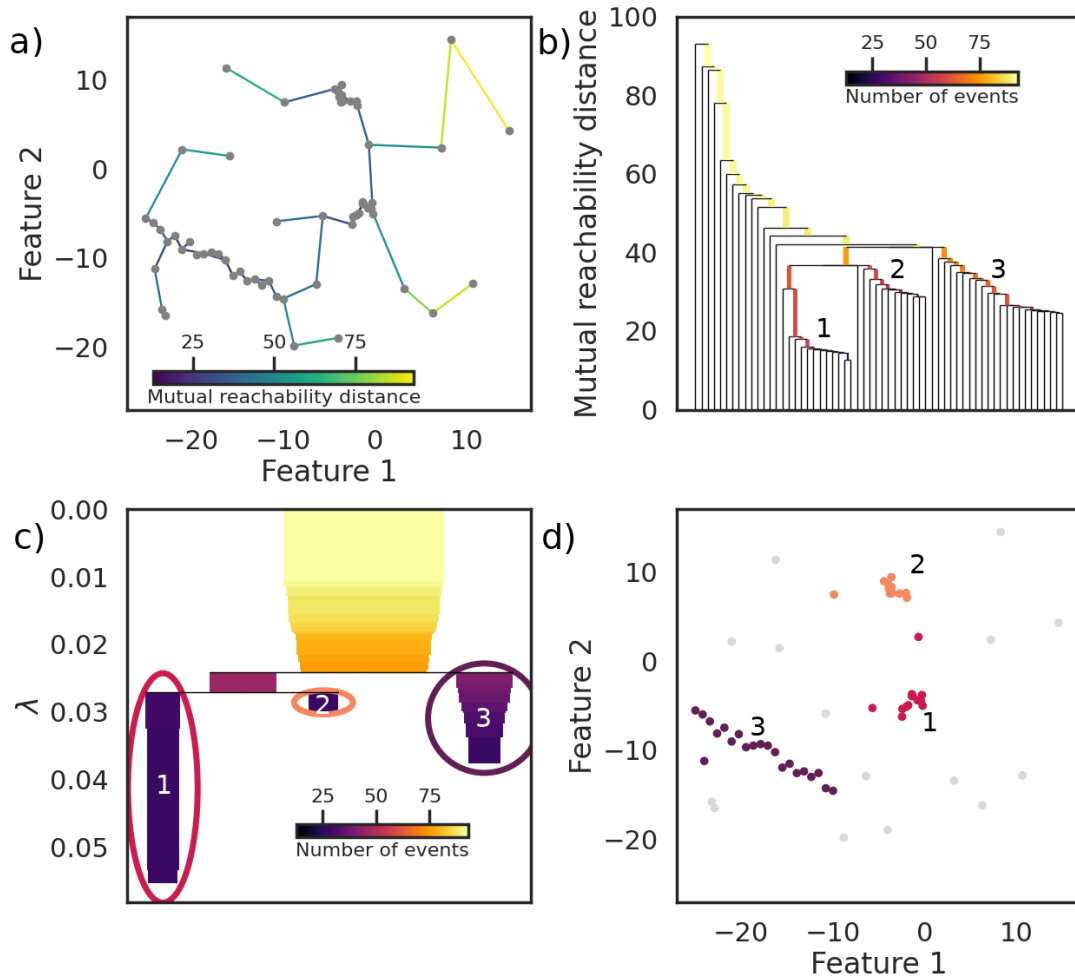


FIGURE 2.5: Conceptual pipeline of HDBscan. (a) 2D feature space of a set of synthetic example events (grey dots). The network of colored lines (i.e., edges) represents the minimum spanning tree (MST), where a single line connects the two closest events according to the mutual reachability distance. (b) Hierarchical tree, representing the mutual reachability distances from the MST. The networks that are finally classified as clusters are shown as numbers. (c) Condensed hierarchical tree where the color-coded ellipses and numbers indicate the event networks which are finally considered as clusters. (d) The 2D feature space as indicated in (a), colored events indicate their affiliation to a certain cluster (indicated by numbers) as seen in (c). Outliers (i.e., background seismicity) are indicated by grey dots.

Chapter 3

Spatiotemporal Evolution of the Seismicity in the Alto Tiberina Fault System Revealed by a High-Resolution Template Matching Catalog¹

Abstract

The Alto Tiberina Fault system, located in the Northern Apennines (Italy), consists of a low angle normal fault (LANF) which radiates micro-seismicity that can be explained by continuous creep. On top of the LANF, a network of syn- and antithetic high angle faults frequently hosts seismic swarms, one of which has been associated with a transient aseismic deformation signal. To study in detail the seismicity and its relationships with aseismic deformation processes occurring in this fault system, we apply template matching on seismic data recorded at an array of borehole stations, to derive a high-resolution earthquake catalog. Thanks to the additionally detected events, we are able to reveal time periods of increased spatial- and temporal clustering during an aseismic deformation event. This reflects the complex evolution of aseismic slip together with the complexity of the shallow fault system. Along the LANF, we observe a bimodal type of seismicity, with diffuse seismicity active continuously, and short-lived bursts of seismicity that could indicate rapid fluid releases. We additionally identify repeating earthquakes. These events not necessarily match a simple creep model and therefore open the possibility for new models to explain the seismicity along the LANF.

¹Published as Essing, D., & Poli, P. (2022). Spatiotemporal Evolution of the Seismicity in the Alto Tiberina Fault System Revealed by a High-Resolution Template Matching Catalog. *Journal of Geophysical Research: Solid Earth*, 127(10), e2022JB024845.

3.1 Introduction

Low angle normal faults (LANF) are intriguing geological structures found in extensional tectonic regimes (Wernicke, 1995). Those structures are normal faults with a dip angle lower than 30° , which should inhibit frictional fault reactivation under the well accepted Anderson-Byerlee theory of faulting (Byerlee, 1978; Collettini, 2011). Nevertheless, seismically active LANFs are found in several locations around the world, such as in Greece in the Gulf of Corinth (Rietbrock et al., 1996), in Papua New Guinea in Mai'iu (Abers, Mutter, and Fang, 1997; Biemiller et al., 2020) and in Italy along the Apennines (Chiaraluce et al., 2007). Observations of seismic activity along LANFs raises the question whether these faults are capable of producing moderate-to-large magnitude earthquakes, or whether other deformation mechanisms accommodate the extension (e.g., Collettini, 2011; Wernicke, 1995).

A well-studied LANF is the Alto Tiberina Fault (ATF) located in the Apennines (Figure 3.1), which is thought to accommodate large portions of the overall tectonic extension of ~ 3 mm/yr within the region (Serpelloni et al., 2005). The structure of this fault is well characterized by several seismological studies, as deep seismic reflection profiles (Barchi et al., 2003), controlled source seismic imaging (Mirabella et al., 2004), and seismic tomography (e.g., Chiarabba and Amato, 2003; Pauselli et al., 2006; Piana Agostinetti, Giacomuzzi, and Chiarabba, 2017). Further studies characterized the ATF with gravity (Boncio, Brozzetti, and Lavecchia, 2000), magnetic (Collettini and Barchi, 2002), and heat flow measurements (Mirabella et al., 2004). These studies reveal a NNW trending major fault dipping $15^\circ - 20^\circ$ from the surface to $\sim 12 - 14$ km depth. Below 4 km the fault plane is highlighted by micro-seismicity within a 500 – 1000 m thick fault zone (Chiaraluce et al., 2007). This micro-seismicity was initially observed at a constant rate (Chiaraluce et al., 2007), while recent research highlighted a variable rate of seismicity along the shallow parts of the LANF, connected with the activity in the hanging wall (HW, Vuan et al., 2020).

The HW of the LANF is dominated by several syn- and antithetic splay faults with high dipping angles of $50^\circ - 60^\circ$. The largest structure is the Gubbio fault showing a listric geometry, dipping $40^\circ - 60^\circ$ at shallow depths and bending to $10^\circ - 15^\circ$ below depths of 3 – 4 km (Mirabella et al., 2004). Between 3 and 6 km depth, the HW is characterized by high V_p - V_s ratios, indicative of high pore-fluid pressure (Chiarabba and Amato, 2003; Piana Agostinetti, Giacomuzzi, and Chiarabba, 2017). This layer consists of Mesozoic carbonates and Triassic evaporitic rocks and hosted several swarm-type seismic sequences in 2001 (Chiaraluce et al., 2007; Piana Agostinetti, Giacomuzzi, and Chiarabba, 2017; Piccinini et al., 2003), 2010, and 2013–2014 (Valoroso et al., 2017). Rare is the occurrence of events larger than $M_w \sim 4$. Among these events, the better recorded occurred in 1984 a M_w 5.6, and probably ruptured a fault in the HW (Collettini et al., 2003; Haessler et al., 1988; Pucci et al., 2003). Historical events with $M > 6$ in 1352, 1751, and 1781 are also reported for the area but not directly linked to the ATF (Valoroso et al., 2017).

Focusing on the mechanical behavior of the ATF, several studies (Anderlini, Serpelloni, and Belardinelli, 2016; Chiaraluce et al., 2014; Collettini et al., 2011; Hreinsdóttir and Bennett, 2009; Vadacca et al., 2016) proposed that the extension in the area is accommodated to some degree by creep along the LANF. Combining a block modeling approach with GNSS velocities measured at a dense GNSS network in the area, Anderlini, Serpelloni, and Belardinelli (2016) inferred partial creep of 1.7 mm/yr along the LANF, with several asperities being locked. Later, the geodetic data analysis of Gualandi et al. (2017) revealed a small transient deformation equivalent to a M_w 4.8 overlapping in time and space with the swarm-like seismic sequence

reported for 2013–2014. Gualandi et al. (2017) identified the slip to occur within shallow depths between 0 and 5 km, along two high-angle faults within the HW of the LANF. The swarm-like seismic activity linked with the transient deformation was studied using a high-resolution earthquake catalog from 2010 to 2014 (Valoroso et al., 2017). This study revealed a complex mixed mode seismicity (Valoroso et al., 2017). More recently, Vuan et al. (2020) used template matching (TM) to better characterize the seismicity adjacent to the LANF surface and found several productive clusters indicating a time intermittent activity rate, indicative of an interaction with $M > 3$ earthquakes and slow deformation occurring within the HW.

Despite the studies cited above, several questions regarding the mechanical behavior of the ATF-system remain open. A first open question is how the accommodated stress within the study area is released, either by continuous deformation along the LANF (Anderlini, Serpelloni, and Belardinelli, 2016), transient deformation within the HW (Gualandi et al., 2017), or a complex interplay of both mechanisms (Vuan et al., 2020). Another open question concerns the driving mechanism of the swarm-like seismic sequences within the HW, and more in particular if seismicity is controlled by aseismic slip, fluids or elastic interaction (Chiaraluce et al., 2007; Chiodini et al., 2004; Duverger et al., 2018; Gualandi et al., 2017; Martínez-Garzón et al., 2021; Ruhl et al., 2016; Valoroso et al., 2017).

To tackle the aforementioned challenges, we first derive a new high-resolution catalog of small earthquakes. This extended catalog is produced using a TM approach (Gibbons and Ringdal, 2006) applied to an array of borehole stations Chiaraluce et al., 2014 recording high-frequency (sampling rate of 500 Hz) and low noise data (Figure 3.2a). Starting from an initial catalog of $\sim 30,000$ earthquakes we detect more than 400,000 new events with magnitude as low as -2 . We further analyze the detected seismicity in terms of event interaction in time and space, and systematically search and model repeating earthquakes (RE), to infer the role of creep along the LANF (Nadeau and McEvilly, 1999). We finally propose models to reconcile the observed seismological behavior and reveal a complex coexistence of different processes along the ATF fault system.

3.2 Detection of Seismicity

To enhance the detection of small earthquakes and improve the time resolution of the seismicity in the study area, we make use of TM (Gibbons and Ringdal, 2006) and apply this array processing approach to data recorded at a network of seismic borehole stations as seen in Figure 3.1a (Chiaraluce et al., 2014). Our analysis covers a time period from July 2012 to December 2015, which includes a transient aseismic deformation signal (Gualandi et al., 2017) that coincides with a major earthquake swarm (Valoroso et al., 2017).

The seismic network used in this study is installed within three boreholes (Figure 3.2a) two of them having one surface station and one deep station (stations TB01 and TB02), and one borehole with a surface station plus 3 stations at different depths inside the borehole (station TB03). After quality control of the data, including visual inspection in time and frequency domain, we noticed that surface stations show a general high level of noise with a daily variation. Additionally, the continuous data is contaminated by artifacts and spikes. As these spurious signals are not consistent over different stations, we speculate that they originate from a source close to the sensor, probably related directly to the sensor or the digitizer. We further observe that the deepest stations are much more sensitive to small magnitude events,

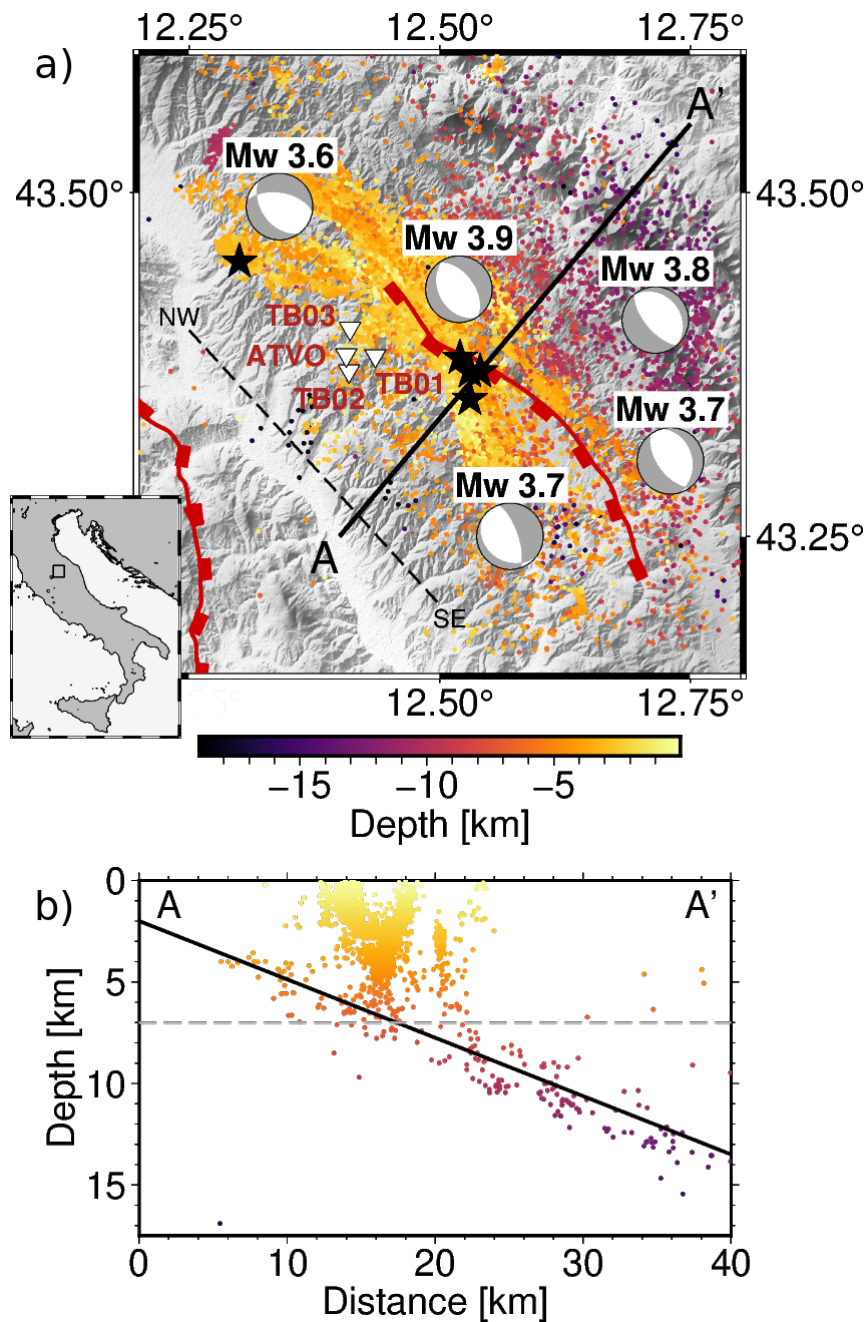


FIGURE 3.1: (a) Map of the study area in Italy. Triangles show the locations of the borehole stations (TB0X) and one surface station (ATVO). To indicate depth, the seismicity is color-coded. The locations of the five largest events during the study period are indicated a black stars, while their focal mechanisms are indicated by beach-balls. Red lines indicate the surface traces of the LANF (SW) and the Gubbio fault (central part) and are taken from Van Gessel et al. (2021). Dashed line indicates the projection along strike for Figure 3.3. (b) Cross-section of the study area as indicated in (a). Solid line indicates the fault surface of the LANF while the dashed line indicates the separation depth used in this study.

as illustrated in Figure 3.2a. We thus focus our analysis on four seismometers (3-components each) located at depth (TB01 (180 m), TB02 (210 m), TB03 (150 m), and TB03 (250 m)) with interstation distances ranging from 2.4 to 3.4 km. For all mentioned stations the data was sampled at 500 Hz throughout the duration of the study period.

The continuous data is analyzed using a TM technique (Gibbons and Ringdal, 2006), which has been shown optimal to detect small signals with extremely low signal to noise ratios (SNR) (e.g., Beaucé and Frank, 2018; Beaucé et al., 2019; Sánchez-Reyes et al., 2020). In TM, the P and S waveforms of known earthquakes (templates) are component-wise extracted with a distinct window length (see below) and then correlated with continuous data. At each time step, the correlation coefficient (CC) between the template window and the continuous data is calculated. This is done for each station and component, and finally averaged over all used components. A new detection is defined when the averaged CC reaches a certain threshold (e.g., Beaucé and Frank, 2018; Beaucé et al., 2019; Sánchez-Reyes et al., 2020). Here, this threshold is set to be 10 times the median absolute deviation (MAD) of the averaged CC for a specific template on a certain day.

To prepare TM, the first step of our data processing consists in preparing the continuous seismic data. The daily traces are synchronized to provide seismograms of 24 hr starting at midnight. The data is then detrended, filtered from 5 to 49 Hz using a Butterworth filter, and resampled at 100 Hz. The frequency band used here differs from earlier studies within the study area (e.g., VanderPlas, 2017) and permits the detection of low magnitude events (Cabrera, Poli, and Frank, 2022), as they are expected to have better SNR at higher frequencies (Abercrombie, 2021). Furthermore, by using 5 Hz as the lower corner frequency, we avoid systematically observed local noise which is strong in the frequency range from 1 to 5 Hz (Cabrera, Poli, and Frank, 2022; Latorre et al., 2014; Poli et al., 2020; Sánchez-Reyes et al., 2020).

In a second step, we extract the potential templates from the continuous data. For this we use the earthquakes from the catalog of Valoroso et al. (2017) (Figure 3.1a; Figure 3.2). For the time period (July 2012 until December of 2015) the catalog contains 34,923 events, which are precisely relocated using a double difference approach (Valoroso et al., 2017). In our work, we define a template as 1.2 s long P and S waveform, starting 0.4 s before the theoretical arrival time at each seismometer. The arrival time at each seismometer is predicted with a local 1D velocity model, which permits the extraction of seismic phases at each station (Chiaraluce et al., 2007, Table S1 in Supporting Information A). P waveforms are extracted from the vertical seismometer component, while the S waveforms from the horizontal components. For each potential template we calculate the root-mean-square (rms) amplitude within a noise window (1.2 s long time window previous to the P wave arrival) and relate this to the rms amplitude within the P and S wave windows to obtain the SNR for each template. Only templates with a $\text{SNR} > 3$ at more than 8 seismometer components are retained for further analysis. This step reduces the number of templates for the final run to 28,903.

We then use each template to scan the daily continuous data with a sliding window of one sample. This computation implies the calculation of $\sim 10^{15}$ correlations. To perform this large analysis, we use the Fast Matched-Filter (FMF) code of Beaucé and Frank (2018) based on a parallel GPU framework. The processing required 2,800 hr of computation, performed using a single NVIDIA Tesla V100 GPU with NVLink. For each template we obtain daily traces of CC averaged over all seismometer components, which are then used to extract new detections. To identify new detections, we first estimate the MAD for each daily trace of average CCs, and then define a

new detected event when the averaged CC at a sample exceeds the daily MAD by a factor of 10. This preliminary threshold was chosen from tests made with a subset of data, using low SNR templates. With these parameters we obtain a first set of detections, which includes redundant ones (e.g., new detections identified by multiple templates). This redundancy results in event detections with an interevent time smaller than the template window length (1.2 s). Therefore, we decluster this first set of detections using the interevent arrival time at the seismometer network. In this study we retain events with an average interevent arrival time at the network larger than 1.2 s, which corresponds to the window length of the template. This approach allows to detect events with interevent times even below 1.2 s, if the hypo-central distances between these events are large enough. Within a group of redundant detections, the CC ranges from ~ 0.2 to values of up to one if an auto-detection is included. In each group of redundant detections, we retain only the one with the highest CC for the final extended catalog. After declustering the extended catalog consists of 630,265 detected events, that is 21 times the number of events within the initial catalog.

Each newly detected event is assigned to the location of the template which detected it (Valoroso et al., 2017). We estimate the magnitude of a newly detected event by measuring the ratio of the waveform amplitudes between the template and the newly detected event (Cabrera, Poli, and Frank, 2022; Peng and Zhao, 2009). The ratio is taken from the mean value of the absolute signal within a window length of 1.2 s during the P-arrival on every component. Then, the new magnitude is estimated by adding the logarithm to the base of 10 of the median ratio of all components to the template's magnitude. This approach assumes a change of 10 in the amplitude as a change of 1 unit in magnitude (Cabrera, Poli, and Frank, 2022; Frank, Poli, and Perfettini, 2017; Peng and Zhao, 2009).

We subsequently perform quality control on the extended catalog, to ensure that only real detections of good quality are included. This step involves visual inspection of events detected by single templates (Figure 3.2b). We thus plotted 10 s of the waveforms for all detections made by one template sorted by a decreasing CC to MAD ratio as seen in Figure 3.2b. New detected events above the dashed line have a ratio > 12 , while detections above the solid line have a ratio > 11 . From Figure 3.2b, we see clear P wave arrivals for the first 30 detections, while the quality of detected signals reduces around detection number 40. The S wave arrivals are generally more prominent and can be seen for almost all detections, with significant quality reduction below a ratio of 11.

We performed the aforementioned procedure of visual inspection on randomly chosen families. The approach led us to the choice of retaining only detections with a CC to MAD ratio > 12 as new events which is in good agreement with other studies based on TM (Sánchez-Reyes et al., 2020; Shelly, 2020). This choice leads to a final catalog of 447,834 events which is an extension of the initial catalog (34,923 events) by a factor of ~ 12 , in agreement with studies from other areas using a similar approach (e.g., Gibbons and Ringdal, 2006; Sánchez-Reyes et al., 2020; Shelly, 2020).

3.3 The Extended Seismic Catalog

From 28,903 templates we were able to retrieve 447,834 events. A comparison of the time and space evolution of the new events is reported in Figure 3.3, together with the initial catalog (Valoroso et al., 2017). The extended catalog contains one

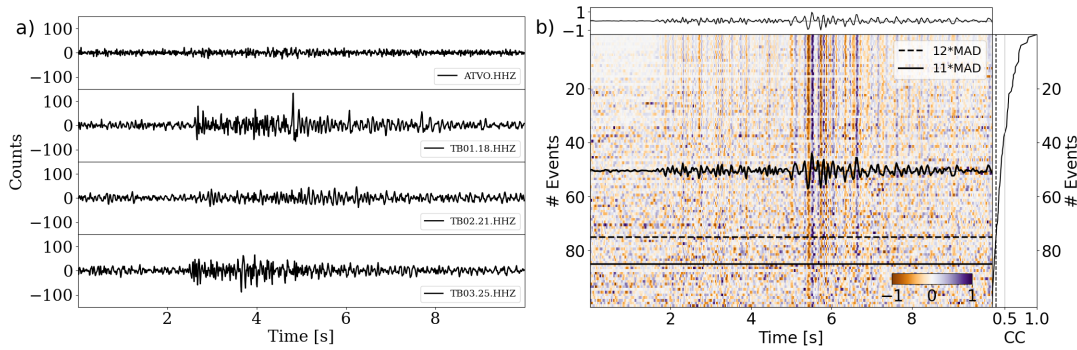


FIGURE 3.2: (a) Waveforms of a $M \sim -1.8$ event, recorded at the vertical components of the stations indicated in Figure 3.1a. The event occurred on 2013-04-21T20:15:15 northeast of the station array. (b) Waveforms of all detections made by a template event (2013-12-23T17:02:05, $M_w = -0.98$), normalized by their absolute maximum (recorded at TB01.BHZ). The waveform of the template event is indicated in the upper panel. Right panel shows the average correlation coefficient (CC) between the new detections and the template event. As indicated in the right panel, the normalized waveforms are sorted by a decreasing ratio between the average correlation coefficient and the median absolute deviation (MAD) of the daily average correlation coefficient. The horizontal dashed and solid lines indicate ratios of 12 and 11, respectively. A stack of the normalized waveforms of all events is indicated at Event 50 in black.

order of magnitude more events than the initial one, while it preserves a similar time evolution for the cumulative number of events (Figure 3.3a). This is seen as a first order quality estimate, as it reproduces the overall evolution of the seismicity.

The fact that the number of new detections is not constant over the analyzed time is an intriguing characteristic of the extended catalog (Figure 3.3a). The cumulative event number of both catalogs follows the same time evolution in the first part of the studied period, up to December 2013, with the extended catalog containing 10 times more events than the initial one (Figure 3.3a, note the different y-axis). However, in January 2014, the ratio of new events to templates events exceeded 10 (Figure 3.3a). To ensure that this evolution of the cumulative event number is not related to changes in data quality we inspected the continuous data related to the days in late December 2013 without finding anomalies. This increment is thus reflecting a true seismicity increase. Indeed, the extended catalog has a potential time resolution below 1.2 s, which allows to resolve events with very short interevent times (Figure S1 in Supporting Information A), of even less than 2 s (Figure S2 in Supporting Information A). This aspect has a significant impact on the increment factor we obtained, which allows to resolve an extremely high seismicity rate as in January 2014 (Figure 3.3), and therefore enables us to resolve the small-scale spatio-temporal evolution.

We additionally observe 4,157 periodically activated events (Figure S3a in Supporting Information A) at along strike distance approximately -15 km (Figure 3.3b) within the extended catalog. These events were detected by templates located at shallow depths (between 0.09 and 1.9 km) within a small region at the southern end of the Gubbio basin close to a cement factory. The waveforms of these events (Figure S3b in Supporting Information A) consist mainly of low frequency signals similar to the events observed by Lambotte et al. (2014). In the following analysis, we removed these events, as they can be considered as a nuisance for earthquake related studies (Gulia and Gasperini, 2021). However, human made signals can potentially be used

to monitor changes in physical properties in the fault system, using recently proposed correlation approaches (Pinzon-Rincon et al., 2021).

In Figure 3.4a we compare the frequency-magnitude distribution of the extended and the initial catalog (Valoroso et al., 2017). Even though both catalogs share a similar slope, the estimated magnitude of completeness (Herrmann and Marzocchi, 2021) decreased from 0.39 for the initial catalog to -0.67 for the extended one (Figure 3.4a).

Figure 3.4b further compares the estimated magnitudes with the magnitudes of the initial catalog as a function of time. This figure again reveals the improved magnitude resolution of the extended catalog, and its capability to resolve in detail the large number of events associated with each burst of seismicity (Figure 3.4b). There is however in both catalogs a daily evolution of minimum resolved magnitude, with smaller magnitude events better detected during nighttime (Figure 3.4b inset). This phenomenon was already seen in another TM study (Sánchez-Reyes et al., 2020) and might be due to daily anthropogenic noise variation (Poli et al., 2020). This should be considered for example, while performing statistical analysis of the seismicity (e.g., Marsan and Nalbant, 2005). A further issue in the presented approach is the limitation to a borehole station network consisting of only four sensors (12 channels). During periods when no data is available for more than one station, the results of TM are less reliable, and are therefore not included within the extended catalog presented here. Especially during early 2013, figures 3.3b and 3.4b show several gaps of data indicated by vertical empty lines.

The results of the extended catalog can be partially compared with a previous study (Vuan et al., 2020), where the authors applied TM using events nucleating within 1,500 m from the assumed ATF surface to detect $\sim 16,000$ earthquakes within our study period. With the TM approach presented here we are able to detect 32,158 events nucleating in the same fault volume, which is more than twice the number of events detected by Vuan et al. (2020). We postulate that the reason for the improved performance in this study is related to the use of a higher frequency band and the higher sampling rate, which allows to better detect small magnitude events. Additionally, the borehole data used in this study seems to be less sensitive to noise (Chiaraluce et al., 2007), and therefore better resolve the micro-seismicity nucleated from the deeper parts of the LANF.

Even though we are able to detect a large amount of new seismic events from areas where templates are available, the inherent disadvantage of TM is its blindness in areas where no seismicity, or any other signal was previously identified. This represents the weak point of TM compared to other detection methods like used by Majstorović, Giffard-Roisin, and Poli (2021) which do not rely on previously characterized events from distinct areas. The extended catalog is available in electronic format (see Data Availability Statement).

3.4 Time and Space Evolution of the Seismicity

In the following, we use the extended catalog containing 443,677 events (without the 4,157 human induced sources) to derive new insights about the dynamics of the seismicity, to shed light on deformation processes and infer mechanical properties of the ATF fault system.

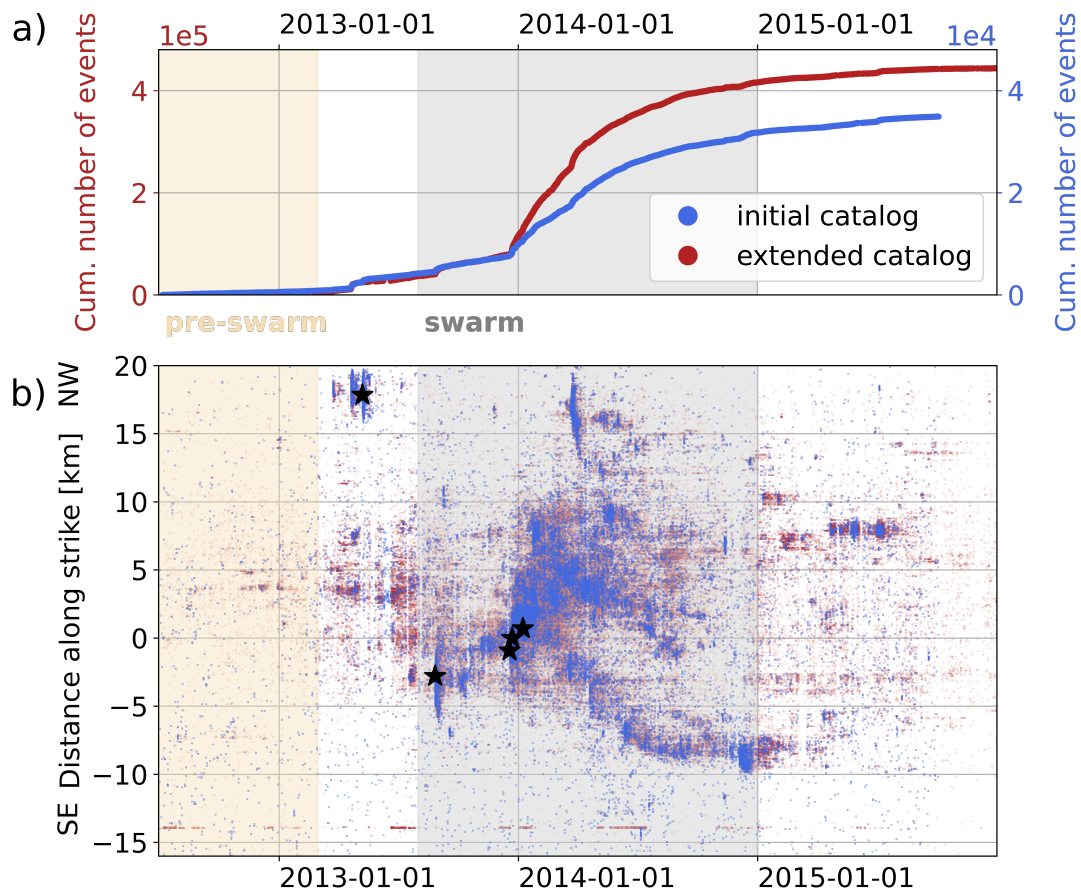


FIGURE 3.3: (a) Cumulative number of events for the initial (blue) and the extended (red) catalog. Note the two different scales. Two distinct time periods (pre-swarm and swarm) of distinctive style of seismicity are indicated. (b) Space-time evolution along strike as indicated in Figure 3.1a, for the initial (blue) and the extended (red) catalog. Black stars mark the five largest events within the study period (Figure 3.1a).

3.4.1 Time and Space Clustering of the Seismicity

We begin the analysis by assessing the interaction in time and space between seismic events. The presence (absence) of earthquakes clustering provides fundamental insights into the dynamics of seismicity and rheological properties of fault systems, as revealed from seismological studies (Liu et al., 2022) and numerical modeling (Dublanchet, Bernard, and Favreau, 2013). The simplest mechanism of time and space clustering of earthquakes is through interactions between events during co- and post-seismic processes, like static or dynamic stress transfer triggering (Freed, 2005) or afterslip (Perfettini and Avouac, 2004), with additional modulation related to the asperity density (Dublanchet, Bernard, and Favreau, 2013). Alternatively, enhanced interaction can result from external forcing as slow aseismic deformation (Frank et al., 2016; Lengliné et al., 2017; Poli et al., 2022), fluid fracturing (Obara, 2002; Seno and Yamasaki, 2003) or coupled fluid and rock interaction (Shelly et al., 2006), in complex fault systems (Dublanchet, Bernard, and Favreau, 2013).

We start by dividing the seismicity into pre-swarm (beginning of the catalog until 2013-03-01) and swarm (2013-08-01 until 2014-12-31) periods (Figure 3.3), guided by the results of Gualandi et al. (2017) and Valoroso et al. (2017). Then, to assess the time and space interaction during these two periods, we discretize the seismicity in space using 1 km bins along depth, as well as along strike. Finally, for each bin we count the number of events occurring in each time bin of 1-hr.

We start by evaluating the spatial population dynamics (Bjørnstad, Ims, and Lambin, 1999), to retrieve synchronous populations of earthquakes. To that scope, we compute the zero-lag cross-correlation (ZCC) between the event count time series defined above (Figures 3.5a and 3.5b). The resulting ZCC is expected to be high for time series having similar time evolution, thus indicating synchronous activation over different space bins (Bjørnstad, Ims, and Lambin, 1999; Frank et al., 2016; Trugman et al., 2015; Wu et al., 2015).

Figure 3.5a shows the results of our analysis, for the pre-swarm period. Here, small ZCC off the diagonal are observed for the full depth range, suggesting marginal spatial interaction. A similar behavior is observed for the along strike interaction (Figure 3.5d). On the other hand, during the swarm period we observe a systematic increase of space synchronization both in depth (Figure 3.5b) and along strike (Figure 3.5e). During the swarm period, we additionally observe that the synchronization is reduced at depths of ~ 7 km, indicating a less spatially clustered seismicity (Figure 3.5b). This depth limit is also associated with the base of the Mesozoic carbonates and Triassic evaporitic rocks (Chiaraluce et al., 2007; Piana Agostinetti, Giacomuzzi, and Chiarabba, 2017; Piccinini et al., 2003). It is worth mentioning here that the seismicity below 7 km depth, mainly consists of events nucleating along the ATF volume (Figure 3.1).

We further assess the time interaction of the seismicity along depth, considering a point process formalism (Lowen and Teich, 2005), and the autocorrelations of the event count time series. If the auto-correlation function exhibits a distinct pulse at zero lag-time, the seismicity is temporally unrelated as expected for a Poisson process like random seismicity (Lowen and Teich, 2005). On the other hand, a smooth drop of the auto-correlation function indicates an auto-regressive model, in which the time of future earthquakes is related to the previous ones (Lowen and Teich, 2005). Figure S4a in Supporting Information A shows the auto-correlation functions along depth for the pre-swarm period. Here the pulse at zero lag-time indicates Poissonian-like evolution of seismicity over the entire depth range. For the swarm period (Figure S4b in Supporting Information A), we again distinguish

two behaviors. The shallow seismicity (above 7 km depth) is characterized by an auto-correlation function with a smooth decay around zero lag-time, indicating a significant time interaction. On the other hand, for the deeper part, below 7 km, the auto-correlation functions show a zero-lag pulse, as seen for the entire depth range in the pre-swarm period (Figure S4 in Supporting Information A).

We additionally explore the time interaction of the seismicity occurring in each space bin (Figure 3.5c and 3.5f), by calculating the coefficient of variation (COV) of the interevent times. The COV provides insightful information about the time clustering of earthquakes (e.g., Cabrera, Poli, and Frank, 2022; Kagan and Jackson, 1991; Sánchez-Reyes et al., 2020; Schoenball and Ellsworth, 2017). A COV of ~ 1 indicates a Poissonian-like distribution of the interevent times while a COV > 1 indicates temporal clustering, indicative of high interaction between events. Note that for this step we employ the same time separation (before and during the swarm) applied in the previous approach but use the interevent time of events in different depth bins, thus exploring the time clustering at time scales even smaller than 1-hr.

Figure 3.5c shows the COV over the depth bins for the pre-swarm period (blue line) and the swarm period (red line). Over the whole depth range, the pre-swarm period exhibits quasi stable values less than 2. For the swarm period, we can distinguish between two different regimes. The shallow part above 7 km exhibits values larger than two indicating an enhanced interaction between events. However, the deeper part below 7 km remains at pre-swarm values.

The COV along strike is generally higher during the swarm phase (Figure 3.5f). Furthermore, during the swarm period (Figure 3.5f), the COV is particularly large for regions also showing significant spatial clustering (Figures 3.5e and 3.5f).

In summary, the spatio-temporal analysis reveals a strong interaction in time and space (Figure 3.5; Figure S4 in Supporting Information A) occurring during the swarm period. This clustering is observed to decay as function of depth, with seismicity deeper than ~ 7 km, nucleating along the low angle normal, beginning to be less clustered in time and space (Figure 3.1; Figures 3.5a-c).

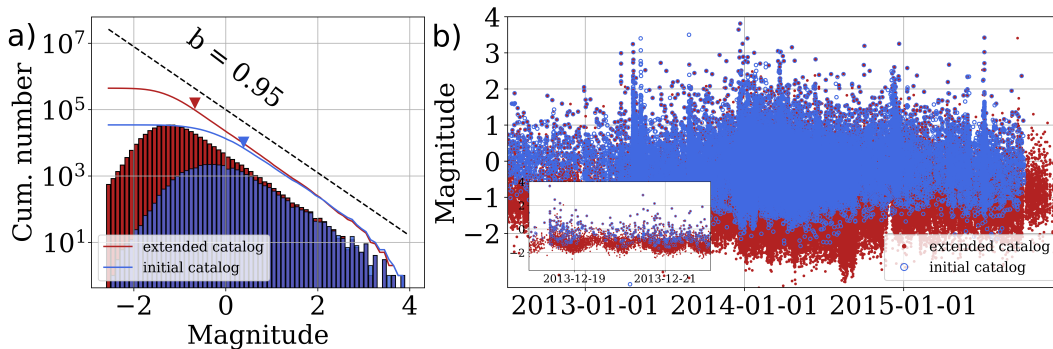


FIGURE 3.4: (a) Frequency-magnitude distribution for the initial (blue) and the extended (red) catalog. Continuous lines indicate the cumulative distributions while the dashed line indicates the b-value of the initial catalog (Valoroso et al., 2017). Triangles indicate the magnitude of completeness estimated following the approach of Herrmann and Marzocchi (2021). (b) Magnitudes as a function of time for the initial (blue) and the estimated magnitudes for the extended (red) catalog. Inset: As (b), for the time period from 2013-12-18 to 2013-12-22.

3.4.2 Temporal Behavior of Template Families

We further focus on the characteristics of event families. Similar to previous studies (e.g., Cochran et al., 2018; Shelly and Johnson, 2011), a family is defined as all detections made by a certain template. From Figure 3.2b it is visible that the normalized waveforms of new detections within a family share similar features with their template. This indicates qualitatively the spatial proximity of the events belonging to a particular family. To further quantify the distances between events within a family, we take advantage of the redundant events reported in Section 3.2. We therefore consider events which were used as templates, and at the same time detected by other templates. As for these templates we know the precise location, we can calculate the hypo-central distances between the location of the auto-detection (i.e., a template detects the event which it was extracted from) and the locations of all additional templates, which detected this particular event. From the distances, we obtain a first order estimate of the volume a template is sensitive to. We perform this analysis for 2,052 cases of redundant detections which corresponds to $\sim 5\%$ of the catalog (Figure S5 in Supporting Information A). Figure S5 in Supporting Information A shows that in certain rare circumstances, templates located up to 3 km away from another event may still detect it. However, $\sim 80\%$ of the redundant events have distances smaller than 1 km to the template. We therefore assume that hypo-central distances between events and their detecting template can be expected to be approximately 1 km. This leads us to the consideration that a family of events allows us to probe the time evolution of asperities that are close to each other, in a localized zone of the fault (e.g., Cochran et al., 2018).

Guided from the results of Section 3.4, we study in more details the properties of families in the shallow (<7 km) and deeper (>7 km) fault system (Figure 3.1; Figure 3.5; Figure S4 in Supporting Information A). We emphasize once more that this separation is guided by the change in spatial and temporal clustering that we resolved (Figure 3.5; Figure S4 in Supporting Information A), and isolate events along the low angle normal fault (>7 km, Figure 3.1) from earthquakes occurring both along the low angle normal fault and along high angle syn- and antithetic faults (<7 km, Figure 3.1). For each family, we estimate the interevent times, and normalize them by the total duration of each family. The resulting normalized interevent times (τ) are then sorted within logarithmic time bins and counted. We account for logarithmic spacing, by dividing the number of normalized interevent times per bin by the length of the bin and the total number of normalized interevent times (Duverger et al., 2018). This processing provides the interevent time distributions for the two distinct depth range, as shown in Figure 3.6a. Their general shape can be described with a truncated gamma distribution:

$$\rho(\tau) = C(\tau)^{\gamma-1} e^{-\frac{\tau}{\beta}} \quad (3.1)$$

where C and β are constant while γ indicates the time clustering of the seismicity (Hainzl et al., 2006). For $\gamma = 1$ the seismicity is Poissonian-like and therefore occurs randomly in time, while for $\gamma = 0$ it follows a power-law decay similar to an Omori-like sequence (Duverger et al., 2018; Omori, 1894; Poli et al., 2022).

For families of the shallow part (above 7 km depth; Figure 3.6a) the interevent times linearly decay over four orders of time magnitude and can be fitted (Equation 3.1) with $\gamma \sim 0.26$. This value of γ is indicative of seismicity clustered in time (Duverger et al., 2018; Poli et al., 2022), but differs from classic aftershock sequence (e.g., Omori, 1894). The influence of different separation depths can be seen in Figure S7 in Supporting Information A.

For the deep families (below 7 km depth; Figure 3.6a) we observe a clear change of the slope at $\tau \sim 10^{-2}$. This change of the slope is indicative of a bi-modal behavior of the seismicity, similarly to the observations of Thomas et al. (2018) for low frequency earthquakes (LFE). More in particular, for $\tau < 10^{-2}$ the distribution decays with $\gamma = 0$ indicative of an Omori-like process (Omori, 1894). On the other hand, for $\tau > 10^{-2}$ the seismicity becomes less time clustered, with $\gamma = 0.55$.

To visualize the behavior of distinct time clustering discussed above, in Figures 3.6b–d we show the cumulative number as function of time, for the deep and shallow seismicity. We therefore separate the seismicity of the deep families according to their absolute interevent times (short (< 104 s) and long (> 105 s) interevent times, Figure S6 in Supporting Information A). We can clearly see that the temporal clustering shown in Figure 3.6a is mostly associated with the intermittent occurrence of quick bursts of deep seismicity with short interevent time intervals (Figure 3.6b). In contrast to that, the seismicity with long interevent time intervals evolves with a nearly constant rate for the whole duration of our study period (Figure 3.6c). After the increase in occurrences in January 2014, the seismicity associated with shallow families decays in time, following an Omori law, without however being governed by a large mainshock (Figure 3.6d), similar to observations of other swarms (Poli et al., 2022).

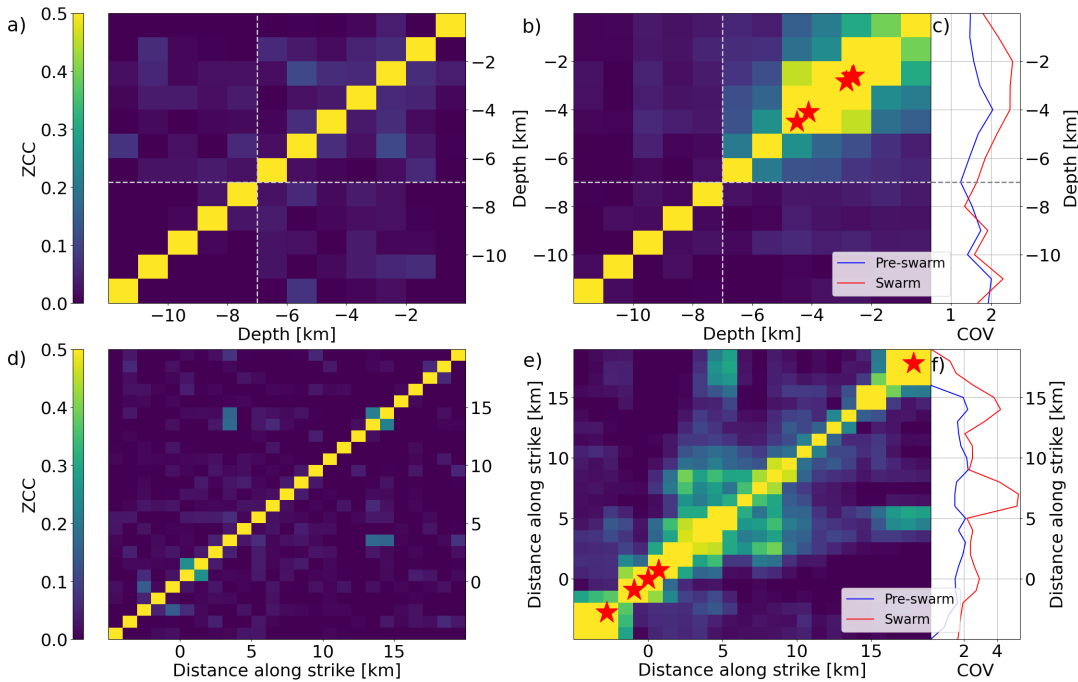


FIGURE 3.5: Pairwise zero-lag cross-correlation (ZCC) between the event count time series binned in 1 km along depth and 1-hr lasting time bins for (a) the pre-swarm and (b) the swarm time period. Red stars indicate the largest events of the sequence. (c) Coefficient of variation (COV) of the interevent times for 1 km depth bins for the pre-swarm (blue) and the swarm (red) period. In (a), (b), and (c) the dashed gray lines indicate the separation depth for Section 3.4.2. (d) Pairwise ZCC between the event count time series binned in 1 km along strike and 1-hr lasting time bins for the pre-swarm and (e) the swarm time period. Red stars indicate the largest event of the sequence. (f) As (c), for along strike bins.

3.4.3 Repeating Earthquakes (RE) Along the LANF

One of the proposed mechanisms for explaining the accommodation of the extension inside the study area is gradual creep along the LANF (Anderlini, Serpelloni, and Belardinelli, 2016; Vadacca et al., 2016). Creeping faults are widely recognized for producing RE: earthquakes with waveforms that are remarkably similar, radiated from asperities that are brought to failure by the loading caused by creep in the surrounding area (Nadeau and McEvilly, 1999). RE have been observed along the ATF (Chiaraluce et al., 2007), with recurrence times ranging from seconds to minutes (Valoroso et al., 2017), and are thought to be the result of creep (Anderlini, Serpelloni, and Belardinelli, 2016). Several studies, however, have found that RE with short recurrence times are difficult to link to creep (Chen, Bürgmann, and Nadeau, 2013; Lengliné and Marsan, 2009).

In this work, we systematically search for REs along the LANF (seismicity below 7 km) as evidence of creep, by correlating the waveforms of events. We follow the approach of Duverger et al. (2018) and estimate the similarity value between event pairs over the entire station network, while considering the SNR of each component. It is worth mentioning that here we limit our analysis only on waveform similarities, without any attempt to relocate highly similar events (Uchida and Bürgmann, 2019).

For each pair of events with a hypo-central distance of less than 750 m in between, we extract the waveforms on all 12 components and cut it into 9.5 s lasting windows (sampled at 500 Hz) starting with the p-arrival and including substantial portions of the s-coda (Figure 3.7a inset). The waveforms are filtered between 1.5 and 15 Hz (Duverger et al., 2018; Schaff and Waldhauser, 2005). The upper frequency is chosen to limit the effects of different source properties, that is, changes in stress drops and thus corner frequencies (Uchida, 2019). For every detection we estimate the SNR within a 0.5 s window before the P-arrival. We cross-correlate the waveforms component-wise and extract the maximum of the resulting cross-correlation function. This maximum is then averaged over the station network while values extracted from components with a low SNR are down weighted with a logistic function (Duverger et al., 2018, Equation 1 in Supporting Information A).

Next, we group events sharing a similarity value (> 0.95) following a simple equivalence class approach (i.e., if event A and B share a high similarity value, they open a family, if an additional event C shares a high similarity value with only one of the events A or B, it is grouped into that family).

This approach leads to 10 event families of similar events (Figure 3.7; Figure S8; Table S2 in Supporting Information A). The families consist of 2–3 events, with short recurrence times of seconds to hours (Figure 3.7b; Table S2 in Supporting Information A), in agreement with previous studies (Valoroso et al., 2017). From Figure 6d it is clear that families occur unrelated to the starting time of the swarm-like seismic sequence in the shallow part of the HW, while some of them seem to be correlated in time with the short duration bursts observed from the short-lasting template families (Figure 3.6b). To assess if the behavior of RE can be reconciled with fault creep (Anderlini, Serpelloni, and Belardinelli, 2016), we make use of the scaling relationship between moment (M_0) and recurrence time (T_r):

$$T_r \propto M_0^{\frac{1}{5}} \quad (3.2)$$

proposed by Nadeau and Johnson (1998) for the San Andreas fault. In order to scale the recurrence time (T_r^{norm}) to the creep observed in the ATF, we use the normalization from Chen, Nadeau, and Rau (2007), which was shown valid over many tectonic environments:

$$T_r^{norm} = T_r \left(\frac{V_f}{V_{parkfield}} \right) \quad (3.3)$$

In this study we use 2.3 cm/yr for $V_{parkfield}$ (Uchida, 2019) while 0.17 cm/yr represents the geodetic rate of the study area (V_f , Anderlini, Serpelloni, and Belardinelli, 2016).

The observed interevent times are several orders of magnitude smaller than the expected interevent times for constant creep of 0.17 cm/yr (Anderlini, Serpelloni, and Belardinelli, 2016), highlighting that the RE observed along the LANF are not necessarily driven by creep, as speculated in other studies (Anderlini, Serpelloni, and Belardinelli, 2016; Valoroso et al., 2017).

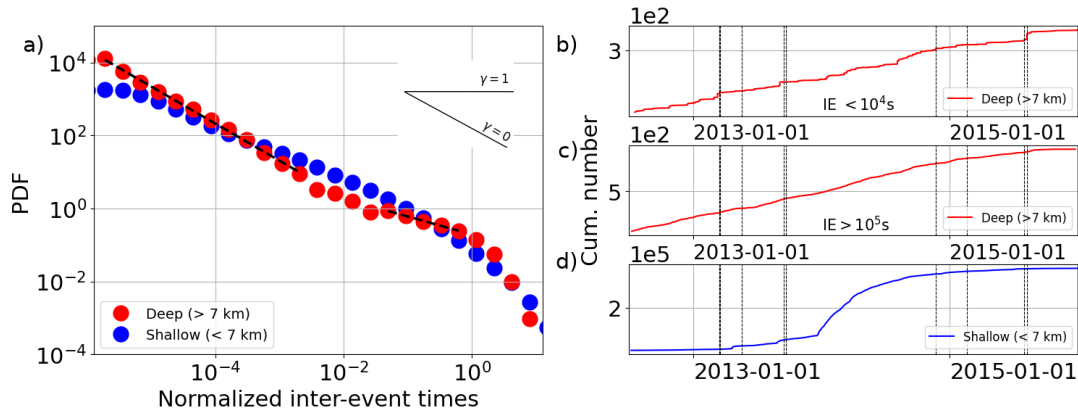


FIGURE 3.6: (a) Probability density function for the normalized interevent times of deep (red) and shallow (blue) template families. Dashed black lines indicate the least squares polynomial fit for the indicated areas. (b)–(d) Cumulative number for events for different areas and interevent times (IE). Vertical dashed lines indicate the origin times of repeating earthquakes (Section 3.4.3).

3.5 Discussion

From the study of spatial and temporal clustering of earthquakes along the ATF, we highlighted different styles of seismicity (Figure 3.5; Figure S4 in Supporting Information A). Deep seismicity (depth > 7 km) which includes only events nucleating along the LANF, exhibits marginal space clustering (Figure 3.5; Figure 3.6). Additionally, it is characterized by a bimodal time evolution, with short temporally clustered (Figure 3.6b) and long and non-temporally clustered (Figure 3.6c) seismicity. This result differs from a recent study (Vuan et al., 2020) which found the occurrence of swarms along the LANF as a function of activity within the HW.

At shallow depth (< 7 km), the Mesozoic carbonates and Triassic evaporitic rocks (Piana Agostinetti, Giacomuzzi, and Chiarabba, 2017) host clustered seismicity in time and space (Figure 3.5; Figure 3.6), which coincides in space with the aseismic deformation signal observed by Gualandi et al. (2017).

We here discuss in more details the different types of seismicity and the possible physical processes governing them.

3.5.1 The Shallow Seismicity

Shallow seismicity (depth < 7 km) is radiated by syn- and antithetic high angle normal faults (above the LANF, Valoroso et al., 2017), with notably high event rates only during the time period in which Gualandi et al. (2017) observed an aseismic deformation signal at 0 – 5 km depth. This seismicity exhibits significant spatial clustering, which implies a simultaneous activation of large fault portions of up to 4 km in depth and of up to 5 – 10 km along strike, over the time scale of 1 hr (Figures 3.5b and 3.5e).

The analysis of the interevent times (Figure 3.6a) and the time evolution of cumulative events (Figure 3.6d) reveal that the swarm seismicity mimics an Omori-like sequence, without however any clear large mainshock controlling this behavior. Additionally, $\gamma \sim 0.26$, obtained from Equation 3.1, does not support the hypothesis of stress transfer from large events to govern the evolution of the seismicity (Duverger et al., 2018; Poli et al., 2022).

The local space and time clustering can be controlled by elastic interaction and afterslip, which play a substantial role even for small magnitude seismicity (Fattahi et al., 2015; Helmstetter, Kagan, and Jackson, 2005). However, the observed rapid (1-hr) synchronization of seismicity is in many cases not associated with $M_w > 3$ earthquakes (Figure 3.5e) and difficult to reconcile with stress transfer or afterslip (Freed, 2005; Perfettini and Avouac, 2004). Even in the presence of $M_w > 3$ earthquakes capable of generating significant afterslip (Fattahi et al., 2015), the seismicity here is spatially synchronized on a length scale of up to 5 – 10 km (Figure 3.5). According to earthquake scaling relations (Mai and Beroza, 2000; Wells and Coppersmith, 1994), this is 5 – 10 times larger than the fault size expected for the largest events in the sequence.

The large-scale interactions (Figure 3.5) are more similar to observed spatial and temporal synchronization described by numerical models of seismicity in complex fault systems, where it is related to positive feedback in between seismicity and creep (Cattania and Segall, 2021; Dublanchet, Bernard, and Favreau, 2013).

The synchronization (Figure 3.5) observed for the shallow seismicity, is also similar to the behavior of LFEs observed in subduction or transform faults, during slow slip events (Frank et al., 2016; Tan and Marsan, 2020). We thus infer that the shallow seismicity can directly be used to assess the detailed spatio-temporal evolution of transient aseismic slip, not resolvable by daily geodetic measurements (Gualandi et al., 2017). Our interpretation further implies that the reported transient aseismic deformation is similar to the one observed in subduction zones. In our study area however, the distinct rheology of the shallow normal faults (Piana Agostinetti, Giacomuzzi, and Chiarabba, 2017), as well as lower temperature and pressure values do not permit the occurrence of tremors or LFE, but rather of regular seismicity.

Interestingly, the space and time clustering occur only during the aseismic deformation episode (Gualandi et al., 2017) (Figures 3.5c and 3.5f; Figure 3.6; Figure S4b in Supporting Information A), similarly to what is observed for LFE (Frank et al., 2016; Tan and Marsan, 2020). If stress transfer or afterslip from small events (Fattahi et al., 2015; Helmstetter, Kagan, and Jackson, 2005) were the only factor controlling the spatial or temporal synchronization on larger scales, this effect should be observable on a smaller scale for the seismicity outside of the swarm period, contrary to what we describe (Figure 3.5; Figure S4 in Supporting Information A).

The strong interactions observed (Figure 3.5; Figure S4 in Supporting Information A) also suggest the complexity of the fault system, which likely consists of groups of asperities along faults, or complex fracture networks in a fault volume

(Dublanchet, Bernard, and Favreau, 2013). In both cases, the resulting complex rheology is likely to inhibit the propagation of large magnitude earthquakes in the shallow syn- and antithetic faults (Dublanchet, Bernard, and Favreau, 2013).

Finally, we note that the absence of interaction during time periods outside of the transient aseismic deformation episode (Figure 3.5; Figure S4 in Supporting Information A) indicates a mostly coupled fault system within the shallow part of the study area, which is in good agreement with the results of Anderlini, Serpelloni, and Belardinelli (2016).

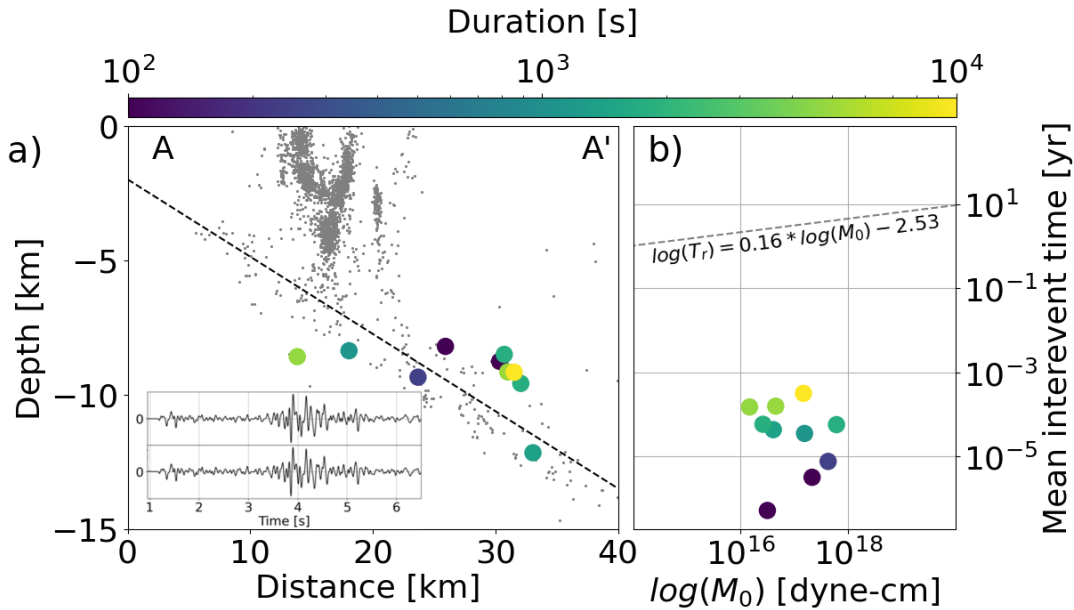


FIGURE 3.7: (a) Cross section of the ATF as seen in Figure 1b. Gray dots indicate the seismicity in vicinity to the cross section while the LNF model is indicated as a dashed line. Color-coded dots indicate the locations and the durations of the found families of similar events. The inset shows one event pair with highly similar waveforms (waveforms of all found event families can be seen in Figure S8a-j in Supporting Information A). (b) Mean interevent times as a function of seismic moment. In order to compare this relationship to other regions we normalized the mean interevent times by loading rates between California and the study area (Chen, Nadeau, and Rau, 2007; Uchida, 2019). Dashed line indicates the interevent times expected for a loading rate of 1.7 mm/yr. Color-coded dots as in (a).

3.5.2 The Deep Seismicity

At depths below 7 km, there is a significant change in seismicity style, with no large-scale spatial interaction (Figure 3.5) and much less apparent temporal interaction (Figure 3.5c; Figure S4 in Supporting Information A), both independent of the 2014 transient aseismic deformation episode (Gualandi et al., 2017). This observation indicates that the deeper part of the study area, related to the LNF, is not activated during the transient aseismic deformation episode (Gualandi et al., 2017) differently from what was discussed by Vuan et al. (2020).

We additionally observe that the deep seismicity follows a bimodal time evolution, with a small number of fast reoccurring events ($< 10^4$ s) exhibiting temporal

interaction (Figures 3.6a and b), and a larger number of events exhibit long-lasting reoccurring times ($> 10^5$ s) in a nearly constant time evolution (Figures 3.6a and c).

The systematic analysis of waveform similarities between events permitted to discovered 10 groups of RE. These events are used to clarify the role of creep along the ATF, in modulating their time occurrence. In Section 3.4.3, we utilize the scaling relationship suggested by Nadeau and Johnson (1998) and find that the interevent times do not necessarily match to the creep inferred using geodetic data (Figure 3.7, Anderlini, Serpelloni, and Belardinelli, 2016).

Short time intervals for RE were already observed by Valoroso et al. (2017) and seem to be comparable to the short-lasting event families we report (Figures 3.6a and b). The driving mechanism of these events could therefore be stress transfer on close asperities (Chen, Bürgmann, and Nadeau, 2013; Lengliné and Marsan, 2009). To test this hypothesis, we analyze the position of the largest events within each event family (Chen, Bürgmann, and Nadeau, 2013; Lengliné and Marsan, 2009), without recognizing any clear sign of mainshock aftershock behavior (Figure S9 in Supporting Information A).

The rapid recurrence of RE could be linked to the significant amount of high pore-fluid pressure observed in the ATF fault system (Piana Agostinetti, Giacomuzzi, and Chiarabba, 2017). Following the model of (Baisch and Harjes, 2003), multiple failures of the same asperity can occur for an increase of fluid pressure. These events (Figure 3.7) could thus represent a mode of rupture, fully driven by short lasting (10 – 1,000 s) pore pressure changes, as suggested by Collettini (2011). A simplified calculation of the pore pressure change can be done by dividing the cumulative stress drop for each family and assuming a coefficient of friction of 0.6 (Baisch and Harjes, 2003; Cochran et al., 2018). For a stress drop of 3 MPa, we obtain 10 – 15 MPa of pore pressure change over times ranging from ~ 10 to 1,000 s.

Together with the short bursts of events along the LANF (Figure 3.6c), we observe the occurrence of long-term and nearly continuous seismicity. This seismicity seems to agree with creep (Liu et al., 2022), as proposed by Anderlini, Serpelloni, and Belardinelli (2016). However, unlike many other well-instrumented creeping faults (e.g., Nadeau and McEvilly, 1999; Uchida, 2019; Uchida and Bürgmann, 2019), we found no evidence of RE sequences (Figure 3.7). This could be explained with general RE models (Chen, Nadeau, and Rau, 2007; Nadeau and Johnson, 1998), despite geological studies define the LANF as a continuously deforming ductile matrix with embedded lenses of competent material that represent seismically active asperities (Collettini et al., 2011). This model would thus predict the existence of RE, with the re-rupture of asperities driven by long term creep (Chen, Nadeau, and Rau, 2007; Nadeau and Johnson, 1998).

However, it should be noted that in such a fault model (Collettini et al., 2011) the role of heterogeneities in a large fault zone, can have an important role in controlling strain rate variability in space (Collettini et al., 2011; Fagereng and Sibson, 2010), and thus alter how RE occur. Thus, the lack of observed RE earthquakes can be only apparent, and result from the inaccuracy of the simple planar fault model used to predict the recurrence time (Figure 3.7, Chen, Nadeau, and Rau, 2007). A better understanding of fault properties, strain rate distribution and their control on eventually RE is hence required to better infer the role of creep (if any) along the Alto Tiberina LANF, and LANFs in general.

Alternatively, the lack of REs might challenge the creep model proposed for the Alto Tiberina LANF (Anderlini, Serpelloni, and Belardinelli, 2016). In this case alternative models that explain the observed surface displacement should be considered (Cianetti et al., 2008; Lambotte et al., 2014; Le Pourhiet, Burov, and Moretti,

2003). For example, a non-elastic volume at depth would concentrate the elastic strain upwards and produce similar surface displacement as observed for a creeping low angle fault (Lambotte et al., 2014). High temperatures can cause materials to become less viscous or plastic, which may be one of the reasons of the volume's origin (Lambotte et al., 2014). Within the study area, high temperatures could be the effect of rising CO₂ from the subducted mantle which is over-pressurized as it is trapped below the LANF (Chiodini et al., 2004). In this proposed model, the LANF accommodates little, if any deformation. Strain below the LANF would cause the continuous seismicity that we report (Cianetti et al., 2008).

3.6 Conclusion

By applying TM processing (Beaucé and Frank, 2018; Gibbons and Ringdal, 2006) to data recorded at an array of borehole stations we were able to produce a catalog of 443,677 earthquakes, expanding by ~ 12 times the number of events within the initial catalog (Valoroso et al., 2017). The new seismic catalog is complete to magnitude down to -0.67 .

While TM is powerful to detect many more events with low SNR, no objective method can be used to define a good and time consistent detection threshold. We therefore performed several quality controls on the detected signals to ensure to have a minimal impact of false detections in the extended catalog. With the presented approach we significantly improved the detection of small events, being able to detect earthquakes with magnitude as low as -2 (Figure 3.4). The extended catalog is available in electronic format (see Data Availability Statement).

The detailed analysis of this catalog enabled the identification of several types of seismicity in different parts of the fault system. We initially observe marginal temporal and spatial clustering along the whole fault system outside of the aseismic deformation episode (Figures 3.5a and d; Figure S4a in Supporting Information A). The shallow seismicity then begins to be strongly clustered in time and space, coinciding with the 2014 aseismic deformation episode (Gualandi et al., 2017). We propose that the enhanced interaction of seismicity reflects the complexity of the slip process during the transient (Cattania and Segall, 2021; Dublanchet, Bernard, and Favreau, 2013).

In the deeper part of the fault system, along the LANF, we observe bi-modal seismicity (Figure 3.6), with long and nearly continuous families of events, and short bursts with duration of less than 1 day. We further identified and modeled REs and illustrate the marginal role of creep in controlling their occurrence (Figure 3.7). We thus proposed rapid changes of pore pressure as driver of RE, which is in good agreement with geological studies (Collettini et al., 2002).

Finally, we show that RE are not a direct expression of creep and provide an alternative deformation model for the extension within the study area. This emphasizes that more seismo-geodetic studies are required to properly assess the deformation style occurring along the ATF during the inter-seismic periods (Anderlini, Serpelloni, and Belardinelli, 2016; Vadacca et al., 2016).

Chapter 4

Swarms as a Cascade of Aseismic Transients revealed by Unsupervised Clustering of Earthquakes: The Case of the Alto Tiberina 2014 sequence¹

Abstract

Earthquake swarms represent a particular mode of seismicity, not directly related to the occurrence of large earthquakes (e.g., aftershocks) but rather driven by external forcing such as aseismic slip or fluid migration in fault systems. Sometimes swarm occurrence overlaps with observable geodetic signals in space and time, indicating a direct link. However, the low resolution of geodetic observations tends to obscure small scale spatial and temporal dynamics of swarms.

In this work, we separate the 2014 Alto Tiberina swarm seismicity (Italy) into background and clustered seismicity using a spatiotemporal clustering approach, and further isolate single bursts of events. The quantitative characterization of each burst indicates that the whole swarm is composed of spatially and temporally confined (sub) swarms that could potentially be driven by aseismic slip. These findings are similar to findings during slow slip events in subduction zones.

¹Currently under review in *Journal of Geophysical Research: Solid Earth*. Essing, D., & Poli, P. (2023). Swarms as a cascade of aseismic transients revealed by unsupervised clustering of earthquakes: The case of the Alto Tiberina 2014 sequence

4.1 Introduction

Swarms are sequences of earthquakes with no obvious mainshock (Mogi, 1963; Vidale and Shearer, 2006). They show a delayed moment release with respect to their starting time (Chen and Shearer, 2011; Roland and McGuire, 2009), and have durations ranging from days to years (Passarelli et al., 2021).

Despite the lack of a mainshock that triggers the following events, swarms can be composed of hundreds or thousands of earthquakes (Chen and Shearer, 2011; Chen et al., 2017; Essing and Poli, 2022; Passarelli et al., 2021), which often show spatial and temporal organization (Chen and Shearer, 2011; Chen et al., 2017; Passarelli et al., 2021). The precise assessment of the observed spatial and temporal evolution of earthquakes composing the swarms has been used to assess the potential driving mechanism(s) of swarms (Hainzl and Ogata, 2005; Lohman and McGuire, 2007; Shapiro, Huenges, and Borm, 1997; Vidale, Boyle, and Shearer, 2006).

Fluid circulation is one of the possible mechanisms driving swarms (Hainzl, 2004; Shapiro, Huenges, and Borm, 1997). It is often resolved by a diffusive like migration of the seismicity (Shapiro, Huenges, and Borm, 1997). Alternatively, based on direct observations by means of geodetic data studies suggest that swarms could be associated with aseismic slip (Cappa, Rutqvist, and Yamamoto, 2009; Gualandi et al., 2017; Guglielmi et al., 2015; Hirose et al., 2014; Lohman and McGuire, 2007; Ozawa et al., 2003). While the aseismic moment is below the detection threshold in certain regions, linear migration patterns (Passarelli et al., 2018), and small effective stress drops (Fischer and Hainzl, 2017) are interpreted as evidence for aseismic deformation along faults. The role of aseismic slip in controlling the occurrence of swarms is also supported by source scaling studies (Passarelli et al., 2018), which suggest that tectonic swarms are similar to low frequency earthquakes during slow slip events in subduction zones (Frank et al., 2016).

Recent studies also suggest a model that combines fluid and aseismic slip as a potential driver of swarms (Cappa, Rutqvist, and Yamamoto, 2009; Guglielmi et al., 2015). In this case, fluids affect the fault properties by increasing the nucleation size of an earthquake, favoring the occurrence of aseismic slip, which then drives the observed seismicity, by stress changes ahead of the aseismic slip front (Cappa, Rutqvist, and Yamamoto, 2009; Guglielmi et al., 2015).

Despite their spatio-temporal complexities, the ensemble behavior of swarms often resembles an Omori-like sequence of earthquakes, indicative of the temporal clustering observed also for mainshock-aftershocks (MS-AS) sequences (Essing and Poli, 2022; Valoroso et al., 2017). However, recent studies highlighted the existence of multiple space and time scales in a single swarm, revealing significant insights about the physical processes driving swarms (Dublanche and De Barros, 2021; Essing and Poli, 2022).

In this study, we investigate the apparent simplicity of a swarm sequence by inferring its detailed spatiotemporal dynamics and obtain insights into the mechanisms that could be responsible for its occurrence. To that objective, we are focusing on identifying seismic bursts that were part of a large swarm that occurred in the Alto Tiberina Fault (ATF) System in the Northern Apennines in 2013/14 (Figure 4.1, Essing and Poli, 2022; Valoroso et al., 2017).

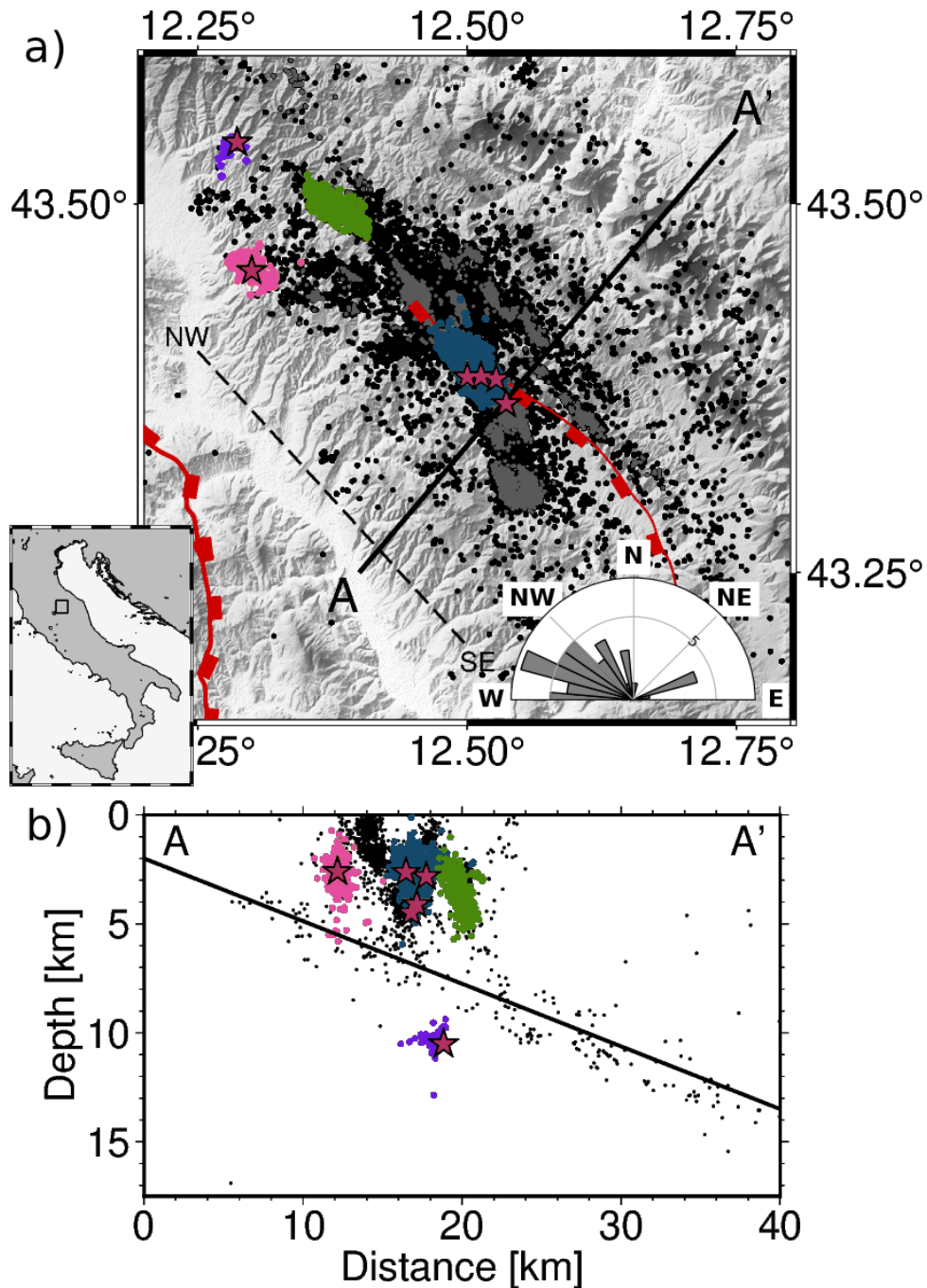


FIGURE 4.1: (a) Map of the study area in Italy. The un-clustered seismicity is plotted as black dots, clustered seismicity is plotted as dark-gray dots. Colored dots indicate bursts highlighted in figure 4.3a and b (pink dots are related to the Citta di Castello sequence, dark blue dots to a central burst, dark green dots to the Pietralunga II sequence, purple dots to an isolated sequence). Largest events ($3.5 < M < 3.8$) are indicated as stars. Red lines indicate the surface traces of the LANF (SW) and the Gubbio fault (central part) and are taken from Van Gessel et al. (2021). Dashed line indicates the projection along strike for figure 4.3a and b. Inset indicates the estimated strike angles for the resulting bursts. (b) A – A' cross-section. Seismicity within 0.5 km distance from A – A' is indicated as black dots. The highlighted clusters of seismicity in (a) are indicated in corresponding colors, as well as the largest events ($3.5 < M < 3.8$).

4.2 Seismo-Tectonic Setting

The ATF system consists of a major low-angle normal fault exhibiting a small dip angle ($< 30^\circ$). Between 3 and 6 km depth, its hanging wall (HW) consists of Mesozoic carbonates and Triassic evaporitic rocks dominated by a network of high-angle ($\sim 50^\circ$) normal faults (Piana Agostinetti, Giacomuzzi, and Chiarabba, 2017). The shallow part is characterized by high $v_p - v_s$ ratios, indicative of high pore-fluid pressure (Chiarabba and Amato, 2003; Piana Agostinetti, Giacomuzzi, and Chiarabba, 2017). This depth layer hosted several micro-seismic ($M_w < 4$) swarm sequences occupying large areas of the study area in 2001 (Piccinini et al., 2003) and 2014 (Chiaraluce et al., 2007; Valoroso et al., 2017). It further hosted sequences of minor extensions near the town of Pietralunga in 2010 (Marzorati et al., 2014) as well as near Citta di Castello in 2013 (Valoroso et al., 2017).

The 2014 swarm sequence was accompanied by a transient aseismic deformation signal detected with an independent component analysis of GNSS data (Gualandi et al., 2017). The deformation signal lasted ~ 6 months and produced a maximum cumulative surface displacement of ~ 3.3 mm. The measured surface displacement could be best explained by a model with two high-angle faults within the shallow HW (2 – 5 km depth) of the ATF. Interestingly, the released geodetic moment was two times larger than the released seismic moment indicating aseismic processes active within the study area (Gualandi et al., 2017).

Due to the small deformation signal of only ~ 3 mm, it is not possible to infer whether the aseismic signal was produced by pre- and post-seismic processes or was driving the increment of seismicity (Gualandi et al., 2017). To shed more light into the driving mechanism of the swarm seismicity, Essing and Poli (2022) produced a high-resolution earthquake catalog, obtained with a matched-filter approach using continuous seismic data from sensors installed within a borehole array. The analysis of the detected seismicity revealed significant spatiotemporal clustering occurring during the swarm sequence. In their work, especially the spatial synchronization of seismicity over distances of ~ 5 km in short time periods (1-hr) is used to argue that additional processes than only stress transfer triggering are driving the seismicity within the HW (Essing and Poli, 2022). Indeed, the findings were interpreted as complex stress interaction between aseismic slip and earthquakes in a fault network, which is in good agreement with numerical models (Cattania and Segall, 2021; Dublanchet, Bernard, and Favreau, 2013). The observed clustering additionally shares similarity with the behavior of low frequency earthquakes (Rogers and Dragert, 2003; Hirose and Obara, 2006) during aseismic slip events in the deep part of megathrust or transform faults (Frank et al., 2016; Tan and Marsan, 2020).

To better characterize the spatial and temporal clustering discussed above, and thus infer its driving mechanism, we here make use of a high-resolution seismic catalog (Essing and Poli, 2022), and unsupervised spatiotemporal clustering methods (Campello, Moulavi, and Sander, 2013; Davis and Frohlich, 1991), to isolate bursts of seismic events. For each burst we then assess its spatial and temporal evolution (Schoenball and Ellsworth, 2017), the effective stress drop (Fischer and Hainzl, 2017) and its scaling properties (Danré et al., 2022; Passarelli et al., 2018).

Previous studies related the overall swarm sequence of the study area to a major aseismic deformation signal (Essing and Poli, 2022; Gualandi et al., 2017). The analysis presented here further suggests that the detected large scale deformation signal is a composition of small scale aseismic transient processes indicated by seismic bursts which themselves interact. This finding is in a sense similar to processes related to slow slip events (Frank et al., 2016; Tan and Marsan, 2020).

4.3 Spatiotemporal Hierarchical Clustering

To resolve the apparent spatial and temporal bursts in the study area (Essing and Poli, 2022; Valoroso et al., 2017), we make use of an unsupervised clustering approach (Campello, Moulavi, and Sander, 2013). We therefore use the hypocenter location (latitude, longitude and depth) and the origin time of the earthquakes in the high-resolution catalog of Essing and Poli (2022) as input features for the clustering. In this section we describe the clustering approach and the feature preparation in detail.

4.3.1 Clustering

Clustering algorithms are generally used to identify subgroups in a feature space such that data points in the same subgroup (cluster) share similar features, while the features of data points in different clusters are different. Clustering methods include density-based clustering (Ester et al., 1996) and hierarchical clustering (Ward Jr, 1963), among many more.

In this study we exploit the combined space and time information (the feature space) to identify times of elevated seismicity rates localized in space. An elevated seismicity rate relative to background seismicity might originate from a variety of processes acting on different time scales, like MS-AS or swarms, as well as a non-stationary background seismicity rate driven by external forcing. To group the seismicity into meaningful clusters despite the variable spatial and temporal density, we follow an approach accounting for varying densities within the feature space, to define clusters. The presented approach is based on Hierarchical Density-based Spatial Clustering of Applications with Noise (HDBscan) and combines density-based with hierarchical clustering (Campello, Moulavi, and Sander, 2013).

Density-based clustering scans the feature space to isolate densely populated regions (Ester et al., 1996). This approach has already been applied to find groups of seismicity using the horizontal event locations (Schoenball and Ellsworth, 2017). The awareness of outliers is one advantage of density-based clustering approaches. Therefore, events do not necessarily have to be grouped into clusters but could potentially be identified as outliers. This is especially convenient to identify the abundant background seismicity active within the study area (Essing and Poli, 2022).

Hierarchical clustering (Ward Jr, 1963) starts with each event in its own cluster, while pairs of data points are merged into clusters as one increases the distance threshold in-between events within the feature space. This approach was already used to cluster seismic events depending on their pairwise waveform similarity (Sánchez-Reyes et al., 2020). The advantage over other clustering algorithms such as k-means (Lloyd, 1982) is that no predetermined number of clusters is required.

The first step in the clustering pipeline of HDBscan consists of the transformation of the feature space from the original space (Figure 4.2a) to the mutual reachability distance (d_{mr}) space (Eldridge, Belkin, and Wang, 2015) following

$$d_{mr}(A, B) = \max(\rho(A), \rho(B), d(A, b)) \quad (4.1)$$

where $d(A, B)$ is the direct distances between two points, and $\rho(A)$ the density at point A. Here, density is measured by the means of number of neighboring events within a certain distance.

This feature space transformation pushes data points in sparse areas farther apart, while leaving them untouched if located in dense areas. In that sense, isolated background seismicity that populates randomly the feature space in a sparse manner, is moved farther apart from denser populated areas.

Based on the d_{mr} space, the algorithm connects the nearest neighbors (edges) using Prim's algorithm (Prim, 1957). As exemplified in figure 4.2a, this results in a minimum spanning tree (MST).

The estimated MST can be directly converted into a hierarchy that can be represented by a dendrogram (Figure 4.2b). In figure 4.2b, events and group of events are connected according to their d_{mr} . Now, one could establish a d_{mr} threshold over which all events are disconnected. Events and groups of events below this threshold that remain connected then open clusters (Sánchez-Reyes et al., 2020). However, this approach using a global threshold might not be satisfactory as it does not account for different densities in the feature space. We expect the seismicity radiated from the study area to have different event densities in the feature space due to various processes like MS-AS, swarm sequences and a potential non-stationary background rate of seismicity. Therefore, by using HDBscan we can expand the clustering pipeline.

In figure 4.2b one can see that while lowering the mutual reachability distances from 90 to 50, single events split apart from the hierarchical tree, indicated as black lines. These are events that HDBscan classifies as outliers. By further lowering the mutual reachability distances from 40 to 30, one can see in figure 4.2b that entire networks (marked 1, 2, and 3) of events split apart. The implementation of the minimum cluster size hyper-parameter now allows to use these networks as potential clusters if the number of events within exceeds the introduced hyper-parameter (Campello, Moulavi, and Sander, 2013). With this step HDBscan condenses the built hierarchical tree (Figure 4.2c). The distance between clusters is now indicated by the inverse of the mutual reachability distance (λ), and potential clusters are represented by colored bars. The horizontal width of each bar in figure 4.2c indicates the number of events within, which decreases with the increase of λ , due to the drop out of single events.

In figure 4.2c one can see that five potential clusters exist depending on the decision whether to consider clusters with smaller λ values (parent cluster) or the descendant clusters with larger λ values (children cluster). HDBscan decides this in an automated way by estimating the stability of each cluster by comparing the $\sum(\lambda_p - \lambda_{birth})$ of the parent and the children clusters (Campello, Moulavi, and Sander, 2013). Here λ_p is the value at which a certain point splits off and λ_{birth} the value at which a cluster is opened. If the sum of the children clusters now has a larger value than the parent cluster, the children clusters are maintained as clusters. Vice versa, the children clusters would be merged into the parent cluster. For example, figure 4.2c shows cluster 1 and 2, where the decision was taken in favor of the children clusters.

The algorithm requires no global density threshold due to the individual selection of clusters to be considered. Indeed, in the example presented, a pure density-based approach would not have found this set of clusters where the event densities of cluster 1 and 2 are comparable but relatively dense with respect to cluster 3 (Figure 4.2a and d). However, HDBscan helps to extract clusters with different levels of densities. This is especially convenient as we expect different parts of the study area to be affected by varying degrees of seismicity in terms of spatiotemporal density.

HDBscan can be controlled by either just the introduced minimum cluster size hyper-parameter or an additional one. This additional hyper-parameter is called minimum samples and defines how conservative the clustering will be in determining outliers. In our study we tested a set of the two hyper-parameters to control the

stability of the clustering (Figure S1 in Supporting Information B). Figure S1 (in Supporting Information B) shows that minor details change as the hyper-parameters are altered, the most prominent bursts however remain unchanged. After testing, we set the minimum cluster size to a value of 60, which will require 60 seismic events within each burst in order to open a cluster. The minimum sample size is set to 60, representing a relatively conservative value within the tested range (Figure S1 in Supporting Information B).

Finally, we want to remind that the pipeline's principle follows a single-linkage approach similar to approaches which were already used for clustering in seismology (Zaliapin and Ben-Zion, 2013a; Zaliapin and Ben-Zion, 2013b; Davis and Frohlich, 1991).

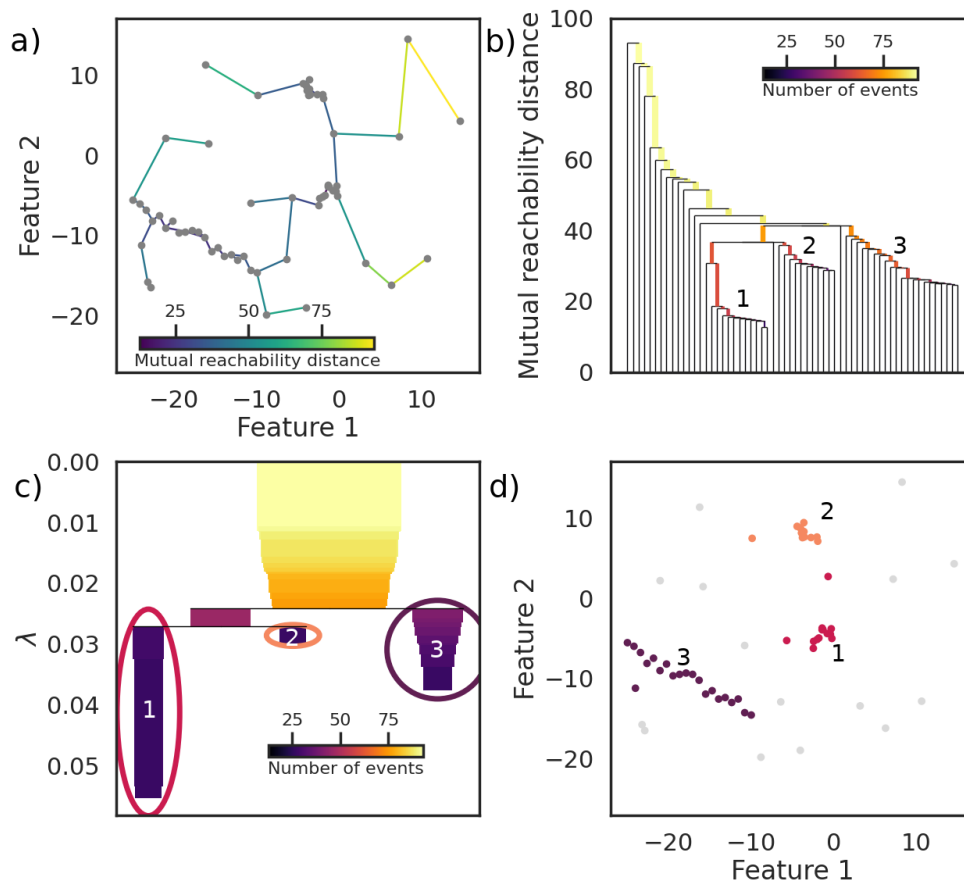


FIGURE 4.2: Conceptual pipeline of HDBscan. (a) 2-dimensional feature space of a set of synthetic example events (grey dots). The network of colored lines represents the minimum spanning tree (MST), where a single line connects the two closest events according to the mutual reachability distance. In the upper right part one can see that events are connected, even though their distance seems larger compared to other points in closer vicinity. This is happening in sparse area and is the imprint of the feature space transformation. (b) Hierarchical tree, indicating the mutual reachability distances from the MST. Numbers indicate the networks, which are finally considered as clusters. (c) Condensed hierarchical tree. Color-coded ellipses and numbers indicate the event networks which are finally considered as clusters. (d) The 2-dimensional feature space as indicated in (a), colored events indicate their affiliation to a certain cluster (indicated by numbers) as seen in (c)

4.3.2 Feature Preparation

The previously described clustering approach will be used to find subgroups of earthquakes depending on their individual spatial and temporal features. The features (latitude, longitude, depth, and origin time) will be extracted from a catalog that spans a period from July 2012 until the end of 2015, contains $\sim 400,000$ events, and is complete until a magnitude of completeness (M_c) ~ -0.7 (Essing and Poli, 2022).

As single linkage clustering techniques (such as the one previously described) may be influenced by an incomplete catalog in terms of magnitude (Frohlich and Davis, 1990), we only consider events above the M_c of -0.7 (Essing and Poli, 2022; Herrmann and Marzocchi, 2021). This step limits the number of events to consider for clustering to 97,120.

The input catalog is not relocated, meaning that new detections are associated to the position of the templates detecting them (Essing and Poli, 2022). As a result, many pairwise distances will be equal to zero, limiting the use of spatial clustering. For every new detection we therefore assign a distance from its template (Figure S2; Figure S3 in Supporting Information B), which is derived by a gamma distribution representative of the distance of redundant detection described in (Essing and Poli, 2022). We tested the influence of slightly varying distributions and found only marginal changes in the results of the clustering approach (Tab. S1 in Supporting Information B).

For the final clustering, we extract the four event features from the catalog and further combine them to a single pairwise distance matrix d_s .

Therefore, we first prepare the spatial features by applying a homogenization as the horizontal extension within the study area is significantly larger than the vertical extension (Piegari, Hermann, and Marzocchi, 2022). We transform each horizontal feature (max_{old}, min_{old}) to km and rescale it (x_{new}) with respect to the maximum vertical depth, following Piegari, Hermann, and Marzocchi (2022):

$$x_{new} = \frac{(max_{new} - min_{new})}{(max_{old} - min_{old})} \cdot (x_{old} - min_{old}) + min_{new} \quad (4.2)$$

where, min_{old} is the smallest horizontal, and max_{old} the largest horizontal component before spatial homogenization. min_{new} is set to 0 and max_{new} is set to the deepest event depth within the study area. We tested the presented approach with and without spatial homogenization. In general, the outcome without the application of spatial homogenization is similar over all presented results (Tab. S1 in Supporting Information B). However, the area as well as the dip angles of the resulting bursts without spatial homogenization are found to be more scattered and relatively smaller respectively (Figure S4 in Supporting Information B).

From the homogenized spatial features, we compute a pairwise distance matrix d of the hypocenter distances between all events. From the origin times of the events, we further compute the pairwise interevent-times in seconds resulting in matrix τ .

To combine the two matrices d and τ we follow the approach of Davis and Frohlich (1991) by using

$$d_{st} = \sqrt{d^2 + C^2 \cdot \tau^2} \quad (4.3)$$

Here, the C-parameter is used as a scaling constant that relates the pairwise interevent times to the pairwise interevent distances. The C-parameter must be adjusted based on the seismic activity of the study area (Davis and Frohlich, 1991;

Frohlich and Davis, 1990).

A large C -parameter emphasizes the time features, while a small C -parameter emphasizes the spatial features (Davis and Frohlich, 1991; Frohlich and Davis, 1990). In order to cluster aftershock sequences of synthetic and real earthquake catalogs, this approach has already been used with $C = 1$ (Davis and Frohlich, 1991; Frohlich and Davis, 1990). Compared to the studies cited above, here we focus on a relatively small study area with less influence of MS-AS sequences. Therefore, a value of $C = 1$ does not produce satisfactory clustering results, as illustrated in figure S5a (in Supporting Information B).

To define an appropriate C -parameter, we calculate the ratio between the largest hypo-central distance (after homogenization) and the largest interevent time. This yields a parameter of $C = 0.018$.

To test how this choice affects the final results, we further evaluate the clustering results for different values of C (Figure S5 in Supporting Information B). For $C > 0.1$, stripes along the spatial domain are observed indicating a strong influence of the temporal features for clustering. On the other hand, $C < 0.01$ produces elongated clusters in time, highlighting the spatiotemporal evolution of the swarm as a large, long lasting single cluster, lacking a detailed time evolution. As we are interested in a satisfactory spatial and temporal resolution in our work, C -parameters $0.1 > C > 0.001$ appear suitable. The following results are obtained using $C = 0.018$, thus the ratio between the largest hypo-central distance and the largest interevent time.

4.4 Results

In the following section, we first discuss the performance of the presented clustering approach and compare the clustered with the un-clustered seismicity. We then focus on the clustered seismicity and quantitatively analyze the extracted groups of events to derive insights about the physical driving mechanisms.

4.4.1 Separating Clustered Seismicity from the Background

With the introduced clustering approach, we are able to separate the seismicity of the initial catalog (Figure 4.3a), into un-clustered, and clustered seismicity (Figure 4.3b). The clustered seismicity makes up 38% of the events in the initial catalog and includes the majority of the largest events within the sequence (Figure 4.3c). By transforming the magnitude following Kanamori (1977) with $M_0 = 10^{1.5 \cdot M + 9.1}$, we estimate the cumulative seismic moment of the clustered seismicity $\sim 2 \cdot 10^{15}$ Nm to be larger than the cumulative seismic moment of the un-clustered seismicity ($\sim 1.8 \cdot 10^{15}$ Nm).

To evaluate the performance of the presented clustering approach we first assess the capability of discerning background and clustered events (e.g., Zaliapin et al., 2008; Zaliapin and Ben-Zion, 2013a; Zaliapin and Ben-Zion, 2013b). For the input catalog and the two resulting types of seismicity, the temporal evolution is shown in figure 4.3a and b. For the un-clustered seismicity, figure 4.3b shows a smooth evolution of the seismicity in time which significantly increases during the 2014 swarm (Gualandi et al., 2017), revealing that aseismic slip significantly affects the background rate of seismicity as suggested by other studies (Reverso, Marsan, and Helmstetter, 2015). The clustered seismicity on the other hand reveals a less smooth time evolution, intermittent by several localized accelerations in time indicative of temporal interaction (Figure 4.3b). This rapid acceleration of seismicity in time also

appears in the space-time domain (Figure 4.3b). Here, we note that the spatial proximity of events in each burst is indicative of spatial interaction. Thus, final spatiotemporal clusters for the chosen C-parameter reveal localized groups of events (Figure 4.3b), some of which are known sequences occurring in the study area like the Citta di Castello and two sequences along the Pietralunga fault (Figure 4.3a and b; Valoroso et al., 2017).

To further quantify the quality of our results, we calculate the rescaled spatiotemporal distances following the approach of Zaliapin and Ben-Zion (2013a) and Zaliapin and Ben-Zion (2013b). In agreement with Zaliapin and Ben-Zion (2013a) and Zaliapin and Ben-Zion (2013b) the background seismicity is characterized by an increased distance (Figure 4.3d) with respect to the clustered seismicity (Figure 4.3e). Thus, without the consideration of the magnitude for the distance metric and without imposing a global threshold, the two populations are well separated.

After the quantification of the quality of the separation between background and clustered seismicity we will now focus on the main goal of this work and analyze the found groups of seismicity within the clustered seismicity. Because these events mostly exhibit burst-like characteristics, we shall now refer to them as bursts.

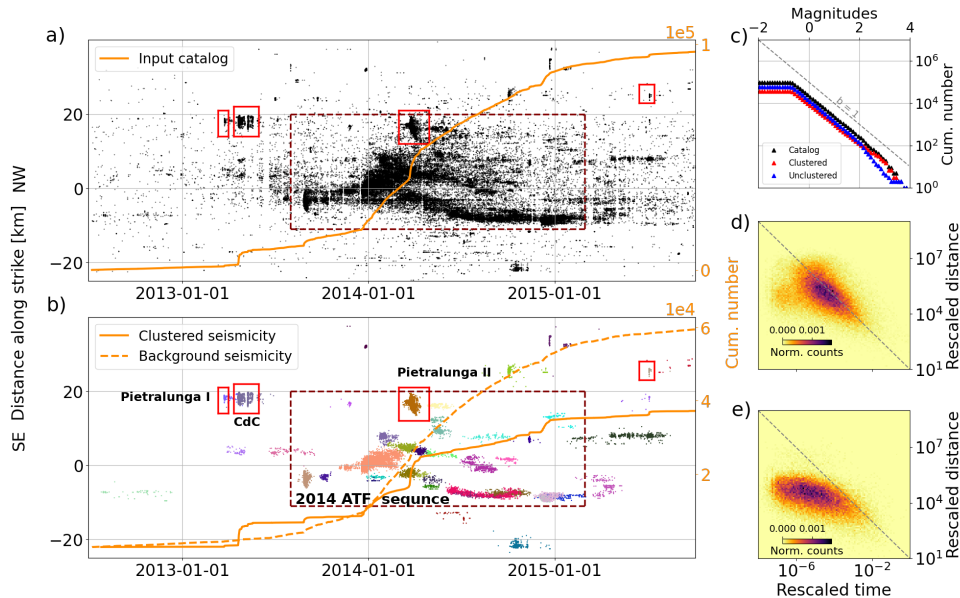


FIGURE 4.3: (a) Space-time evolution of the input catalog, (b) clustered seismicity. For the clustered seismicity, extracted bursts are indicated with different colors. Well known sequences like the Citta di Castello (CdC), the Pietralunga I, II, as well as the isolated sequence are marked by a red frame (Figure 4.1). The 2014 ATF swarm sequence is marked with a dashed maroon frame. (c) Frequency magnitude distribution of the input catalog, un-clustered, and clustered seismicity. The dashed diagonal line indicates the b-value of the initial catalog (Valoroso et al., 2017). (d) Joint distribution of the rescaled time T_{ij} and space distances R_{ij} for the un-clustered seismicity. (e) as (d) but for the clustered seismicity. For reasons of comparison, we indicated a diagonal dashed line.

4.4.2 Size and Duration of Seismic Bursts

The resulting clustered seismicity makes up 38% of the initial catalog and can be separated into 44 bursts (Tab. S1 in Supporting Information B), mainly consisting of

hundreds up to several hundred events (Figure 4.4a). After the visualization of the horizontal spatiotemporal evolution (Figure 4.4b), we now visualize the location of each burst along depth (Figure 4.4a). The majority of bursts are found in shallow depths between 1 and 6 km, overlapping the depth of the clustered seismicity found by Essing and Poli (2022) as well as the depth range of the aseismic deformation signal reported by (Gualandi et al., 2017).

In figure 4.4a we further report the cumulative seismic moment of each burst. The histogram shows a continuous spectrum with the majority of bursts radiating relatively small amounts of seismic moment and a smaller number of bursts with a large seismic moment release. Interestingly, the decrease of the number of bursts as a function of seismic moment weakly follows the b-value of the study area (Valoroso et al., 2017).

The duration of each burst as the time between the first and last event is reported in figure 4.4b. A continuous spectrum of duration's ranging from ~ 20 up to ~ 200 days can be seen.

By identifying the region enclosing the seismic events in each burst, we estimate the area (A) occupied by each burst (Figure 4.4b). Therefore, we estimate the occupied horizontal area using a convex hull approach (Fischer and Hainzl, 2017; Cabrera, Poli, and Frank, 2022).

We additionally consider the three-dimensional distribution of seismicity. We therefore find the best fitting plane from the eigenvectors (Zhang and Shearer, 2016). From the two eigenvectors with the largest eigenvalues, we estimate the strike (Figure 4.1a, inset) and the dip angle (Figure S6 in Supporting Information B). While the estimated dip angles seem systematically smaller than expected for the study area (Mirabella et al., 2011), the strike angles fit well the NW trending overall tectonics. We project the seismicity of each burst along its strike and dip angle to finally estimate the occupied area using the same convex hull approach as previously indicated (Figure S7 in Supporting Information B).

The results from both approaches (Figure 4.4b; Figure S7 in Supporting Information B) are comparable and reveal that the majority of clusters range in size from about 0.5 to 100km^2 .

The comparison of the estimated area (A) and duration (T) of the bursts reveals a direct proportionality in the log-log space, which can be expressed by $T \propto A^{1.0}$. The relationship suggests that the size of the clusters is directly proportional to their duration. The scatter in figure 4.4b can be attributed to either erroneous estimation of A and/or T , by the existence of multiple velocities in a burst (Dublanche and De Barros, 2021) or heterogeneous propagation of the seismicity (Dublanche and De Barros, 2021).

We also assess how A and T of each burst scale with the cumulative seismic moment estimated from the earthquakes in each burst (Passarelli et al., 2018; Fischer and Hainzl, 2017; Cabrera, Poli, and Frank, 2022). The comparison between A and seismic moment (M_0) is expressed by equation $M_0 \sim A^{4.1}$ and shows a weak scaling for the studied swarms (Figure S8a in Supporting Information B).

Assuming a circular area for each cluster we can transform A to the radius r and relate it to the cumulative seismic moment using the effective stress drop $\Delta\sigma_{eff} = 7M_0/16r^3$ (Fischer and Hainzl, 2017). Reference values of constant $\Delta\sigma_{eff}$ are reported in Figure S8a in Supporting Information B and exhibit generally low effective stress drops (< 0.01 MPa) for all the studied bursts, similar to previous studies (Fischer and Hainzl, 2017; Passarelli et al., 2018; Roland and McGuire, 2009).

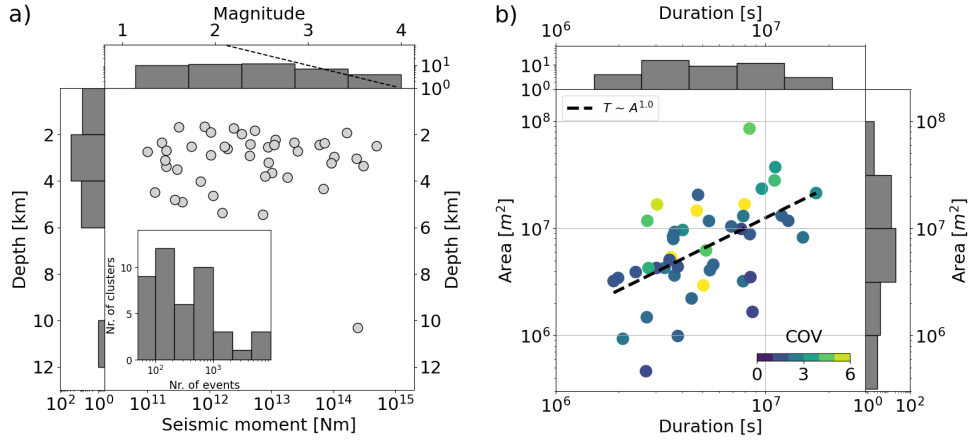


FIGURE 4.4: (a) The cumulative seismic moment/magnitude as a function of average depth for each burst. The upper histogram shows the distribution of the summed magnitudes of the bursts and a b-value of 1 (Valoroso et al., 2017) indicated as a dashed line. The inset shows the distribution of the number of events within the bursts. The left histogram shows the number of clusters along depth. (b) Duration as a function of horizontal area for each burst, with the color-code indicating the coefficient of variation of the interevent times (COV). Dashed line indicates the least squares fit. Histograms of the duration and the area of seismicity within the obtained bursts are indicated in the upper and right panel respectively.

We additionally observe a weak scaling between T and M_0 (Figure 4.5b), in agreement with previous studies, in different tectonic regions (Passarelli et al., 2021; Peng et al., 2021).

The general lack of scaling reported in figure S8 (in Supporting Information B) agrees with observations for other seismogenic swarms (Gao, Schmidt, and Weldon, 2012; Ide et al., 2007; Passarelli et al., 2018) while it significantly differs from scaling of slow slip events (Aiken and Obara, 2021; Frank et al., 2016; Tan and Marsan, 2020) and regular earthquakes (Wells and Coppersmith, 1994).

The lack of scaling could be related to fact, that in this approach we only account for the radiated seismic moment, without however compensating for aseismic moment release. We therefore follow Danré et al. (2022) by assuming that the slip released seismically over seismic asperities is similar to the surrounding aseismic slip. Similar to Danré et al. (2022), we further assume that asperities only rupture once and that the largest rupture provides a first order approximation of the slip over the whole area. To estimate the slip we make use

$$D_{max} = M_{0,max}^{\frac{1}{3}} \frac{(16\Delta\sigma_{max})^{2/3}}{7G\pi^{2/3}} \quad (4.4)$$

where the G is the shear modulus (30 GPa) and $\Delta\sigma$ the stress drop (3 MPa). The total moment over the seismic area can now be approximated by assuming that the aseismic moment is released between and the seismic moment along asperities. We therefore follow (Danré et al., 2022) with

$$M_{0,total} = GD_{max}A \quad (4.5)$$

This is done for every extracted burst as seen in figure 4.5. In figure 4.5a one can now see the comparison between A and the total moment which exhibits scaling that

can be expressed by equation $M_0 \sim A^{2.2}$ for the studied swarms. However, the comparison between the duration T and the total moment does only exhibit extremely weak scaling (Figure 4.5b).

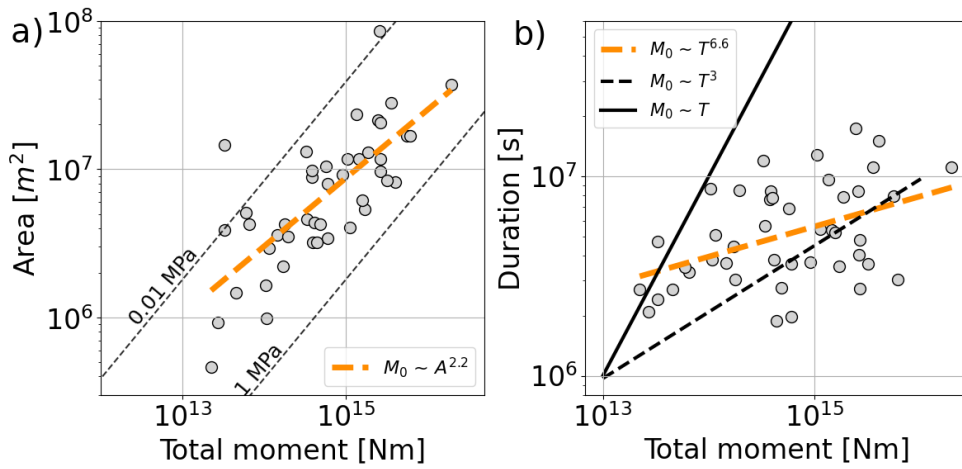


FIGURE 4.5: Scaling properties of the extracted bursts. (a) Area of seismicity (A) as a function of the total moment. Contours indicate the effective stress drop $\Delta\sigma_{eff}$. (b) As (a) but for the duration (D).

4.4.3 Time Evolution of the Seismic Moment and Triggering of Seismicity

For each burst we further quantify the temporal evolution of the seismic moment and analyze the temporal dynamics which highlight the interaction between events (Beuc e, Hilst, and Campillo, 2022; Cabrera, Poli, and Frank, 2022; Essing and Poli, 2022; Poli et al., 2022).

We analyze the seismic moment release for the extracted seismic bursts in order to reveal insights about the driving mechanism (Figure 4.6). If a seismic burst is triggered by a large earthquake via static or dynamic stress transfer (Freed, 2005), the largest event, the mainshock, must occur at the beginning of each cluster. We thus normalize the position of the largest event by the total number of events in each burst (Elst et al., 2016). Small values indicate an early, while large values indicate a late occurrence of the event with the largest magnitude. Figure 4.6a shows that for a large group of bursts, the largest magnitude event occurs relatively early in the sequence.

For each burst we study the seismic moment release over time, by calculating its skewness (Roland and McGuire, 2009; Chen and Shearer, 2011). If the seismic moment is released symmetrically over time, the skewness should be near to zero. Negative values indicate a sequence that begins slowly with an abrupt end, whereas positive values indicate an abrupt beginning and a slow fading, as expected for MS-AS sequences (Chen and Shearer, 2011; Roland and McGuire, 2009). In figure 4.6b the resulting skewness values indicate mostly negative or small positive values (< 5), indicating a symmetric release of seismic moment over time.

We assess the difference in magnitude between the largest event and the second largest event within each burst (B ath, 1965). For various tectonic environments, it has been empirically demonstrated that the second largest event of a MS-AS sequence is 1 to 1.4 magnitude units smaller than the mainshock (Felzer et al., 2002). Swarms on the other hand have been characterized as having only minor magnitude differences among their events (Mogi, 1963; Vidale and Shearer, 2006). Figure

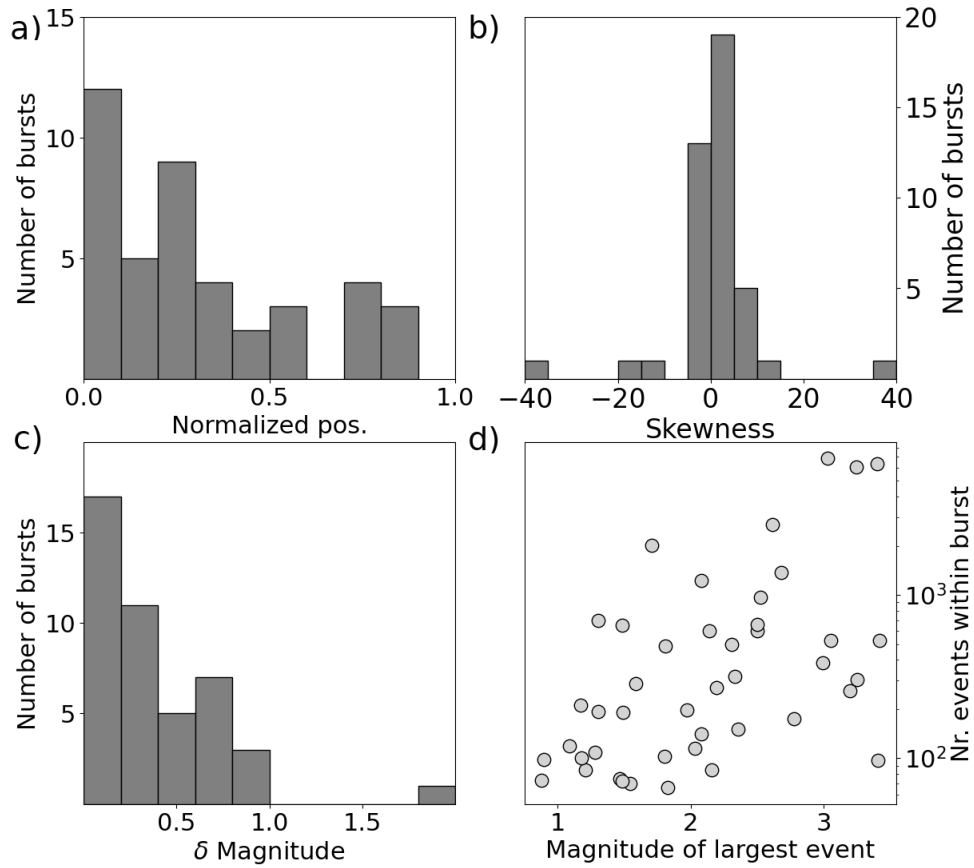


FIGURE 4.6: Histograms showing the distribution of bursts with (a) normalized position of the largest event within a burst, (b) skewness of the seismic moment within each burst, and (c) Δ magnitude between the largest and the second largest event within a burst. (d) Total number of events as a function of the magnitude of the largest event for each burst.

4.6c therefore reports the difference in magnitude between the largest and second largest event within each burst. It can be seen that a majority of bursts exhibit small differences in magnitudes ($< \Delta 1$), with only 1 burst showing a difference $> \Delta 1$.

Within MS-AS sequences the number of events following a mainshock should be proportional to its magnitude (Vidale and Shearer, 2006; Vidale, Boyle, and Shearer, 2006). Therefore, figure 4.6d compares the number of events within each burst with its largest magnitude. Overall, one can see the number of events uncorrelated to the magnitude of the largest event, indicating the independence of the two parameters (Vidale and Shearer, 2006; Vidale, Boyle, and Shearer, 2006). This gives evidence that for most of the bursts the driving mechanism is not related to co-seismic processes.

Furthermore, figure 4.6d shows an unusually high number of events inside bursts, which is difficult to reconcile with aftershock seismicity only (Boettcher and Jordan, 2004; McGuire, Boettcher, and Jordan, 2005; Passarelli et al., 2018).

To estimate the temporal interaction of events within each burst, we calculate the coefficient of variation (COV), that is the ratio between the standard deviation and the mean of the interevent times. The COV measures the temporal interaction of earthquakes (e.g., Cabrera, Poli, and Frank, 2022; Kagan and Jackson, 1991; Sánchez-Reyes et al., 2020; Schoenball and Ellsworth, 2017; Poli et al., 2022), with values of 0 for events occurring with a constant interevent time, 1 for events with random interevent times, and greater than 1 for interaction between events.

The analysis of the COV reveals that the majority of the bursts exhibit values between 1 and 3, indicating slightly increased time interaction between earthquakes (Fig 4.4b), while four bursts exhibit rather large values ($COV > 6$) indicative for increased temporal interaction.

We then analyze the temporal evolution of the extracted bursts. The decay of the event rate immediately following the largest event is a common feature of MS-AS sequences where a power-law decay is used to describe it empirically (Omori, 1894; Utsu, Ogata, et al., 1995). Additionally, an inverse behavior was reported for events preceding larger events (Ogata, Utsu, and Katsura, 1995). Following Schoenball and Ellsworth (2017), we divide each burst into events occurring before and after the largest event. We count the daily event number approaching/moving away from the largest event. The stacked daily event count time series are reported in figure 4.7. Figure 4.7a shows an inverse Omori law for the time preceding the largest event, with an increase in seismicity rate beginning days to months before the largest event.

Figure 4.7b shows the stacked event rate for seismicity occurring after the largest event and further reveals a decay similar to the empirical Omori law, a prominent feature of MS-AS sequences (Schoenball and Ellsworth, 2017), which was also found for the ensemble of seismicity related to the 2014 ATF swarm sequence (Essing and Poli, 2022; Valoroso et al., 2017).

Comparing the two stacked event count time series reveals a symmetry, indicative of a similar number of seismicity radiated before and after the largest event, contrary to what is reported for pure MS-AS sequences (Shearer, 2012). The symmetric behavior is further consistent with the skewness reported in figure 4.6b and indicative of a swarm type sequence with an increased aseismic component (McGuire, Boettcher, and Jordan, 2005).

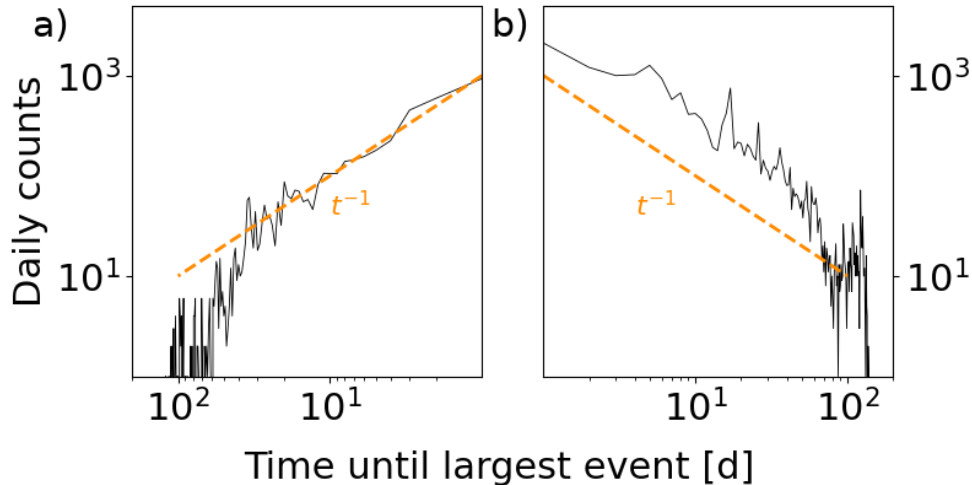


FIGURE 4.7: Stack of the daily event count time series over all bursts considering events (a) preceding the largest event and (b) following the largest event within a burst. The increase/decrease of the seismicity rate following the empirical Omori-law is indicated by orange dashed lines.

4.5 Discussion

Applying unsupervised clustering to spatial and temporal features of earthquakes permitted to automatically extract clusters of seismicity from a high-resolution earthquake catalog (Figure 4.1; Figure 4.3). Therefore, the presented clustering approach relaxes the space-time-magnitude metric using only spatiotemporal features of the seismicity (Reasenber, 1985; Zaliapin et al., 2008; Zhang and Shearer, 2016) which is in a sense similar to previous approaches (Frohlich and Davis, 1990; Zhang and Shearer, 2016). The approach is capable of subdividing the clustered seismicity into individual bursts while it accounts for the issue of a variable background rate in a given location. The approach may be expanded to examine bursts of seismicity in different regions with variable densities of seismicity in order to detect bursts of seismicity. In summary, this approach can complement the actual methodologies to detect seismic swarms in different tectonic regions (Reverso, Marsan, and Helmstetter, 2015; Zhang and Shearer, 2016).

As clustering approaches generally do provide non-unique results which are sensitive to the set of hyper-parameters, we study their influence prior to its final application (Figure S1; Figure S4; Figure S5 in Supporting Information B). We further ensure that a variation of the hyper-parameters does not affect the quantities that we finally used to infer the physical properties of each burst (Figure S1 in Supporting Information B).

The results for the preferred hyper-parameters highlighted two main groups of earthquakes, clustered ones, which account for 38% of the catalogued events, and the un-clustered background seismicity (Figure 4.3). The background seismicity exhibits weak temporal interaction (Figure 4.3b), even though, during the 2014 ATF swarm sequence, the event rate smoothly rises (Figure 4.3b), which could be due to an increased loading rate (Gualandi et al., 2017), that would increase smoothly the seismicity rate without however showing strong interaction in between events (Reverso, Marsan, and Helmstetter, 2015). The background seismicity further exhibits relatively large, rescaled space and time distances (Figure 4.3e), indicating a mainly

un-clustered character as reported for background seismicity (Zaliapin et al., 2008; Zaliapin and Ben-Zion, 2013a; Zaliapin and Ben-Zion, 2013b).

The clustered seismicity is composed of 44 bursts, each of which was carefully analyzed to infer their driving mechanisms (Figure 4.4; Figure 4.5; Figure 4.6). For the majority of the bursts we found symmetries in the seismic moment release (Figure 4.6b), as well as in the time evolution of the event numbers (Figure 4.7), suggesting that bursts are mostly swarm like sequences (Chen and Shearer, 2011; Roland and McGuire, 2009; Schoenball and Ellsworth, 2017).

On the other hand, we observe that for a large number of bursts the largest event in terms of magnitude is released relatively early, which could indicate a MS-AS sequence (Figure 4.6a). At first place, this is difficult to reconcile with the symmetric seismic energy release reported in figure 4.6b (Roland and McGuire, 2009; Chen and Shearer, 2011). However, it is important to note that the difference in magnitude between the largest and the second largest event within each burst tends to be small (Fig 4.6c), contrary to what is reported for MS-AS (Båth, 1965).

We found the extracted bursts mainly within the HW, during a time period of increased seismicity (Essing and Poli, 2022), and overlapping in time and space with an aseismic deformation signal (Gualandi et al., 2017). These bursts are characterized by temporal interaction, with a COV of the interevent times which exhibits mainly values between 1 and 3 (Fig 4.4b), in agreement with previous studies (Essing and Poli, 2022). Furthermore, the resulting effective stress-drop of each burst exhibit values below 0.1 MPa (Figure S8a in Supporting Information B), indicative of a low density of seismic events with respect to the area covered by the seismicity (Cabrera, Poli, and Frank, 2022; Fischer and Hainzl, 2017; Roland and McGuire, 2009).

The ensemble of our observations indicate that the bursts are mainly related to a spatial and temporal increment of seismicity, not driven by the occurrence of a mainshock, which leads us to define them as swarm-like sequences (Chen and Shearer, 2011). The estimated parameters can then help to discuss some possible mechanism(s) driving the occurrence of the bursts.

The swarm-like time evolution (Figure 4.6b; Fig 4.7), the large aseismic contribution (Figure 4.5) and the low stress drops (Figure S8a in Supporting Information B) agree with either aseismic slip (Cappa, Rutqvist, and Yamamoto, 2009; Gualandi et al., 2017; Guglielmi et al., 2015; Lohman and McGuire, 2007) or fluid migration (Hainzl, 2004; Shapiro, Huenges, and Borm, 1997). Despite the presence of fluids in the region is well documented (Piana Agostinetti, Giacomuzzi, and Chiarabba, 2017), the relatively strong temporal interaction (Figure 4.4b) seems to favor aseismic slip as driver for each burst. Indeed, injection of fluids from depth (Piana Agostinetti, Giacomuzzi, and Chiarabba, 2017) would increase the seismicity rate, but without the substantial temporal clustering exhibited by the studied bursts (Figure 4.4b, Beaucé, Hilst, and Campillo, 2022). Furthermore, events driven by the injection of fluids would migrate in a diffusive way (Shapiro, Huenges, and Borm, 1997) for which no evidence was found within the presented study. However, it is important to mention that our conclusions do not rule out the role of fluids (Piana Agostinetti, Giacomuzzi, and Chiarabba, 2017), which are known to play an essential role in pushing the fault zone into the physical state in which it could develop aseismic slip (Danré et al., 2022; De Barros et al., 2021; Guglielmi et al., 2015).

In summary, we propose that the 2014 overall aseismic deformation episode occurring in the shallow fault system of the ATF (Gualandi et al., 2017), is composed of several smaller episodes of aseismic slip pulses, represented by the bursts we identified. The bursts are a byproduct of the aseismic slip (Essing and Poli, 2022) and can

be indirectly linked to pore pressure diffusion (Danré et al., 2022; De Barros et al., 2021). This burst like behavior is similar to the one observed for tremors and low frequency earthquakes occurring during slow slip episodes in subduction zones (Frank et al., 2016; Tan and Marsan, 2020).

The overall ensemble of the 2014 ATF swarm sequence consists of a complex interplay of various small-scale (space and time) aseismic transients, organized in a complex cascading process (Frank et al., 2016). The behavior observed inside each is possibly resulting from the complex stress interaction between aseismic slip and earthquakes, in agreement with numerical models in complex fault systems (Catania and Segall, 2021; Dublanchet, Bernard, and Favreau, 2013), as the highly fractured shallow HW of the ATF (Piana Agostinetti, Giacomuzzi, and Chiarabba, 2017).

Finally, it is important to discuss that despite the resemblance of the identified burst with LFE and tremors (Frank et al., 2016; Tan and Marsan, 2020), we observe no scaling of the duration of the bursts with their cumulative seismic moment (Figure S8b in Supporting Information B). The lack of scaling itself is not surprising, as it was observed in several previous studies (Passarelli et al., 2018; Passarelli et al., 2021; Peng et al., 2021). This lack of scaling is suggested to be related with a typical time scale of the swarm evolution, controlled by the rheological properties of a fault, which changes from region to region (Peng et al., 2021). The lack of scaling we observe between the area and the cumulative seismic moment (Figure S8a in Supporting Information B) can be attributed to an underestimation of the cumulative total moment for the bursts (Figure 4.5a), which can be compensated by accounting for the aseismic strain release associated with each burst (Danré et al., 2022; Passarelli et al., 2018). This second hypothesis is supported by recent results from Passarelli et al. (2021), which revealed that seismic moment typically is significantly lower with respect to the aseismic moment during swarms and slow slip episodes. Further evidence for this hypothesis is provided by the observation of the amount of geodetic moment which is twice the observed seismic moment within the study area (Gualandi et al., 2017). However, more research with quantitative comparisons of seismic and geodetic data will be needed to understand what controls the observed lack of scaling (Figure S8 in Supporting Information B).

4.6 Conclusion

We here presented and tested an approach that first separates background from clustered seismicity and is further able to extract groups of clustered seismicity in an automated and data-driven fashion. The presented method is in a sense related to a already existing methods (Zaliapin et al., 2008; Zaliapin and Ben-Zion, 2013a; Zaliapin and Ben-Zion, 2013b). However, the advantage of the presented approach is that it accounts for a non-stationary background seismicity rate and is able to subdivide the clustered seismicity into seismic bursts of different behavior.

The detailed analysis of the clustered seismicity indicates that a large portion of small-scale seismic bursts can be related to aseismic processes which adds evidence to recent findings within the study area (Essing and Poli, 2022; Gualandi et al., 2017).

It further exhibits that the complexity of the 2014 ATF swarm sequence could probably arise from the ensemble of various small-scale aseismic transient events interacting within a cascade-framework.

Chapter 5

Fast Reoccurring, Repeating Earthquakes as a possible Indication for Fluid over-pressure¹

Abstract

The Alto Tiberina Fault system, located in the Northern Apennines (Italy), consists of a low-angle normal fault that is assumed to host aseismic creep. The presence of repeating earthquakes (REs) was utilized as evidence for this creep-model, among other indications. In this work we reassess the seismicity along the low-angle normal fault in terms of source parameters and high-resolution locations in order to obtain detailed insights about the occurrence of REs. The found families of REs systematically exhibit short time intervals between consecutive REs, which makes them difficult to reconcile with creep as a loading mechanism. Thus, we present an alternative model based on fluid overpressure that we consider more reasonable in explaining the short time intervals between REs.

¹In preparation for submission in Geophysical Research Letters. Essing, D., & Poli, P. (2023). Fast reoccurring, repeating earthquakes as a possible indication for fluid over-pressure.

5.1 Introduction

Low-angle normal faults (LANF) are intriguing geological formations seen in extensional tectonic regimes, where they are considered to be important structures for accommodating and releasing accumulated strain (Wernicke, 1995). Those structures are normal faults with a dip angle lower than 30° , which should – following the well accepted Anderson-Byerlee rupture theory (Byerlee, 1978) - allow frictional fault reactivation only under peculiar circumstances (Collettini, 2011).

Nevertheless, seismically active LANFs have been discovered in a number of locations around the world (Abers, Mutter, and Fang, 1997; Biemiller et al., 2020; Chiaraluce et al., 2007; Rietbrock et al., 1996). This raises questions about the driving mechanism and whether these faults are capable of producing moderate-to-large magnitude earthquakes, or if other deformation mechanisms facilitate the accommodation of the extension (e.g., Collettini, 2011; Wernicke, 1995).

A well-studied LANF is the Alto Tiberina Fault (ATF) located in the Apennines (Figure 5.1a). The ATF is thought to accommodate large portions of the overall tectonic extension of ~ 2 mm/yr within the region (Serpelloni et al., 2005). The structure of this fault is well characterized by several studies (Barchi et al., 2003; Mirabella et al., 2004; Piana Agostinetti, Giacomuzzi, and Chiarabba, 2017; Collettini and Barchi, 2002, among others), that reveal a NNW trending major fault dipping $15^\circ - 20^\circ$ from the surface to at least 12 – 14 km depth. At depths below 4 km the fault plane is highlighted by constant micro-seismicity within a 500 – 1,500 m thick fault zone (Chiaraluce et al., 2007).

There is continuing debate regarding the way extension is accommodated within this region (Anderlini, Serpelloni, and Belardinelli, 2016; Essing and Poli, 2022; Gualandi et al., 2017; Vuan et al., 2020), which is directly related to the question whether or not, the surface of the ATF creeps aseismically. Evidence for aseismic creep was obtained from inversions of data recorded at a network of GNSS stations and a block-modeling approach (Anderlini, Serpelloni, and Belardinelli, 2016). Anderlini, Serpelloni, and Belardinelli (2016) further used repeating earthquakes (REs) as evidence for the creep-model. In this model REs are thought to occur on seismically active (rate-weakening) fault patches frequently loaded by surrounding constant creep (rate-strengthening) along the LANF (Nadeau and Johnson, 1998; Uchida, 2019).

In this work we systematically reassess earthquakes within the study area using a high-resolution earthquake catalog with a magnitude of completeness of $M_L \sim -0.6$ (Essing and Poli, 2022), to extract REs. Potential REs are re-located and merged into event families. For each RE we then refine the source parameters. Families exhibit extremely short time intervals between consecutive REs ($1 \cdot 10^2 - 1 \cdot 10^5$ s), which is difficult to reconcile with creep along the LANF surface as a driving mechanism loading seismically active patches until failure.

As the study area shows an abundance of fluids (Chiodini et al., 2000) and pore-fluid overpressure (Chiodini and Cioni, 1989), we propose an alternative model derived from fluid injection environments (Baisch and Harjes, 2003).

5.2 Identification of Repeating Earthquakes

For the following work we will make use of a template matching catalog (Essing and Poli, 2022) derived by an array of borehole seismic stations (Chiaraluce et al., 2014) within the study area (Figure 5.1, red triangles). The catalog covers a time

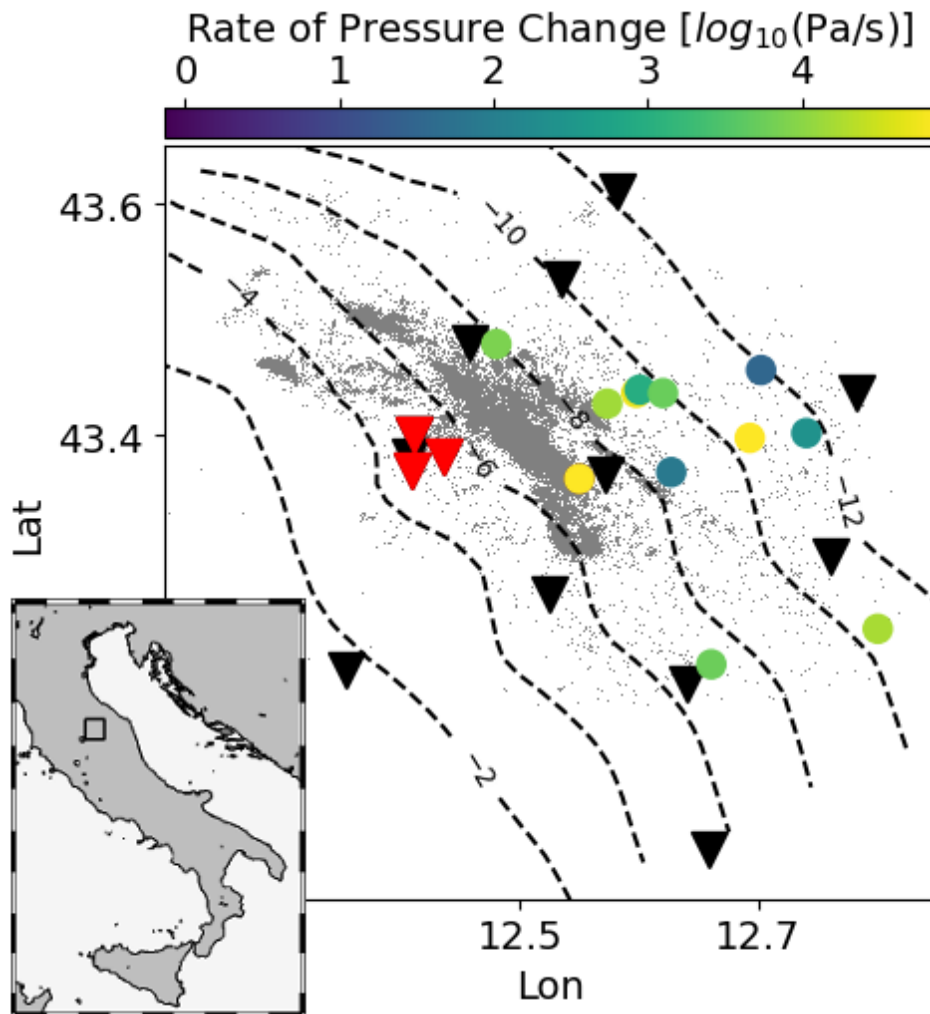


FIGURE 5.1: (a) Contour plot of the LANEF, where dashed lines indicate the depths, grey dots indicate the 2014 swarm sequence in the HW (Essing and Poli, 2022). Colored dots indicate the locations of repeating earthquakes and the rate of pressure change estimated following Baisch and Harjes (2003). Black triangles indicate surface seismometer, while red triangles indicate borehole seismometer which are all part of The Alto Tiberina Near Fault Observatory (Chiaraluca et al., 2014).

period from July 2012 to December 2015, which encompasses a transient aseismic deformation signal (Gualandi et al., 2017) overlapping with a major earthquake swarm (Essing and Poli, 2022; Valoroso et al., 2017), both of which mainly affecting high angle normal faults within the shallow part of the study area above 7 km depth. The catalog is complete until a magnitude of ~ -0.6 , however small magnitude events ($M < \sim 0$) are not relocated, but are associated with the location of the template that detected them (Essing and Poli, 2022).

We systematically examine the seismicity below 7 km depth for pairs of earthquakes with a high similarity value. We extract the waveforms (9.5 s window length, 500 Hz sampling rate, filtered between 1.5 to 15 Hz (Duverger et al., 2018; Schaff and Waldhauser, 2005)) on all 12 borehole seismometer components (Figure 5.1a, red triangles) beginning with the P-arrival and containing significant amounts of the S-coda. We further estimate the signal-to-noise ratio (SNR) for each detection within a 0.5 s window before the P-arrival. The waveforms are component-wise cross-correlated, while the maximum is extracted. This maximum is then averaged over all components, while values retrieved from low SNR components are down weighted using a logistic function (Duverger et al., 2018, Supporting Information A).

Next, we group events sharing a similarity value > 0.90 following a simple equivalence class approach. In comparison to (Essing and Poli, 2022), we apply a slightly less strict similarity value since we will relocate the events later in this study (Uchida, 2019). This initial selection gives 60 events divided into 26 event groups, the majority of which are doublets, with just 5 triplets and one group of four events.

We relocate the obtained initial selection of events, making use of an extended station network covering the whole study area (Figure 5.1a, all triangles). Surface stations within the study area (Figure 5.1a, black triangles) sample with 100 Hz. We therefore use two different sampling rates (100 and 500 Hz); however, the frequency band will be similar to the one used before (1.5-15 Hz). For each pair of events, we measure the pairwise differential times of the P and S-phases. Hence, we predict the arrival times at each station based on a 1D velocity model (Chiaraluce et al., 2007) and further extract the P and S-phases 0.1s before and 0.6s after the predicted phase arrival. From the pairwise waveforms of the phase arrivals, we build cross-correlation functions and extract the maximum as well as the temporal shift of the maximum.

The extracted maximum as well as the temporal shift of the maximum is then used to relocate these events. Here, we apply a relocation approach (Trugman and Shearer, 2017) to precisely estimate the hypo-central distance between consecutive events. Hereby, we only consider events with a maximum of 0.5 of the cross-correlation function.

The magnitudes of events within the initial catalog (Essing and Poli, 2022) are estimated by measuring the ratio of the waveform amplitudes between the template and the newly detected event, resulting in a local magnitude M_L (Cabrera, Poli, and Frank, 2022; Essing and Poli, 2022). To obtain precise estimates of the seismic moment (M_0) and the moment magnitude (M_w) of each event, we make use of the displacement spectra of the P-waves and fit it to the general model

$$\Omega(f) = \frac{\Omega_0 e^{-\frac{\pi f t}{Q}}}{(1 + (f/f_c)^{\gamma m})^\gamma} \quad (5.1)$$

Here, f is the frequency, Ω_0 is the low frequency amplitude, f_c is the corner frequency, t the travel time of the waveform type considered, Q a quality factor, n the

fall-off rate at high frequencies, and γ a constant. At the source ($t = 0$), with $n = 2$, and $\gamma = 1$, equation 5.1 turns into the spectral shape proposed by Brune (1970), while $\gamma = 2$ turns equation 5.1 into the spectral shape proposed by (Boatwright, 1980).

From Ω_0 , the seismic moment M_0 can be estimated following Brune (1970)

$$M_0 = \frac{4\pi\rho c^3 R \sqrt{\Omega_0^2}}{U_{\Phi\Theta}} \quad (5.2)$$

with the density $\rho = 2650 \text{ kg/m}^3$ (Collettini and Barchi, 2002), the P-wave velocity $c = 6.5 \text{ km/s}$ (Chiaraluce et al., 2007), the hypo-central distance from source to receiver R , and the mean radiation pattern $U_{\Phi\Theta} = 0.52$ (Abercrombie, 1995).

Again, we make use of the extended seismic network (Figure 5.1, all triangles). Displacement waveforms are downloaded for time windows starting 2 minutes before the P-wave arrival with a length of 5 minutes. The waveforms are bandpass filtered between 5 – 45 Hz and 5 – 225 Hz depending on the stations maximum sampling rate (100, 500 Hz) and further detrended. We then cut the waveforms into 2 s lasting time windows of noise (ending 1 s before the theoretical arrival time of the P-wave) and signal starting 1 s before the predicted P-wave arrival. We use a cosine taper to smooth the windows at the edges.

We measure the SNR of the signal by comparing the absolute maximum value of the P-wave window with the absolute maximum value of the corresponding noise window. We transform the time domain of the signal into the frequency domain (Figure 5.2b). We further apply Konno Ohmachi smoothing for the full frequency band (5 – 45, 5 – 225 Hz) and a bandwidth coefficient of 50.

The fit of Brunes- (Brune, 1970) and Boatwright-model (Boatwright, 1980) yields the low-frequency amplitude Ω_0 , which is transformed into the seismic moment M_0 following equation 5.2. This is done at all stations, however the final estimate of Ω_0 is only considering the average obtained from stations with a $\text{SNR} > 5$.

In a final step, we transform the seismic moment M_0 to a radius r by following Eshelby (1957)

$$\Delta\sigma = \frac{7M_0}{16r^3} \quad (5.3)$$

assuming stress drops $\Delta\sigma$ in a range of 1 – 30 MPa and combine the results with the relocation outcome to estimate the portion of overlap (Figure 5.2b). We define a pair of events as overlapping if the sum of the two estimated radii is two times larger than the interevent distance. This definition yields 13 overlapping event families that consist mainly of doublets and two triplets. Interestingly, the resulting families of REs mainly show short time intervals between consecutive events (Tab. S1; Figure S1 in Supporting Information C), which will be now further analyzed.

5.3 Estimation of Slip

REs are found in various tectonic environments (e.g., Ellsworth and Dietz, 1990; Vidale et al., 1994; Nadeau, Foxall, and McEvilly, 1995; Bürgmann et al., 2000; Igarashi, Matsuzawa, and Hasegawa, 2003; Uchida et al., 2003; Peng and Ben-Zion, 2005; Chen, Nadeau, and Rau, 2008). They are interpreted as repeated ruptures of the same asperity due to loading from aseismic creep on the surrounding fault surface (Uchida, 2019). Assuming this concept to be valid, the size of a RE as well the time

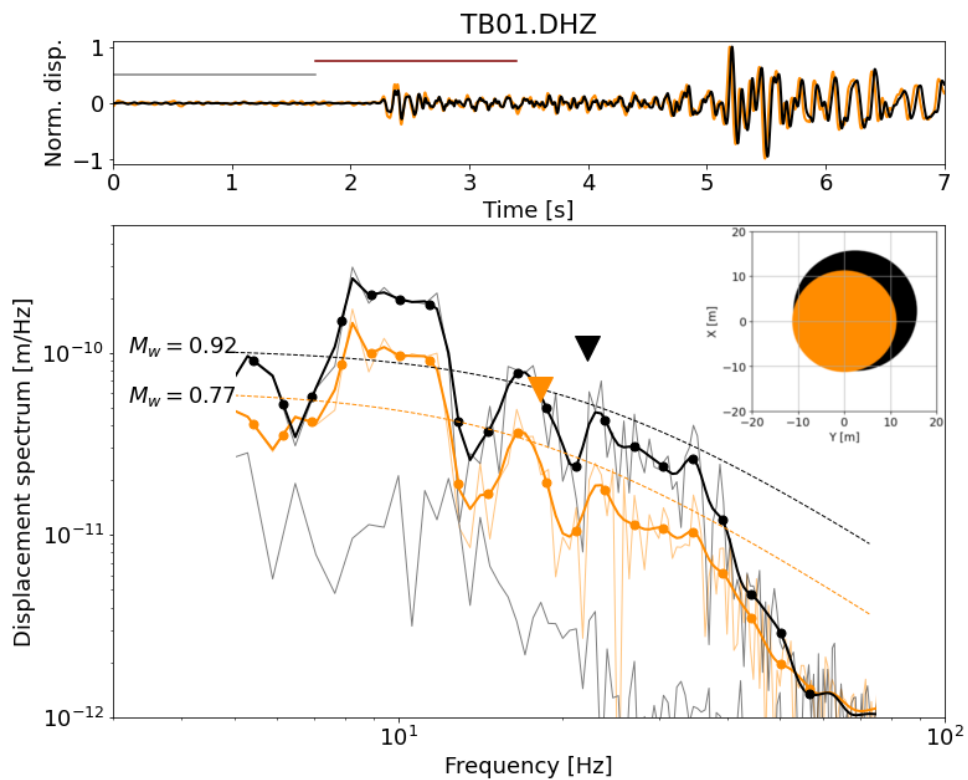


FIGURE 5.2: (a) Displacement waveforms of a pair of repeating events. Gray line indicates the noise window, while the maroon line indicates the signal window, both of which are transformed to the frequency domain. (b) Frequency domain of the two P-waves and the noise window of the first P-wave. Indicated in dashed lines is the fit of the Brune (1970) and the resulting moment magnitude (M_w). The inset shows the overlap between the two events.

interval between consecutive REs can be used to track the slip history of the surrounding creeping fault (Uchida, 2019).

REs, found along the ATF were hence used as evidence to support a suggested creep-model (Anderlini, Serpelloni, and Belardinelli, 2016). However, compared to the creeping section of the Japan Trench (8 cm/yr; Uchida et al., 2003) or the Chihshang fault in Taiwan (~ 2 cm/yr; Chen, Nadeau, and Rau, 2008), creep along the ATF should happen on a scale of mm/yr (Anderlini, Serpelloni, and Belardinelli, 2016). Hence, the time intervals between consecutive REs along the ATF, as well as the seismic moment M_0 should significantly differ from the REs found along the former mentioned sections (Chen, Nadeau, and Rau, 2008; Uchida et al., 2003).

Based on observations along the creeping section of the San Andreas fault (~ 2 cm/yr) Nadeau and Johnson (1998) proposed an empirical scaling law which relates the seismic moment M_0 of a RE directly to the slip d via $d = 10^{-2.36} M_0^{0.17}$. This empirical law was later slightly modified, based on observations for larger sections of the San Andreas Fault system and modeling approaches (Nadeau and McEvilly, 1999). Beeler, Lockner, and Hickman (2001) proposed a model considering the shear modulus μ , the stress drop $\Delta\sigma$ and the hardening coefficient C . Schmittbuhl et al. (2016) and Yao et al. (2017) instead used the standard crack model to estimate the slip (d):

$$d = \frac{M_0}{\pi\mu a^2} \quad (5.4)$$

Figure S2 (in Supporting Information C) shows that the Beeler, Lockner, and Hickman (2001) and Nadeau and Johnson (1998) models predict relatively high slip rates for small seismic moments, whereas the standard crack model (Schmittbuhl et al., 2016; Yao et al., 2017) predicts the smallest slip values (Uchida, 2019). In the next section, we will apply the standard crack model for estimating values of slip for REs along the ATF, with the premise that the estimated slip indicates a sort of lower limit of expected slip.

Using the standard crack model (Schmittbuhl et al., 2016; Yao et al., 2017), to estimate slip we obtain values for each RE in the order of mm (Tab. S1 in Supporting Information C), which is similar to the annual extension (Anderlini, Serpelloni, and Belardinelli, 2016). We sum up the resulting slip of each family of REs and divide it by its duration. This yields a slip rate for every family of REs. Due to the short time intervals between consecutive REs (Figure S1 in Supporting Information C), the resulting slip rates are several magnitudes larger than the annual extension of the study area (Figure 5.3a; Figure S3 in Supporting Information C).

We shed further light on the resulting slip by inverting a theoretical stress drop $\Delta\sigma$ for realistic slip rates. Hence, we combine equations 5.3 and 5.4. We use the duration of each family of REs and the annual extension of the study area (2 mm/yr) to obtain a slip value d . We further use the cumulative seismic moment M_0 of each family, a shear-modulus μ of 30 GPa and thereby obtain a theoretical stress drop $\Delta\sigma$ for each family of REs. This theoretical stress drop $\Delta\sigma$ is further divided by the number of events which yields theoretical stress drop $\Delta\sigma$ for each RE. The theoretical stress drops $\Delta\sigma$ are in the range of Pa (Tab. S1 in Supporting Information C).

We further relate the corner frequency to the source radius (eq. 5.3) following Brune (1970) to obtain a theoretical corner frequency f_c for each event. We therefore use a P-velocity of 6.5 km/s (Chiaraluce et al., 2007) and a k parameter of 0.32 (Madariaga, 1976). That results in theoretical values for the corner frequency f_c , mainly smaller than 1 Hz (Tab. S1 in Supporting Information C). Compared to the corner frequencies f_c we inferred directly from the waveforms of REs using Brune

(1970) and Boatwright (1980) model, the theoretical corner frequencies f_c are several orders of magnitude smaller (Figure 5.2; Tab. S1 in Supporting Information C).

We see this as an indication that the found families of REs might not be directly related to creep along the LANF. As a result, we expand our investigation for a reasonable mechanism, driving the seismicity along collocated patches.

5.4 Approximating the Fluid Pressure

In the previous section we found indication that creep along the LANF surface, derived from geodetic data (Anderlini, Serpelloni, and Belardinelli, 2016), is difficult to reconcile with the short time between consecutive REs. We consider this finding as an indication that the mechanism driving REs may be related to a different physical process.

There is evidence for abundant CO₂ flux within the study area (Chiodini et al., 2000) which represents a constant supply of ascending fluids (Collettini and Barchi, 2002). If we consider the ATF to be an impermeable horizon that confines fluid ascent (Collettini and Barchi, 2002), we expect a large pore-fluid overpressure below the seal. This model is supported by direct measurements at the San Donato borehole at 4.7 km depth, where Chiodini and Cioni (1989) measured a pore-fluid overpressure of 100 MPa. Due to these increased values, we propose fluctuations of the pore-fluid pressure as an alternative mechanism to drive REs.

Generally, re-shearing of an existing fault follows Amonton's law

$$\tau = \mu_s \sigma_{eff} \quad (5.5)$$

where τ is the shear stress, μ_s the coefficient of friction and σ_{eff} the effective normal stress which depends on the normal stress σ_n and the pore-fluid pressure P_f . This relationship can be written as $\sigma_{eff} = \sigma_n - P_f$. Once the τ/σ_{eff} ratio surpasses the coefficient of friction μ_s , frictional sliding occurs. Therefore, an increase of pore-fluid pressure P_f is able to trigger re-shearing of existing faults.

Collettini (2003) found that reactivation of the LANF can occur if the pore-fluid overpressure reaches quasi lithostatic stress ($P_f/\sigma_v > 0.93$) which corresponds with values between 150 – 250 MPa in depth range between 6 – 10 km.

During frictional sliding, pore-fluid overpressure can be released. The resulting drop in pore-fluid pressure ΔP_f can be approximated following Baisch and Harjes (2003),

$$\Delta P_f = \frac{\Delta \sigma n}{\mu_s} \quad (5.6)$$

where n is the number of events in each family of REs, the stress drop $\Delta \sigma$ is assumed between 1 – 30 MPa, and the coefficient of friction $\mu_s = 0.6$. This results in values of pore-fluid pressure change ΔP_f between 3 – 150 MPa, depending on the family (Figure S4 in Supporting Information C).

Following Cochran et al. (2018), we further divide the cumulative pore-fluid pressure change ΔP_f of each family by its total duration, yielding a rate of pore-fluid pressure change (Figure 5.3b). As seen in figure 5.3b, the values range between Pa/s to kPa/s.

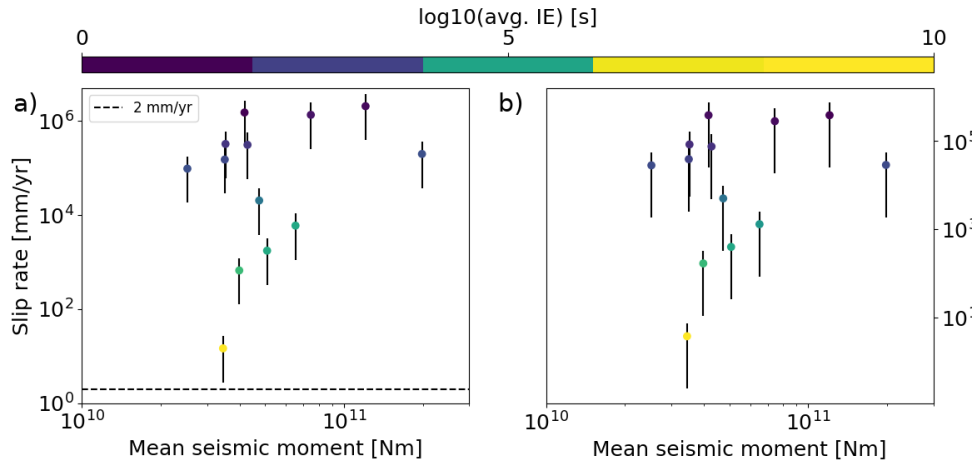


FIGURE 5.3: (a) Slip rate as a function of mean seismic moment for the found families of repeating earthquakes (REs). Slip rates are estimated by the slip derived by the standard crack model (Schmittbuhl et al., 2016; Yao et al., 2017) divided by the duration of RE families. The horizontal dashed line indicates the annual extension of the study area (Anderlini, Serpelloni, and Belardinelli, 2016). (b) Estimated rate of pressure change (Baisch and Harjes, 2003; Cochran et al., 2018) as a function of mean seismic moment for each family of REs. The bars indicate the resulting range as we assume stress drops $\Delta\sigma$ between 1 and 30 MPa.

5.5 Discussion

A possible mechanism leading to REs is that rate-weakening patches that are embedded into a fault that is mostly creeping (rate-strengthening environment), are frequently brought to seismic failure. As the rate of creep that surrounds the seismic patches controls the time intervals between consecutive REs, they can be used to infer the rate of aseismic creep (Beeler, Lockner, and Hickman, 2001; Nadeau and Johnson, 1998; Schmittbuhl et al., 2016; Yao et al., 2017).

Within the study area, REs are found (Chiaraluce et al., 2007; Valoroso et al., 2017) and used as additional evidence for creep along a LANF (Anderlini, Serpelloni, and Belardinelli, 2016). As the time intervals between consecutive REs were found to be small ($1e2 - 1e5$ s), Essing and Poli (2022) argued that other mechanisms than creep could possibly better explain the occurrence of REs.

To reassess the REs of the study area, we make use of a standard crack model (Schmittbuhl et al., 2016; Yao et al., 2017) to infer values of slip for found REs. The estimated slip is in the range of mm (Tab. S1 in Supporting Information C) which corresponds to the annual extension within the study area (Anderlini, Serpelloni, and Belardinelli, 2016). While these values of slip appear to be reasonable at first sight, there are additional things to consider.

First, the values are estimated using the standard crack model (Schmittbuhl et al., 2016; Yao et al., 2017), which produces the lower bound of expected slip values for events of small seismic moment (Figure S2 in Supporting Information C). Other proposed models (Beeler, Lockner, and Hickman, 2001; Nadeau and Johnson, 1998) would result in larger slip values (Uchida, 2019), which are then difficult to reconcile with the annual extension of 2 mm.

Second, the time interval between consecutive REs is mainly relatively short ($1e2 - 1e5$ s). Combining these short time intervals with the estimated slip of each

family of REs yields slip rates of the order of cm/yr up to m/yr (Figure 5.3; Figure S3 in Supporting Information C). Again, this is difficult to reconcile with the overall rate of extension of the study area (Figure 5.3). One could argue that creep in the study occurs in an intermittent way which would allow for slightly larger slip rates in relatively short time intervals. However, a substantial portion of families of REs exhibit slip rates in the order of cm/yr up to m/yr (Figure 5.3).

In order to obtain reasonable slip rates within the expected range, an extremely low stress drop with corresponding small corner frequency in the range of low frequency earthquakes would be needed (Tab. S1 in Supporting Information C). In table S1 (in Supporting Information C), we compare the estimated and theoretical corner frequency for all REs, which shows that estimated corner frequency are several orders of magnitude larger than the theoretical ones. Therefore, we posit that another mechanism than aseismic slip could be active to produce the fast reoccurring, REs (Collettini and Barchi, 2002).

We propose an alternative mechanism that is able to explain the continuous micro-seismicity as well as the peculiar REs within the study area. This mechanism is related to the recognized abundance of fluids (Chiodini et al., 2000) and pore-fluid overpressure (Chiodini and Cioni, 1989), and combines two existing, conceptual models (Baisch and Harjes, 2003; Collettini and Barchi, 2002).

Similar to Collettini and Barchi (2002) we assume the ATF to represent a barrier in form of an impermeable horizon that traps fluids coming from the deeper part (Chiodini et al., 2000). As the ascent of the CO₂ rich fluids is stopped below the sealing ATF, a constant increase in pore-fluid pressure should be observed below the LANF. This leads to - assuming a constant supply of fluids from below - a constant increase in pore fluid pressure. Collettini and Barchi (2002) showed that re-shearing along the LANF can occur if the pore-fluid pressure is about to reach the lithostatic pressure which is in the range of 150 to 250 MPa at depths between 6 to 10 km.

Once the lithostatic pressure is reached (Figure 5.4), re-shearing along preexisting cracks will occur (Collettini and Holdsworth, 2004). This will lead to a constant radiation of micro-seismicity, as found along the LANF (Chiaraluce et al., 2007). During the re-shearing, pressurized fluids can escape upwards and reduce the pore-fluid pressure in direct vicinity. In some cases, the release of fluids and the associated drop in pore-fluid pressure is quickly reloaded leading to a follow up re-shearing (Baisch and Harjes, 2003).

Following the approach of Baisch and Harjes (2003), we estimated the change of pore-fluid pressure related to families of REs to be around 3 – 150 MPa. These values are in a similar range as both, the lithostatic pressure at depth as well as the measured pore-fluid overpressure at the San Donato borehole (Chiodini and Cioni, 1989). It is furthermore in the same range as inferred for a human induced injection environment in southern Kansas (Cochran et al., 2018). Additionally, the estimated values of the rate of pore-fluid pressure change are in a similar range as measured at a well-head in the Cooper Basin in Australia (Baisch, 2020).

Following rate-and-state friction one could argue that an increase of pore-fluid pressure would stabilize the fault (Ruina, 1983; Gu et al., 1984), preventing the development of unstable slip (Guglielmi et al., 2015). However, Scuderi, Collettini, and Marone (2017) used laboratory experiments to demonstrate that the influence of effective normal stress on fault strength and stability might potentially overcome the rate-and-state dependent effects.

Finally, we want to emphasize here that the families of REs discovered within the study area are difficult to utilize as evidence for creep. However, this does not rule

out aseismic creep along the LANF as a mechanism for accommodating the overall extension.

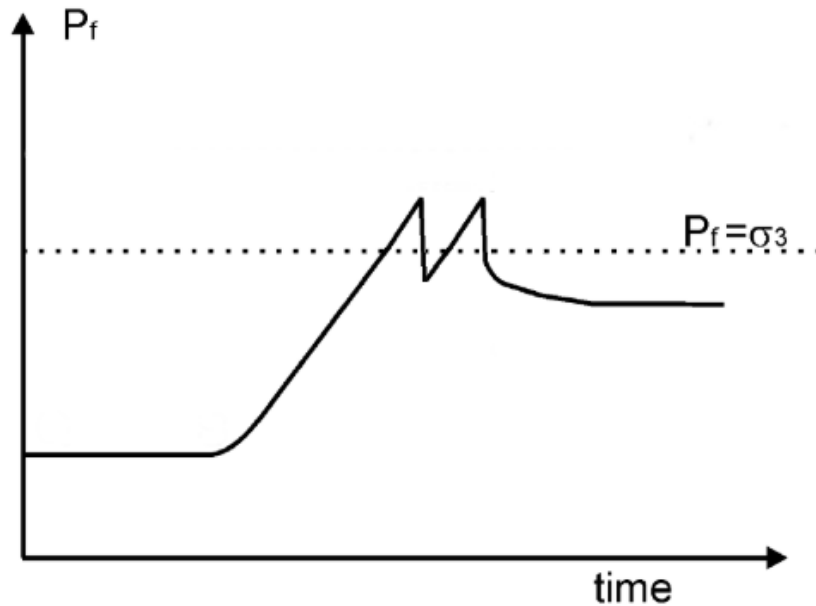


FIGURE 5.4: Conceptual model of the mechanism that could explain rapid repeating earthquakes. Over time, local pore-fluid pressure (P_f) increases. Once the P_f reaches a threshold (i.e., least principal stress (σ_3) acting on the fault), re-shearing of existing cracks occurs. Concomitant to the re-shearing, fluids are escaping the sealing, which leads to a temporal and local pressure decrease. However, as the global increase of P_f is continuing, re-shearing conditions are reached again in short time intervals, radiating a second seismic event.

5.6 Conclusion

In the presented work we extracted families of REs, located in direct vicinity of a LANF. The found families exhibit mainly short time intervals between consecutive REs. To get insights about their driving mechanisms, we first related the released seismic moment of each event to slip, using the standard crack model (Schmittbuhl et al., 2016; Yao et al., 2017). Using the short time intervals between consecutive REs within a family we further obtained slip rates. We found slip rates in a range larger than the study area's annual extension, making the families of REs difficult to reconcile with creep along the LANF as a potential driving mechanism.

To better explain the observed fast recurrences of REs, we introduced a combination of two models where pore-fluid overpressure below a sealing LANF can only be released by re-shearing of preexisting cracks (Baisch and Harjes, 2003; Collettini and Barchi, 2002). With re-shearing of the crack, trapped fluids can escape which leads to a fast decrease of the pressure, and a subsequent crack closing. In some occasions, the pore-fluid overpressure recovers within short time intervals which leads to a quick release of a second seismic event from a similar location. The estimated pressure change as well as its rate are in agreement with findings within induced seismicity environments.

Chapter 6

Final Conclusions & Outlook

6.1 Final Conclusion

The work shown in the here presented thesis can be subdivided into two parts. First, I made use of a dense seismic network recording high quality data in combination with most recent developed earthquake detecting methods in order to obtain a high-resolution catalog down to small magnitude earthquakes. Second, I used tools from classical statistics, unsupervised learning and seismological observations to analyse the behavior as well as the interaction of the seismicity in space and time. The analysis helped to better understand the mechanisms that accommodates the extension along the Alto Tiberina fault, a low-angle normal fault (LANF) in the Northern Apennines in Italy.

More precisely, in chapter 3, matched-filter processing (Beaucé et al., 2019; Gibbons and Ringdal, 2006) was applied to data recorded at an array of borehole stations and helped to expand an existing catalog by a factor of ~ 12 . With this approach the capability to detect small events was improved and therefore helped to analyse the seismicity in unprecedented high details. It further enabled the identification of several types of seismicity within the study area which might be related to different driving mechanisms.

Two modes of seismicity are recognised within the shallow part of the study area. First, marginal temporal and spatial clustering between seismic events is seen during times of constant surface deformation. With the beginning of a transient deformation signal (Gualandi et al., 2017), the shallow seismicity begins to be strongly clustered in space and time. This behavior is interpreted as enhanced interaction of seismicity that reflects the complexity of the slip process during the deformation transient (Cattania and Segall, 2021; Dublanchet, Bernard, and Favreau, 2013).

The deeper part of the fault system appears to be largely disconnected from activity in the hanging wall (HW). Here, repeating earthquakes (REs) are identified and modeled that illustrate the marginal role of creep in controlling their occurrence. Therefore, deformation models different to creep could account for the extension within the study area (Cianetti et al., 2008; Lambotte et al., 2014; Le Pourhiet, Burov, and Moretti, 2003). To further explain the occurrence of REs, rapid fluctuations in pore-fluid pressure are proposed, which are shown to be in good agreement with geological and induced seismicity studies (Baisch and Harjes, 2003; Cochran et al., 2018; Collettini and Barchi, 2002).

In chapter 4, I aim to automatically extract clustered seismicity within the catalog that was obtained in chapter 3. Therefore, a data-driven approach developed within the framework of recent unsupervised clustering methods is applied. Similar to already applied methods (Zaliapin et al., 2008; Zaliapin and Ben-Zion, 2013a; Zaliapin and Ben-Zion, 2013b), the approach is based on single linkage clustering (i.e., nearest neighbor). However, the advantage of the presented approach is that it accounts

for a non-stationary background seismicity rate and is further able to automatically subdivide the clustered seismicity into seismic bursts of different behavior. Additionally it is computationally efficient, which allows to apply it to large earthquake catalogs.

The detailed analysis of the extracted clustered seismicity indicates that a large portion of small-scale seismic bursts could be related to aseismic processes which adds evidence to recent findings within the study area (Essing and Poli, 2022; Gualandi et al., 2017).

It further exhibits that the complexity of the 2014 ATF swarm sequence could probably arise from the ensemble of various small-scale aseismic transient events, interacting within a cascade-framework.

In chapter 5, the work related to REs of chapter 3 is extended. Therefore, event families of REs are extracted. The estimate of slip from the released seismic moment of each event combined with short time intervals between consecutive events yields slip rates several orders of magnitude larger than expected for the study area (Anderlini, Serpelloni, and Belardinelli, 2016).

To better explain the observed short time intervals between collocated events, a combination of two models is proposed. Here, pore fluid overpressure below a sealing LANF is released by re-shearing of fractures (Baisch and Harjes, 2003; Collettini and Barchi, 2002). With re-shearing of the fractures, trapped fluids can escape which leads to a fast decrease of the pore-fluid pressure, and a subsequent fracture closing. Re-shearing can only occur as long as the decreasing fluid overpressure is above a certain threshold. In some rare occasions, the pore-fluid overpressure recovers within short amounts of time, which leads to a fast re-shearing of the same fracture.

The combination of the different findings in chapters 3, 4, and 5 helped to get a better understanding of the way how the extension could potentially be accommodated within the study area.

First, in chapter 1 and 3 we have seen that other mechanisms than creep along the LANF could produce a similar surface expressions. Furthermore, in chapter 3 and 5 we could see that REs cannot be reconciled with creep, but could potentially be driven by pore-fluid over-pressure that was directly measured within boreholes (Chiodini and Cioni, 1989).

Additionally to the two proposed models that use strain release along the LANF, a third model related to the HW could also explain the release of accommodated strain. Chapter 3 brought evidence, that the HW is affected by synchronous activation of large parts, which could be seen as indication for aseismic deformation there, which is in good agreement with findings from GNSS data (Gualandi et al., 2017). If a considerable portion of the accommodated extension is released here, the deeper portions may only release a tiny portion of the extension.

6.2 Outlook

6.2.1 Automated Clustering of Large Seismic Catalogs

In chapter 4, I presented an approach of unsupervised clustering in order to automatically extract groups of earthquakes that are clustered in space and time. This approach is able to extract bursts of seismicity, which analysis showed evidence for their driving mechanism.

The approach depends on several pre-processing steps as well as on two hyper-parameters which were extensively tested with the input data-set (see Chapter 4).

However, I started to additionally test the approach in different study areas, related to seismicity driven by volcano or post-seismic related mechanisms which will help to better understand the pre-processing steps as well as the hyper-parameter tuning. Additionally, the presented approach could potentially be able to extract meaningful clusters of earthquakes from other tectonic environments.

Furthermore, I will test this approach on synthetic earthquake catalogs, retrieved from a epidemic type aftershock sequence model (ETAS). A synthetic environment allows to better quantify the clustering outcome, which will help to better understand potential pit-falls with the clustering pipeline.

Finally, an extensive comparison with other de-clustering methods like Zaliapin et al., 2008; Zaliapin and Ben-Zion, 2013a; Zaliapin and Ben-Zion, 2013b; Aden-Antoniów, Frank, and Seydoux, 2022 which have been shown to work well in MS-AS environments will help to better understand advantages and disadvantages of different approaches.

6.2.2 Combine GNSS Data with Seismic Catalogs

In this thesis, slow deformation processes, lasting up to ~ 6 months, have been proposed to accommodate the extension within the study area. These processes are called slow, as they occur on time scales of days to months, which is several orders of magnitudes faster than fast deformation as seen during common earthquakes (\sim seconds). Due to the large time scales at which these processes occur, the detection on common seismometer is not possible.

Therefore, geodetic measurements (GNSS, InSAR, LiDAR) are required as they are able to sample down to very low frequencies. The drawback of geodetic measurements is their blindness for high frequencies as well as their relatively high detections threshold (cm-scale).

To combine the two approaches and obtain a larger spectrum of frequencies to observe, recent studies used geodetic and seismic observations. This approach has led to an increase of findings related to slow deformation processes (Jolivet and Frank, 2020).

In the study area presented in this work, annual deformation is happening on scales of mm. This makes the finding of slow deformation signals in geodetic data extremely difficult.

Nevertheless, Gualandi et al. (2017) were able to detect a transient deformation signal from continuous GNSS data making use of an independent component analysis.

During this study, I worked on a simpler approach by using the recordings of two GNSS stations (ATBU, MVAL), placed on the two sides of the Gubbio fault (Figure 1.2). The overall tectonic trend was removed from displacement data of the two stations and the north components were rotated towards NNW (along the strike of the Gubbio fault) while the east components were rotated normal to NNW. In order to remove annual trends, the two stations were subtracted from each other resulting in the signal as seen in figure 6.1b.

From figure 6.1b we can see a flat deformation signal from 2010 to 2012. In mid 2012 a small decrease in distance between the stations can be seen. This gentle decrease is followed by a stronger increases that starts slightly before the onset of swarm seismicity at the end of 2013 (Figure 6.1).

This approach shows that one could possibly detect small scale deformation signals within the study area, using basic approaches. However, for future work also more sophisticated approaches like the independent component analysis (ICA) as

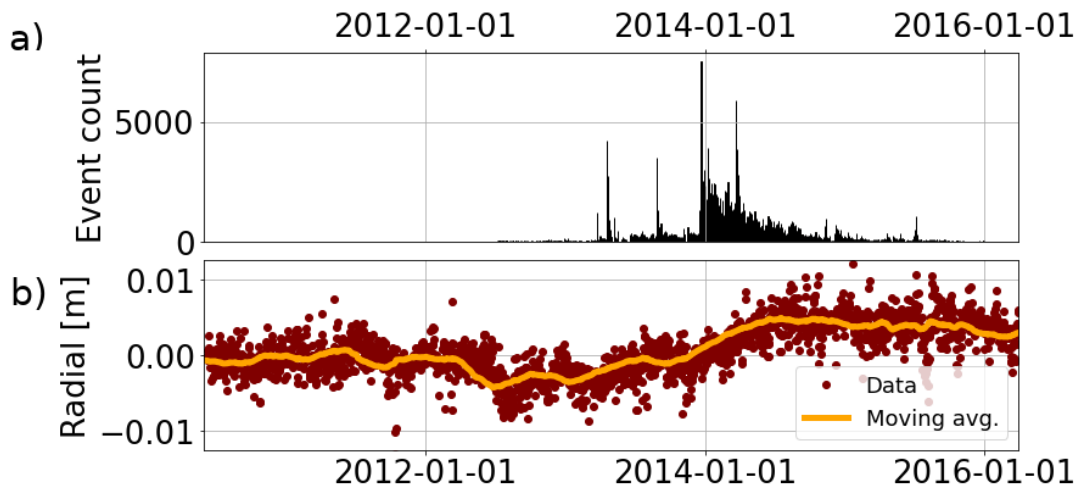


FIGURE 6.1: (a) Event count (10-days window) of the seismicity within the study area as detected in chapter 3 (July 2013 - December 2012). (b) Substracted GNSS signal and its moving average of ATBU and MVAL.

used by Gualandi et al. (2017) could be possibly applied to extend the search for aseismic deformation processes over longer time scales.

6.2.3 2023 Umbertide Sequence

In 2023-03-09 (8 days before the submission of this thesis), two earthquakes $M \sim 4$ were reported for the study area by the National Institute of Geophysics and Volcanology (INGV). The two earthquakes happened in close vicinity to each other within the shallow part of the area (5 – 10 km). Their reported focal mechanisms indicate that both earthquakes occurred along high dip angles ($> 30^\circ$).

This sequence is of large interest in many ways. First, as seen in figure 6.2, these are the largest reported events within the last 13 years. Indeed, they are the largest events recorded since 1984. Second, they occurred at a depth, close to the upward projection of the LANF. This is the area where the LANF is proposed to be locked (Anderlini, Serpelloni, and Belardinelli, 2016). Third, they occurred very close to each other in space and time. Fourth, considering the seismicity reported by the INGV, there is no sign of foreshocks preceding the first event.

The provided focal mechanisms (Figures in Supporting Information D) are similar in dip and strike to the one of the Citta di Castello sequence in 2013, which was supposed to occur on a high angle fault at shallow depth and close vicinity to the projection of the LANF (Valoroso et al., 2017).

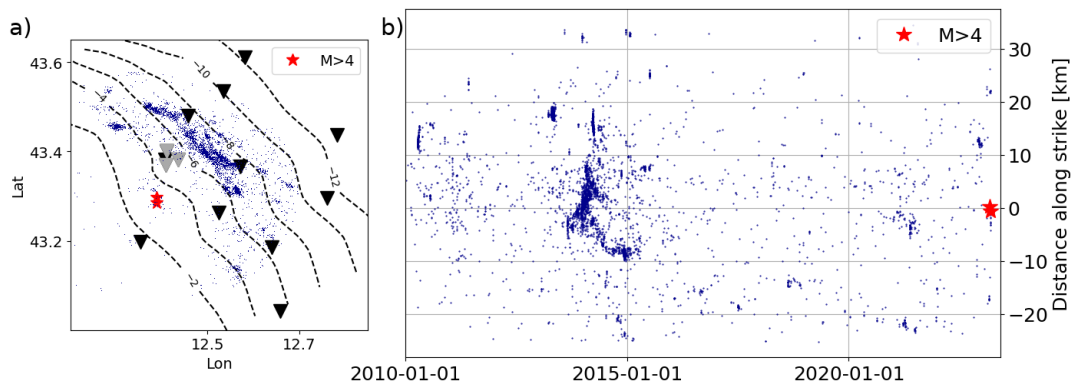


FIGURE 6.2: (a) Seismicity ($M > 0.5$) of the last 13 years as reported by the INGV. Stations of the TABOO observatory are indicated as triangles. (b) Space-time evolution of the seismicity seen in (a).

Appendix A

Supporting Information for Spatiotemporal evolution of the Seismicity in the Alto Tiberina Fault System revealed by a High-Resolution Template Matching Catalog¹

¹Published as Essing, D., & Poli, P. (2022). Spatiotemporal Evolution of the Seismicity in the Alto Tiberina Fault System Revealed by a High-Resolution Template Matching Catalog. *Journal of Geophysical Research: Solid Earth*, 127(10), e2022JB024845.

1 **Spatiotemporal evolution of the Seismicity in the Alto Tiberina Fault System revealed by a**
2 **High-Resolution Template Matching Catalog**

3

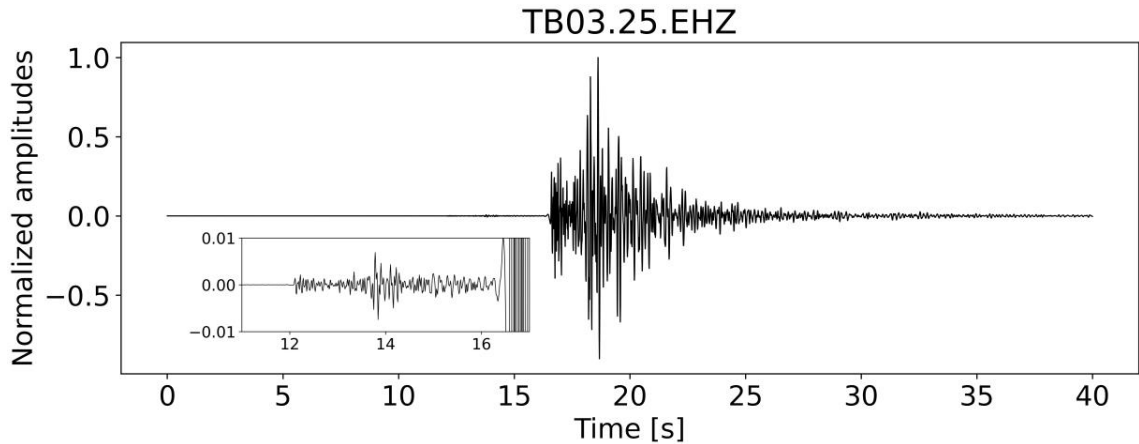
4 **David Essing^{1*}, Piero Poli¹**

5 ¹ISTerre Institut des Sciences de la Terre, CNRS, Université Grenoble Alpes, France.

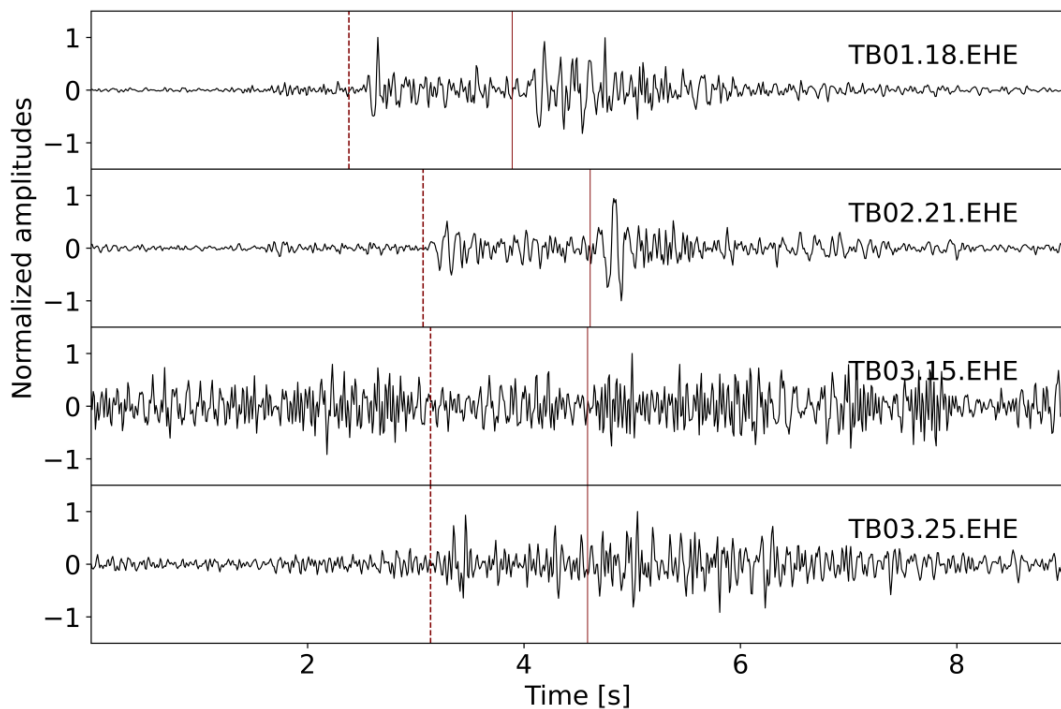
6 Corresponding author: David Essing (david.essing@univ-grenoble-alpes.fr)

7 Université Grenoble Alpes, ISTerre CS 40700 38058, GRENOBLE Cedex 9

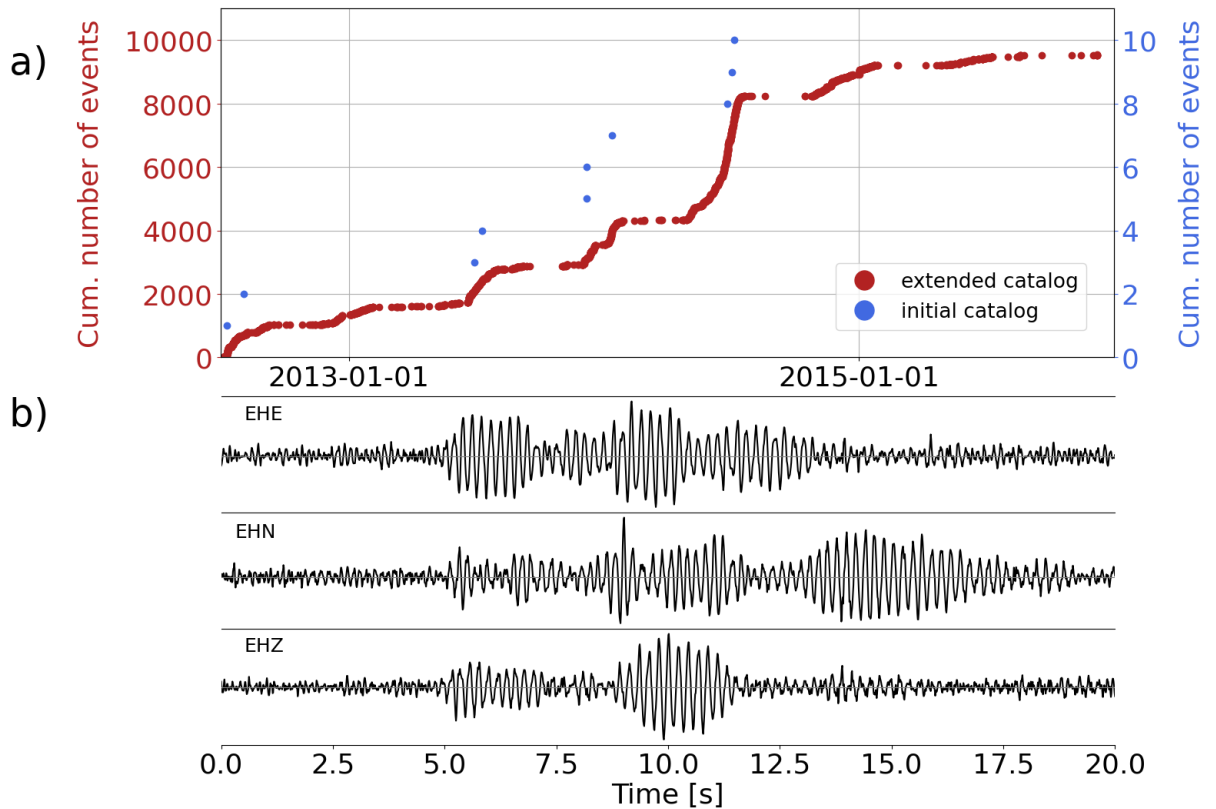
8



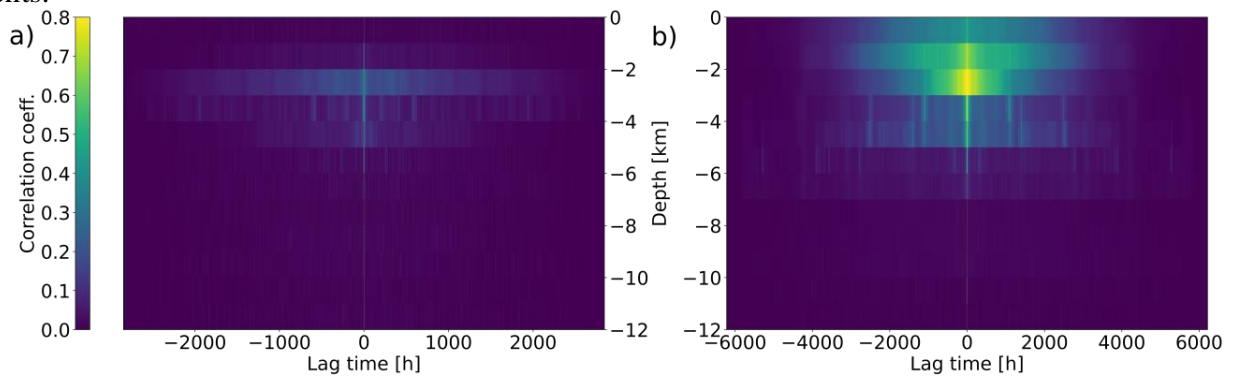
9
 10 **Figure S1:** Normalized waveform of a $M= 2.8$ event (2014-12-20T12:14:24) at station TB03.25.
 11 The zoomed inset allows to see a smaller event $M\sim 0.2$ preceding the larger event by 3 s.
 12 Notably, both events share elevated similarity in terms of waveforms, having a high CC of
 13 ~ 0.66 .
 14
 15



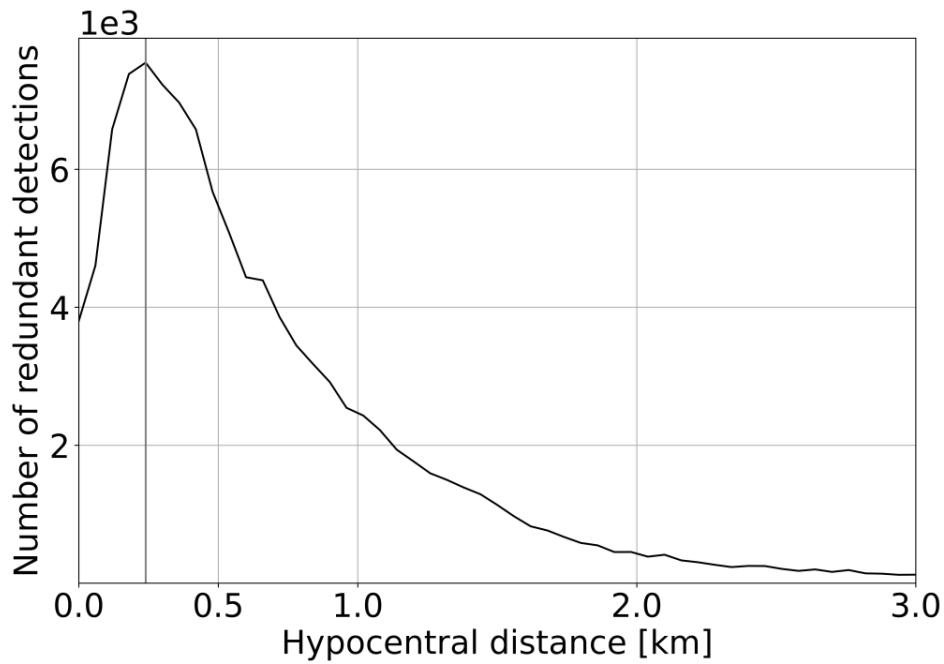
16
 17 **Figure S2:** Normalized waveforms for the East components of all used stations of two
 18 consecutive events (2013-12-21T22-57-54.75 and 2013-12-21T22-57-56.33) following each
 19 other by ~ 1.5 s. The red dashed line indicates the theoretical s-wave arrival time assuming the
 20 travel time of the detecting template. The red solid line indicates the same but for the second
 21 template.
 22



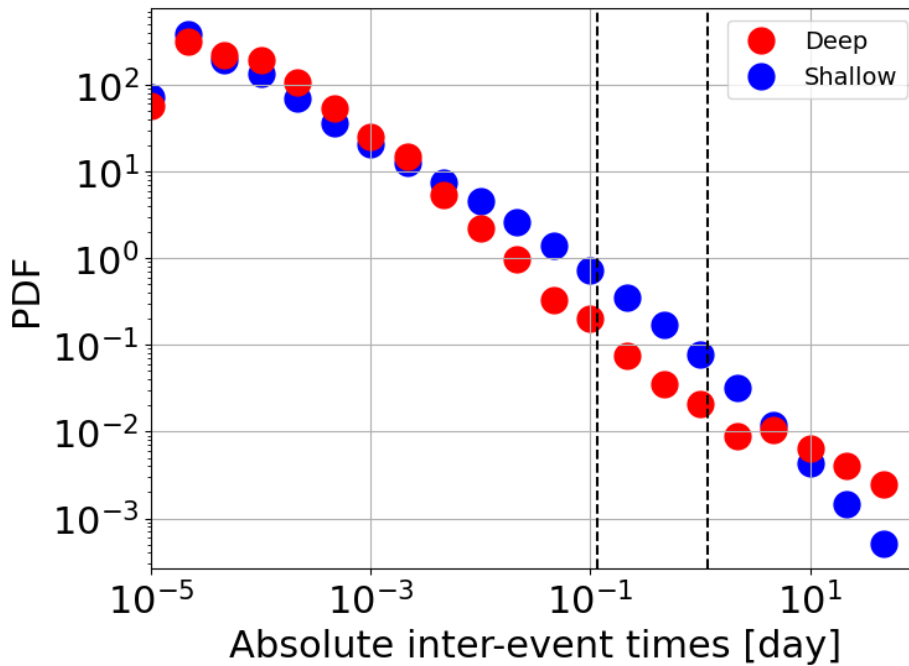
23
 24 **Figure S3:** (a) Cumulative number of events as a function of time for events radiated at shallow
 25 depths close to a cement factory in the southern part of the Gubbio basin. Note the different scale
 26 for the two catalogs. (b) Normalized three-component waveforms recorded at TB02 for one of
 27 the events.



28
 29 **Figure S4:** Auto-correlation functions of the event count time series binned in 1 km along depth
 30 and 1-hour lasting time bins for (a) the pre-swarm and (b) the swarm time period. For both plots,
 31 the color-bar ranges from 0 to 0.8.
 32

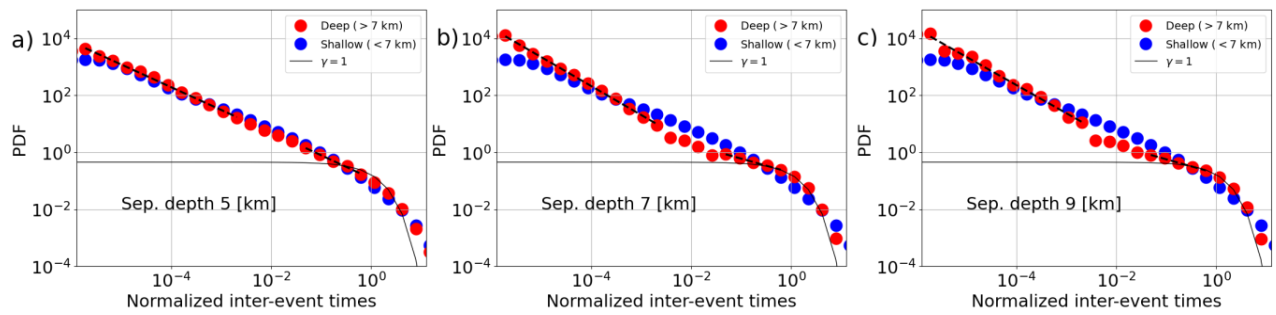


33
34 **Figure S5:** Number of redundant detections as a function of hypo-central distance between the
35 redundant detection and the auto-detection.



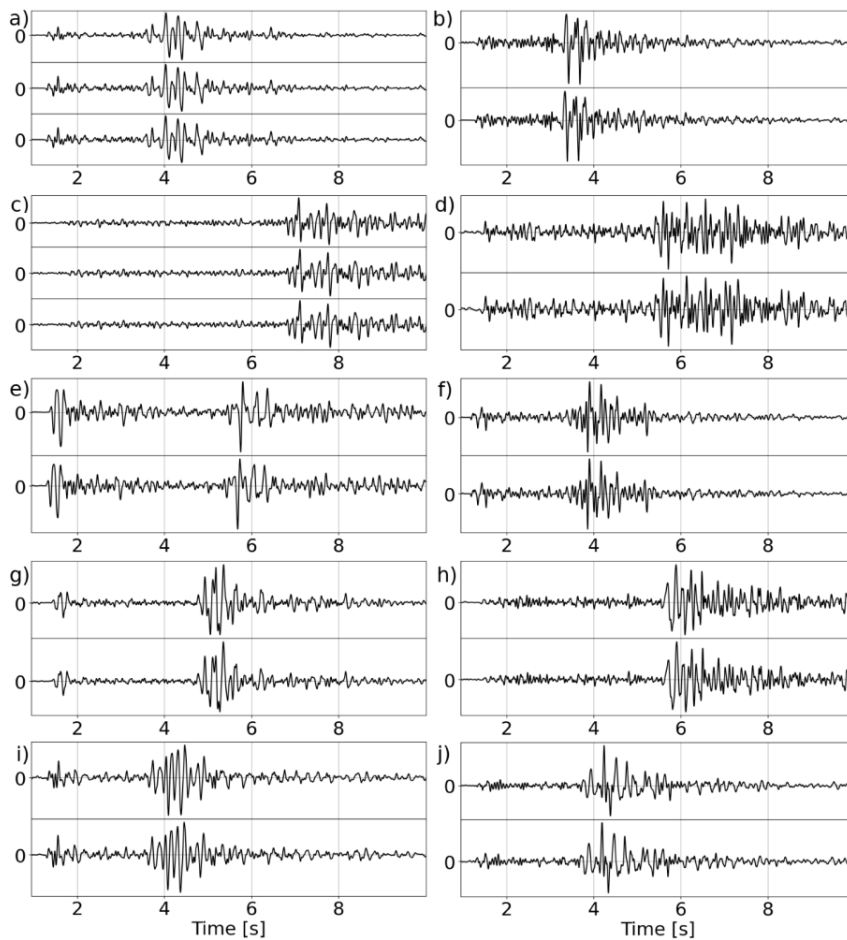
36
37 **Figure S6:** Probability density function for the absolute inter-event times in days for deep (red)
38 and shallow (blue) template families. Vertical dashed black lines indicate the times for separation
39 into short ($<10^4$ s) and long ($>10^5$ s) lasting families.

40
41



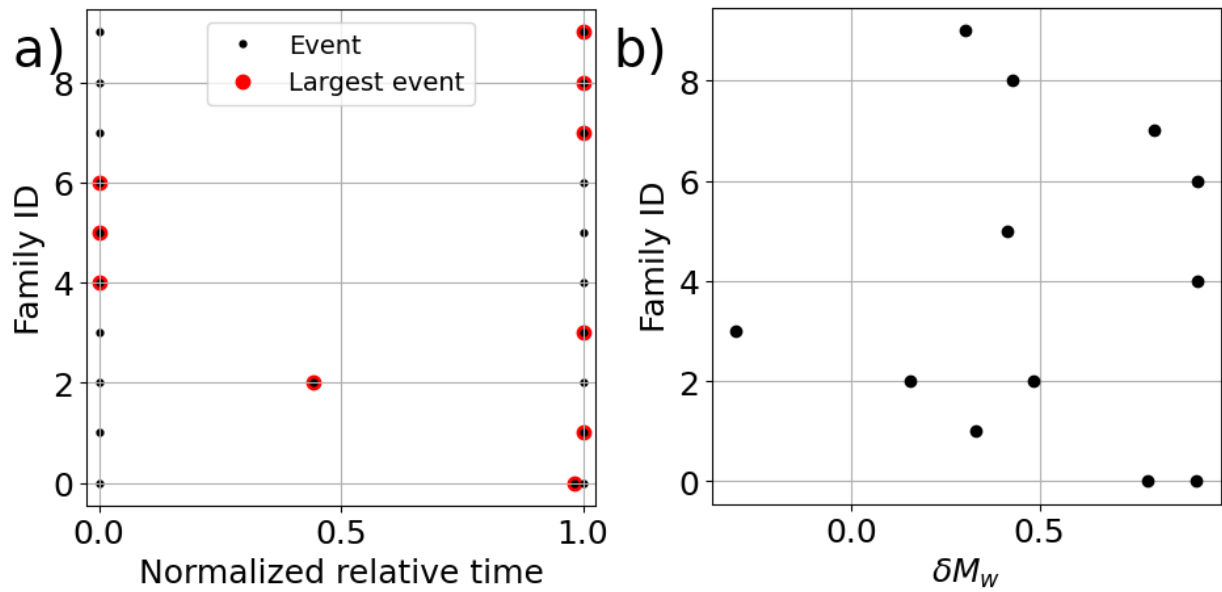
42
43
44
45

Figure S7: As figure 6a but for different separation depths. (a) Separation of seismicity at 5 km. (b) at 7 km. (c) at 9 km.



46
47
48
49
50
51
52

Figure S8: (a) - (g) Normalized waveforms of events with similar waveforms recorded at TB01 east component. See also Table S2.



53
54
55
56
57
58
59
60
61

Figure S9: (a) Normalized relative times for each family of repeating events. Red dots indicate the largest event within a family. (b) The difference between the largest event and the other events within each family in δM_w

Table S1: 1-d p wave velocity model used to predict the arrival times at the stations used in this study (Chiaraluce et al., 2007)

Layer top [km]	p-wave velocity [km/s]
0	4.6
3	5.5
5	6.0
7	6.7
38	7.9

62
63
64
65

Table S2: Families of repeating events. If events within a family were detected by different templates, they have different locations. In this case we computed the average location between them.

lat [deg]	lon [deg]	depth [km]	origin time first event	duration [s]	nr_events	Fig. S8
43.43607 07601	12.59830 9199	8.76996	2013-03-15T07:36:33	9965.625 624	3	a)
43.41519 54651	12.54738 85536	8.21381	2013-03-16T09:17:48	16.41872 8	2	b)
43.23249 30827	12.79992 51684	9.35883	2013-03-16T23:07:36	1110.068 787	3	c)

43.24079 13208	12.67919 34967	8.37477	2013-05- 17T22:17 :12	4722.86	2	d)
43.37870 97931	12.74312 68692	12.17099 5	2013-09- 14T19:19 :33	240.3852 6	2	e)
43.45399 09363	12.57639 12201	8.512165	2013-09- 21T17:08 :56	4942.709 734	2	f)
43.39792 63306	12.69310 66513	9.59176	2014-11- 22T03:42 :20	100.95	2	g)
43.20241 54663	12.66066 07437	8.59461	2015-02- 18T10:14 :04	1798.788 118	2	h)
43.44217 49115	12.60103 36876	9.163845	2015-07- 31T19:30 :15	1366.510 071	2	i)
43.43663 0249	12.62002 75421	9.175625	2015-08- 09T23:21 :46	1836.393 349	2	j)

66

67

68 Logistic function used to weight the maxima of each component wise cross-correlation function
69 depending on the SNR of the correlated waveforms (for more details see Duverger et al., 2018)

70
$$f(x) = \frac{L}{1+e^{-k(x-x_0)}} \quad (1)$$

71 Where $L = 1$, $k = 2.5$, and $x_0 = 3$ (Duverger et al., 2018).

72

73 **Reference**

74 Chiaraluce, L., Chiarabba, C., Collettini, C., Piccinini, D., & Cocco, M. (2007). Architecture and
75 mechanics of an active low-angle normal fault: Alto Tiberina fault, northern Apennines, Italy.
76 Journal of Geophysical Research: Solid Earth, 112(B10).

77 Duverger, C., Lambotte, S., Bernard, P., Lyon-Caen, H., Deschamps, A., & Nercessian, A.
78 (2018). Dynamics of microseismicity and its relationship with the active structures in the western
79 Corinth Rift (Greece). Geophysical Journal International, 215(1), 196-221.

80

Appendix B

Supporting Information for Swarms as a cascade of aseismic transients revealed by unsupervised clustering of earthquakes: The case of the Alto Tiberina 2014 sequence¹

¹Currently under review in Journal of Geophysical Research: Solid Earth. Essing, D., & Poli, P. (2023). Swarms as a cascade of aseismic transients revealed by unsupervised clustering of earthquakes: The case of the Alto Tiberina 2014 sequence.

1 **Swarms as a cascade of aseismic transients revealed by unsupervised clustering of**
2 **earthquakes: The case of the Alto Tiberina 2014 sequence**

3 **David Essing^{1*}, Piero Poli^{1,2}**

4 ¹ISTerre Institut des Sciences de la Terre, CNRS, Université Grenoble Alpes, France.

5 ²Dipartimento di Geoscienze, Università degli Studi di Padova, 35131 Padova PD, Italy

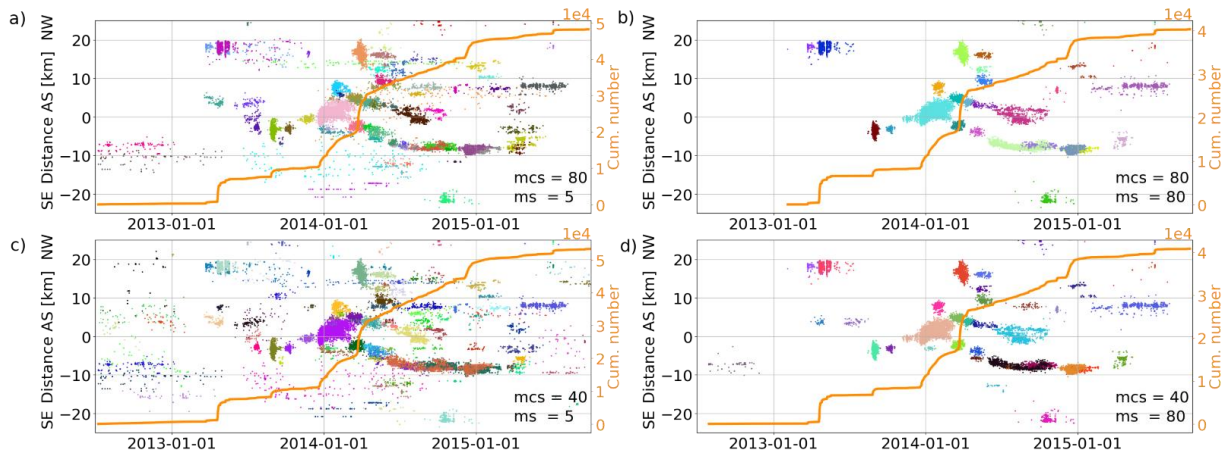
6

7 Corresponding author: David Essing (david.essing@univ-grenoble-alpes.fr)

8 Université Grenoble Alpes, ISTerre CS 40700 38058, GRENOBLE Cedex 9

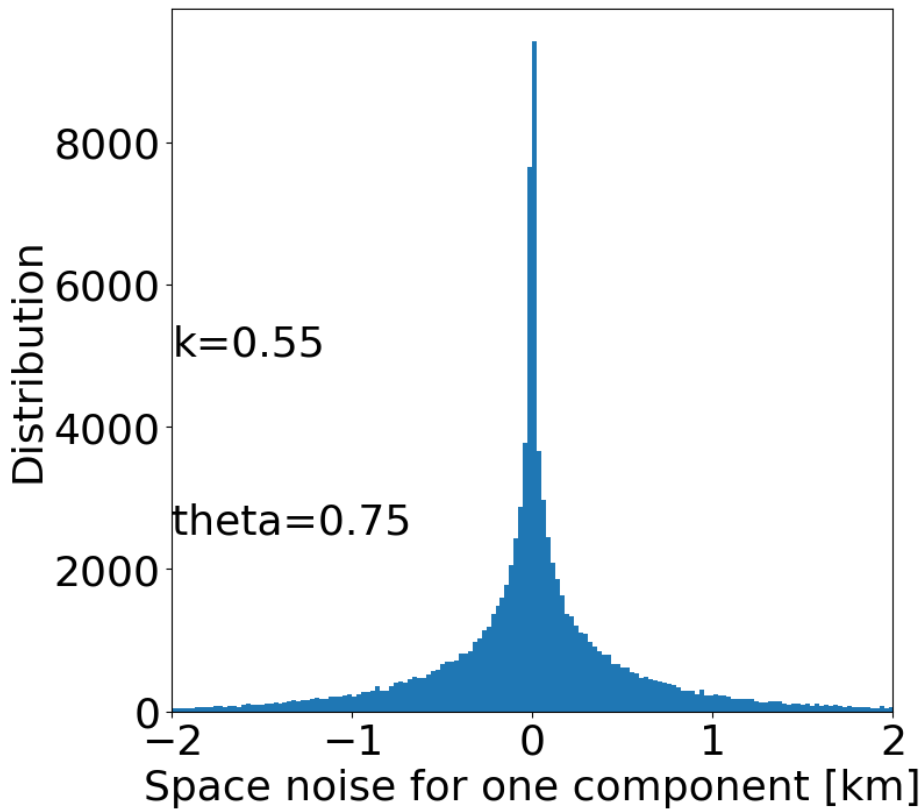
9

10
11



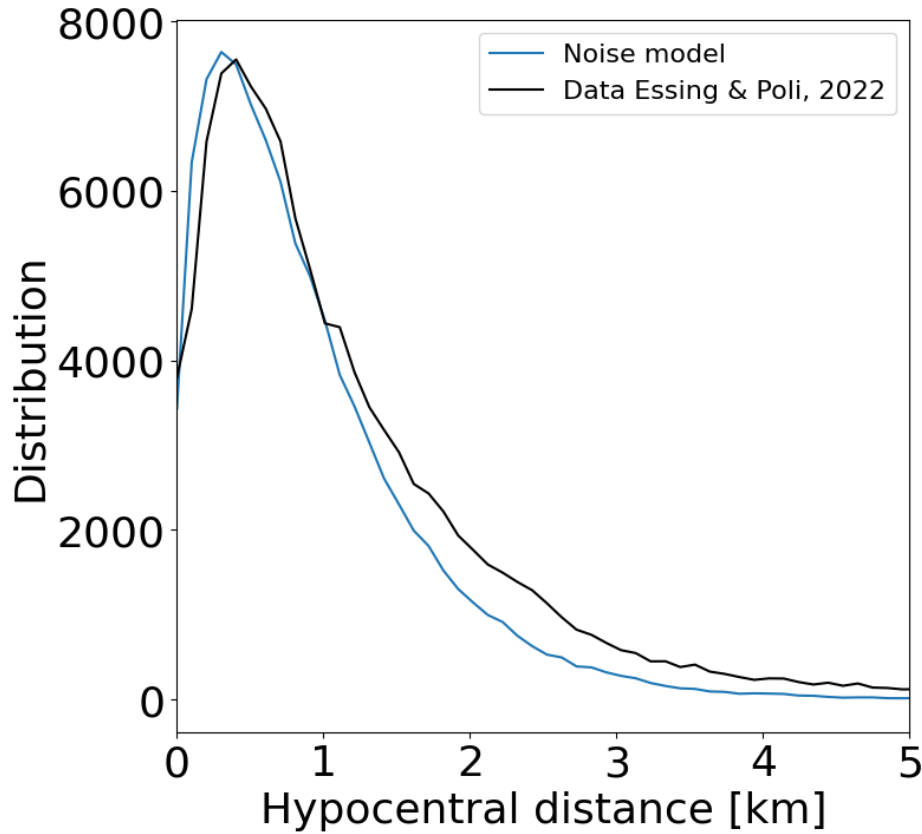
12
13
14
15
16
17
18
19
20

Figure S1: Space time evolution of the clusters resulting from different values for the minimum cluster size and the minimum samples hyper-parameter. a) Minimum cluster size (mcs) = 80, minimum samples (ms) = 5, 50 % of the initial catalog is clustered seismicity and organized within 71 clusters. b) mcs = 80, ms = 80, 42% of the initial catalog is clustered seismicity and organized within 30 clusters. c) mcs = 40, ms = 5, 55 % of the initial catalog is clustered seismicity and organized within 114 clusters. d) mcs = 40, ms = 80, 42% of the initial catalog is clustered seismicity and organized within 38 clusters.

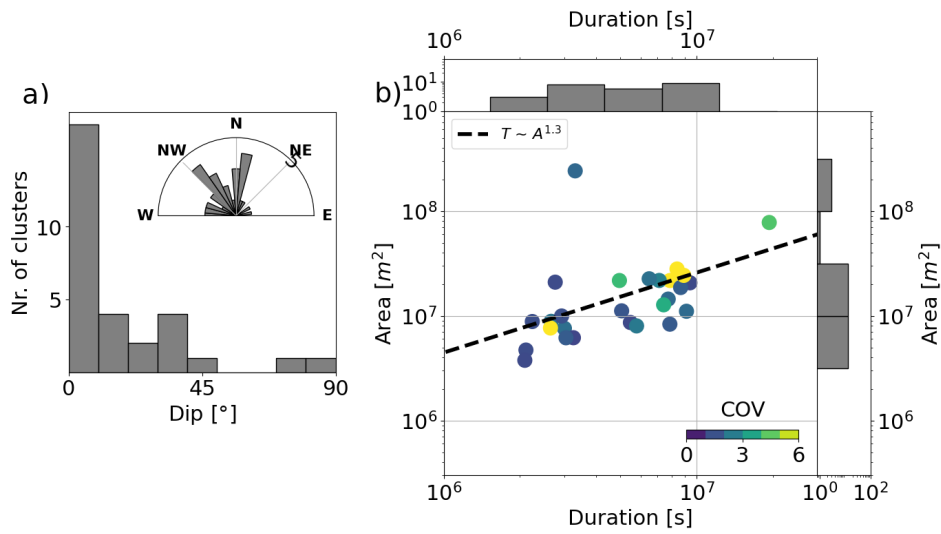


21

22 **Figure S2:** Distribution of the space noise for one space component modeled by a gamma
23 distribution.
24

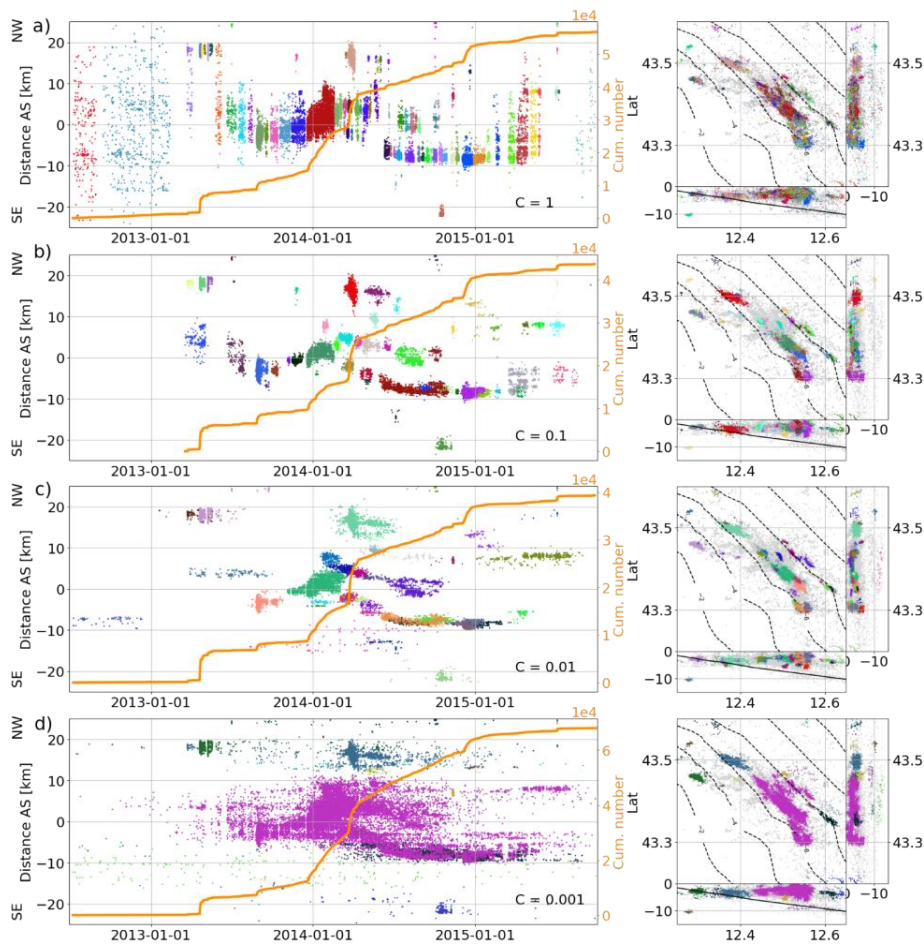


25
26
27 **Figure S3:** Function of redundant detections as a function of hypo-central distance between
28 redundant detections and the auto-detection (Essing & Poli, 2022). Resulting hypo-central
29 distances of three (for x, y, and z) combined distance distributions as indicated in figure S1, which
30 are finally added as space noise to the events of the catalog.
31
32
33
34



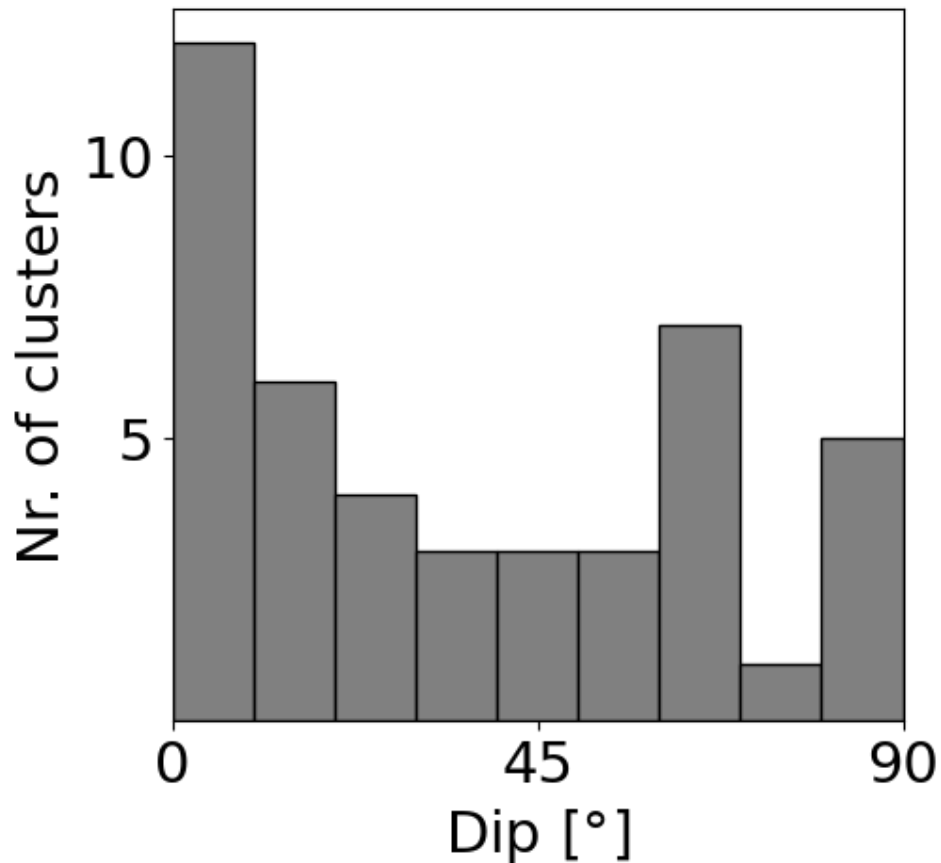
35
36
37
38
39
40

Figure S4: Results when space-homogenization is not applied (Piegari et al., 2022), resulting in 40% clustered seismicity within 30 clusters. (a) Distribution of the dip angles found for the resulting cluster. Inset: Distribution of strike angles. (b) As figure 4b.



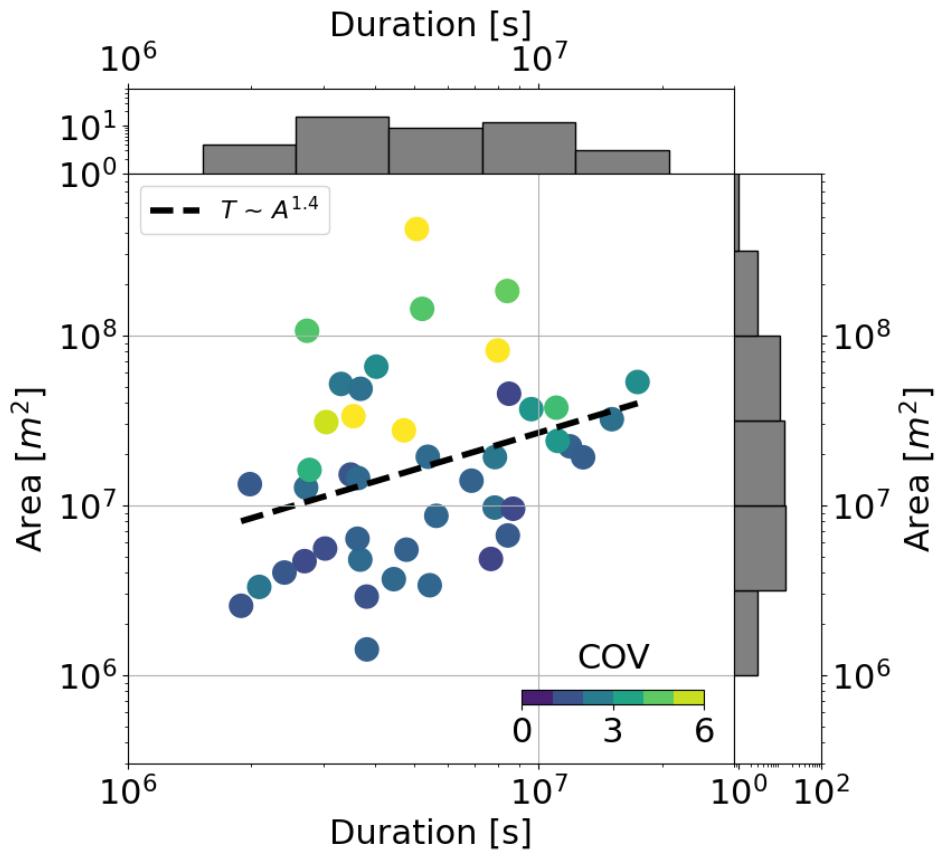
41
42

43 **Figure S5:** Space time evolution (left column) and locations (right column) of the resulting clusters
44 for different C parameters. (a) $C = 1$: clustering results in 59% clustered seismicity within 83
45 clusters. (b) $C = 0.1$: clustering results in 45% clustered seismicity within 54 clusters. (c) $C =$
46 0.01 : clustering results in 40% clustered seismicity in 39 clusters. (d) $C = 0.001$: clustering results
47 in 70% clustered seismicity within 15 clusters.
48
49



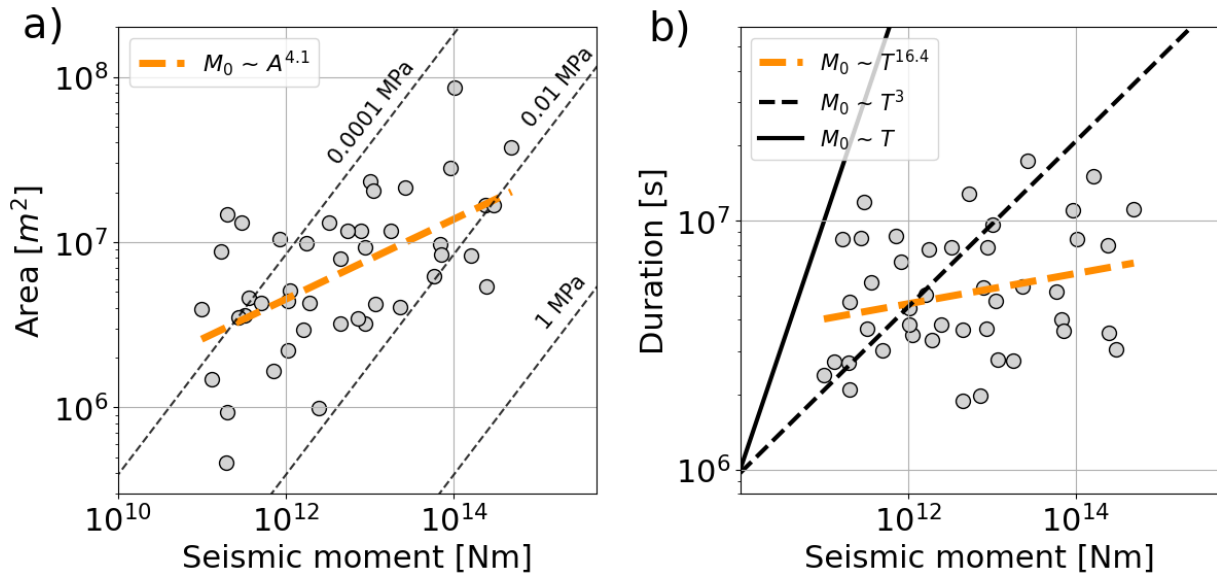
50
51
52
53
54

Figure S6: Distribution of the dip angle found for the extracted bursts of seismicity.



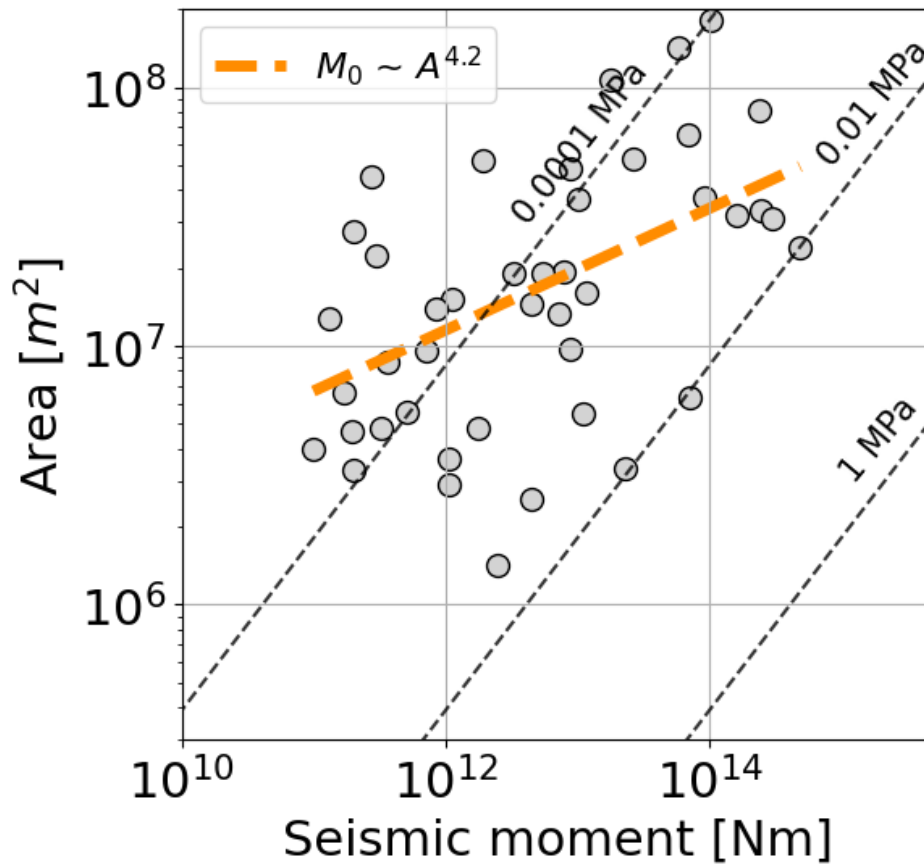
55
56
57
58

Figure S7: As figure 4b, but for the seismicity projected along the inferred fault planes.



59
60
61

Figure S8: As figure 5, only considering the measured seismic moment (M_0).



62
63
64
65
66
67
68
69
70
71
72
73

Figure S9: As figure 5a, but for the seismicity projected along the inferred fault planes.

Table S1: Outcome of different runs of HDBscan, with different gamma-noise added to the space features (v_{4_1} , $v_{4_1_a}$), and without the application of space noise. For the application without space noise, the C-parameter varies as it is dependent of the largest space distance.

Run	% of clustered seismicity	Nr cluster	C-parameter
v_{4_1}	38.32063426688633	44	0.018471633029548684
$v_{4_1_a}$	37.294069192751237	43	0.018905235680000002
$v_{4_}$ (no space scaling)	40.668039538715	30	0.0016905235680000002

74
75

Reference

76 Essing, D., & Poli, P. (2022). Spatiotemporal evolution of the Seismicity in the Alto Tiberina Fault
77 System revealed by a High-Resolution Template Matching Catalog. *Journal of Geophysical*
78 *Research: Solid Earth*, 127.

79 Piegari, E., Herrmann, M., & Marzocchi, W. (2022). 3-D spatial cluster analysis of seismic
80 sequences through density-based algorithms. *Geophysical Journal International*, 230(3), 2073-
81 2088.

82

83

Appendix C

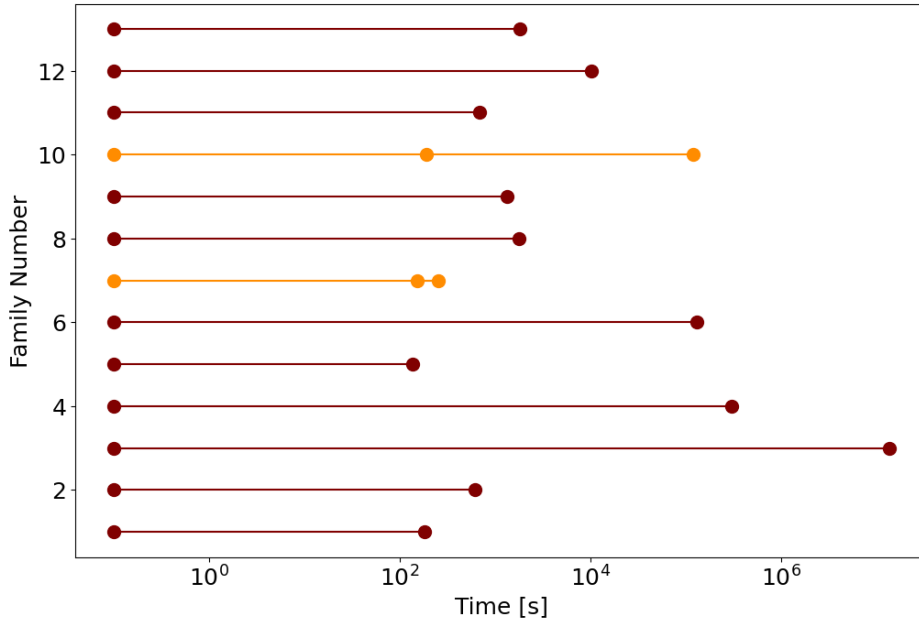
Supporting Information for Fast reoccurring, repeating earthquakes as a possible indication for fluid over-pressure¹

¹In preparation for submission in Geophysical Research Letters. Essing, D., & Poli, P. (2023). Fast reoccurring, repeating earthquakes as a possible indication for fluid over-pressure.

1 **Appendix**

2

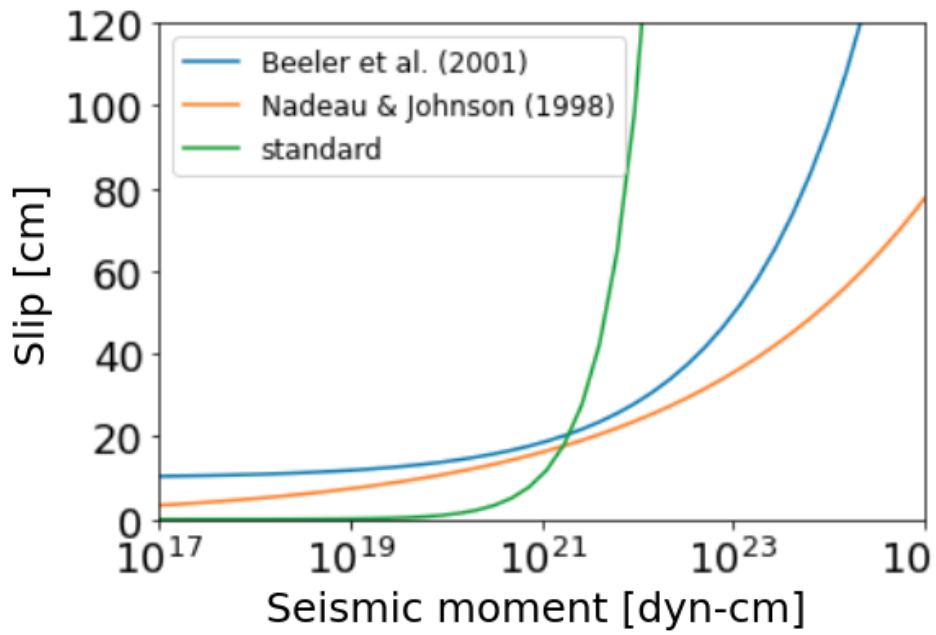
3



4

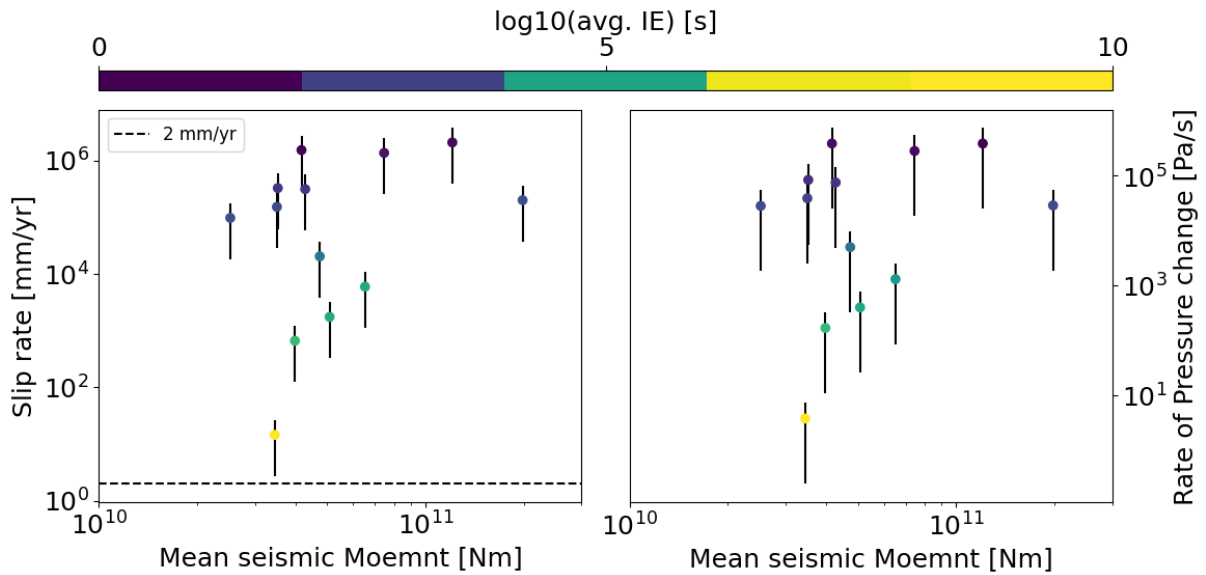
5 **Figure S1:** Times between consecutive events for each family of repeating earthquakes (REs).

6

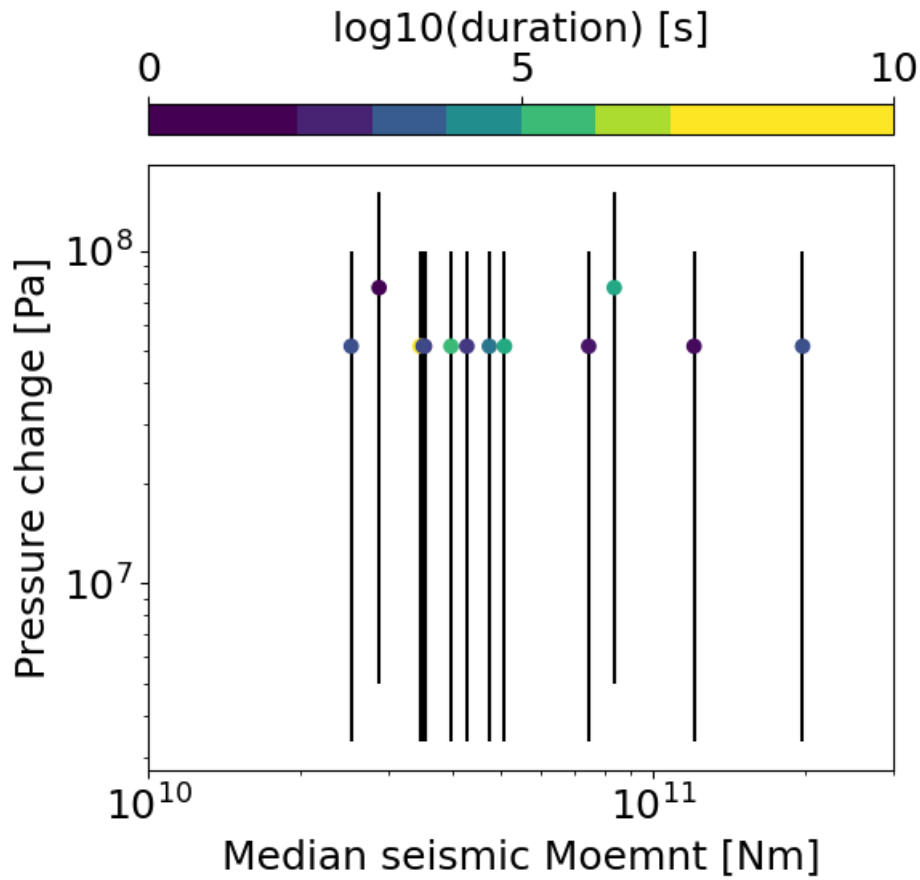


7

8 **Figure S2:** Slip for repeating earthquakes, as predicted by seismic moment following the
 9 introduced models (Uchida, 2019).



10
 11 **Figure S3:** (a) Slip rate as a function of mean seismic moment for the found families of repeating
 12 earthquakes (REs). Slip rates are estimated by the slip derived by the standard crack model
 13 (Schmittbuhl et al., 2016; Yao et al., 2017) divided by the average intervent-times of RE families.
 14 The horizontal dashed line indicates the annual extension of the study area (Anderlini et al., 2016).
 15 (b) Estimated rate of pressure change (Baisch & Harjes, 2003) as a function of mean seismic
 16 moment for each family of REs. The bars indicate the resulting range as we assume stress drops
 17 $\Delta\sigma$ from 1 to 30 MPa.



18

19 **Figure S4:** Pressure change (Baisch & Harjes, 2003) as a function of mean seismic moment for
 20 the found families of repeating earthquakes.

21

22 **Table S1:** Table showing events, within families with the duration, the estimated slip, the
 23 estimated seismic moment (M_0), the corner frequency (f_c) estimated using Brunes-model (Brune
 24 1970), f_c estimated using Boatwright-model (Boatwright 1980), the theoretical stress drop ($\Delta\sigma$)
 25 for slip of 2 mm/yr, and the theoretical f_c for slip of 2 mm/yr.

26

event nr	fam .	duration [s]	estima ted slip [mm]	estimate d M_0 [Nm]	estim ated f_c (Brun e) [Hz]	estima ted f_c (Boatw right) [Hz]	theo. $\Delta\sigma$ [MPa]	theo. f_c [Hz]
0	1	183	1.88	1.19E+11	35.03	16.41	1.62E-08	0.14
1	1	183	1.19	3.04E+10	35.90	21.48	3.21E-08	0.28
2	2	617	1.36	4.47E+10	35.23	20.74	1.64E-07	0.42
3	2	617	1.13	2.58E+10	30.19	18.61	2.16E-07	0.56
4	3	13778072	1.30	3.95E+10	38.13	22.48	5.82E-01	67.20

5	3	13778072	1.18	2.96E+10	35.53	21.30	6.72E-01	77.62
6	4	307666	1.50	6.04E+10	28.05	16.55	1.57E-03	8.12
7	4	307666	1.03	1.92E+10	27.61	16.53	2.78E-03	14.39
8	5	134	1.15	2.73E+10	35.19	20.80	2.12E-08	0.25
9	5	134	2.29	2.14E+11	33.80	19.46	7.58E-09	0.09
10	6	130003	1.53	6.40E+10	28.99	16.94	4.19E-04	5.12
11	6	130003	1.28	3.76E+10	36.86	21.94	5.47E-04	6.69
12	7	100	1.17	2.87E+10	26.66	16.20	7.27E-09	0.17
13	7	100	0.97	1.61E+10	23.28	14.21	9.69E-09	0.23
14	7	100	1.65	8.02E+10	26.08	15.66	4.34E-09	0.10
15	8	1798	2.08	1.61E+11	34.18	20.75	4.30E-07	0.38
16	8	1798	2.36	2.35E+11	33.34	20.66	3.55E-07	0.31
17	9	1332	1.24	3.41E+10	28.64	18.39	5.95E-07	0.71
18	9	1332	1.26	3.60E+10	27.22	17.53	5.79E-07	0.69
19	10	119197	1.68	8.38E+10	26.93	15.98	1.75E-04	3.50
20	10	119197	0.98	1.68E+10	19.61	12.17	3.90E-04	7.82
21	10	119197	1.75	9.50E+10	25.71	15.24	1.64E-04	3.29
22	11	687	1.45	5.39E+10	32.34	20.68	1.75E-07	0.41
23	11	687	1.21	3.16E+10	33.04	21.04	2.29E-07	0.53
24	12	10335	0.98	1.66E+10	30.58	18.85	1.84E-05	2.83
25	12	10335	1.64	7.82E+10	29.43	18.26	8.49E-06	1.31
26	13	1836	1.24	3.43E+10	36.03	22.10	9.61E-07	0.83
27	13	1836	0.97	1.62E+10	33.07	20.33	1.40E-06	1.21

27

28

References

29 Uchida, N. (2019). Detection of repeating earthquakes and their application in characterizing slow
30 fault slip. *Progress in Earth and Planetary Science*, 6(1), 1-21.

31

32

33

34

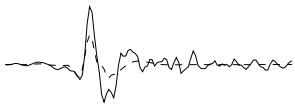
Appendix D

Supporting Information for Outlook and Conclusions

Tangential

Radial

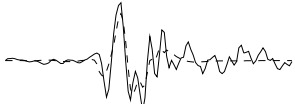
Vertical



TRTR_f0.05.data, Max Amp=3.13e-04 cm/s, VR=39.5, Azi=113, Dist=135.6, Zcor=111



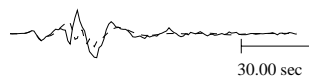
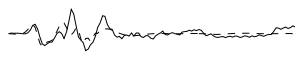
GUMA_f0.05.data, Max Amp=2.06e-04 cm/s, VR=31.3, Azi=108, Dist=81.2, Zcor=102



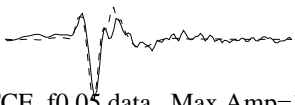
LPEL_f0.05.data, Max Amp=5.54e-05 cm/s, VR=36.3, Azi=133, Dist=202.2, Zcor=116



NARO_f0.05.data, Max Amp=2.65e-04 cm/s, VR=82.7, Azi=24, Dist=38.2, Zcor=96

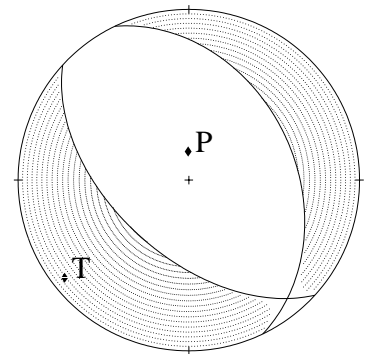


OSSC_f0.05.data, Max Amp=2.03e-04 cm/s, VR=66.2, Azi=286, Dist=96.0, Zcor=102



MTCE_f0.05.data, Max Amp=1.22e-04 cm/s, VR=54.9, Azi=168, Dist=144.5, Zcor=106

Depth =5 km
 Strike=132 ; 334
 Rake =-103 ; -72
 Dip =54 ; 38
 Mo =3.04e+22
 Mw =4.26
 Percent DC=97
 Percent CLVD=3
 Percent ISO=0
 Variance=3.08e-10
 Var. Red=6.08e+01
 RES/Pdc.=3.17e-12



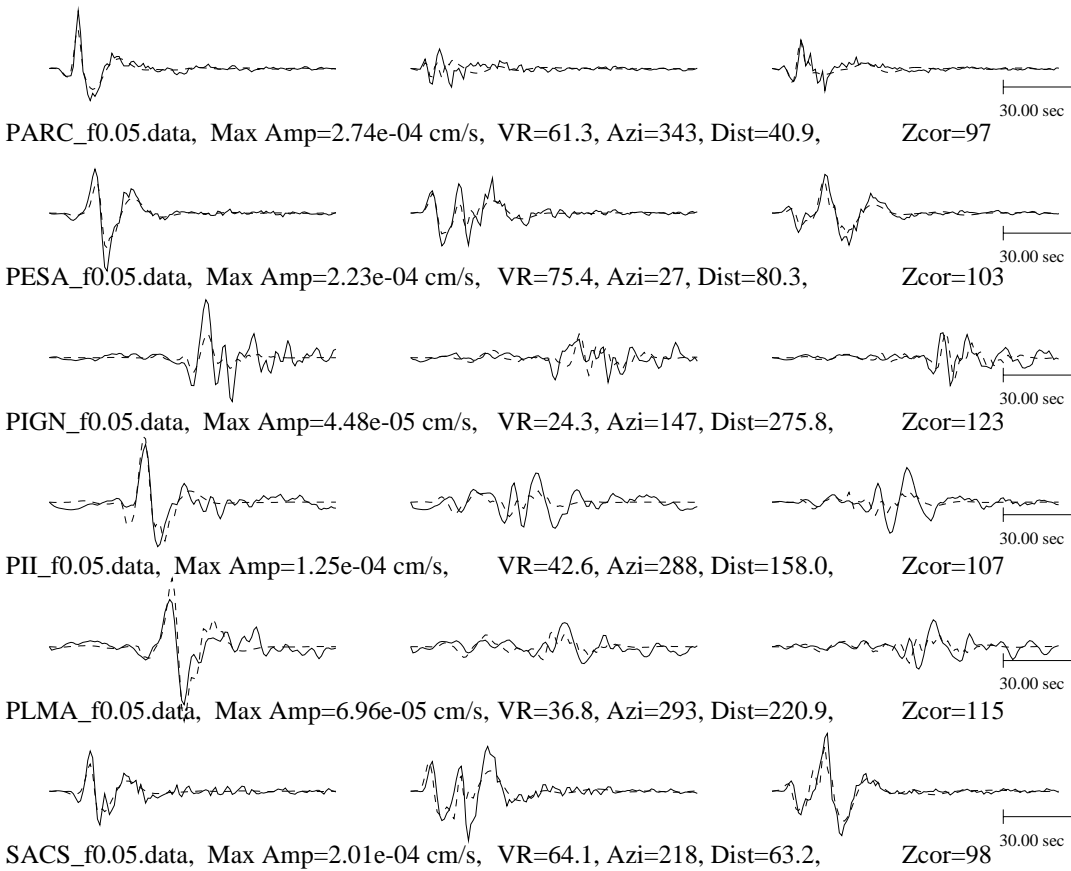
Mxx=9.54e+21 Myy=1.84e+22
 Mxy=1.48e+22 Myz=-3.32e+21
 Mxz=-9.52e+21 Mzz=-2.79e+22

Manually revised

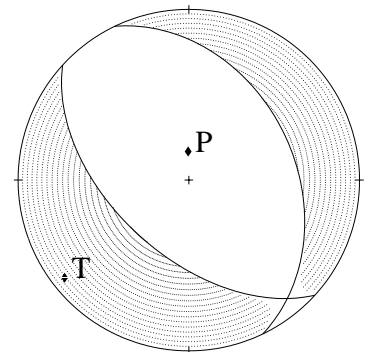
Tangential

Radial

Vertical



Depth =5 km
 Strike=132 ; 334
 Rake =-103 ; -72
 Dip =54 ; 38
 Mo =3.04e+22
 Mw =4.26
 Percent DC=97
 Percent CLVD=3
 Percent ISO=0
 Variance=3.08e-10
 Var. Red=6.08e+01
 RES/Pdc.=3.17e-12



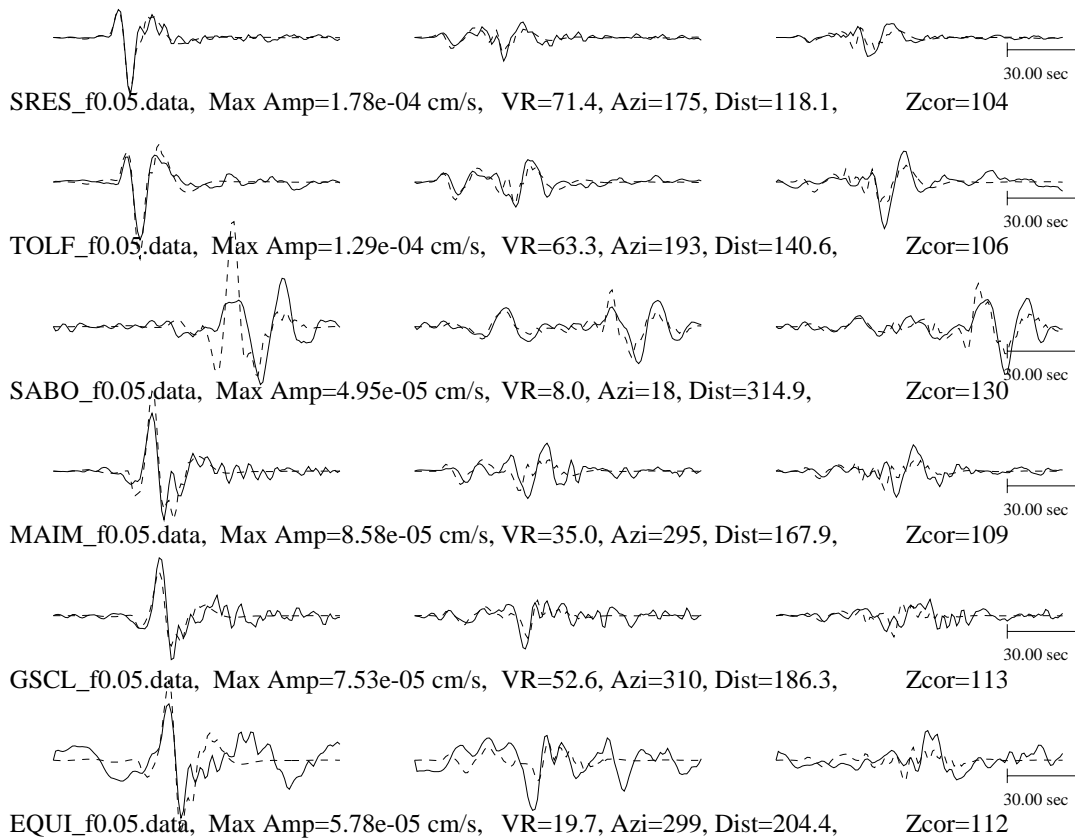
Mxx=9.54e+21 Myy=1.84e+22
 Mxy=1.48e+22 Myz=-3.32e+21
 Mxz=-9.52e+21 Mzz=-2.79e+22

Manually revised

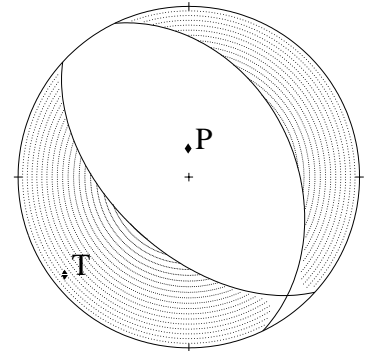
Tangential

Radial

Vertical



Depth =5 km
 Strike=132 ; 334
 Rake =-103 ; -72
 Dip =54 ; 38
 Mo =3.04e+22
 Mw =4.26
 Percent DC=97
 Percent CLVD=3
 Percent ISO=0
 Variance=3.08e-10
 Var. Red=6.08e+01
 RES/Pdc.=3.17e-12



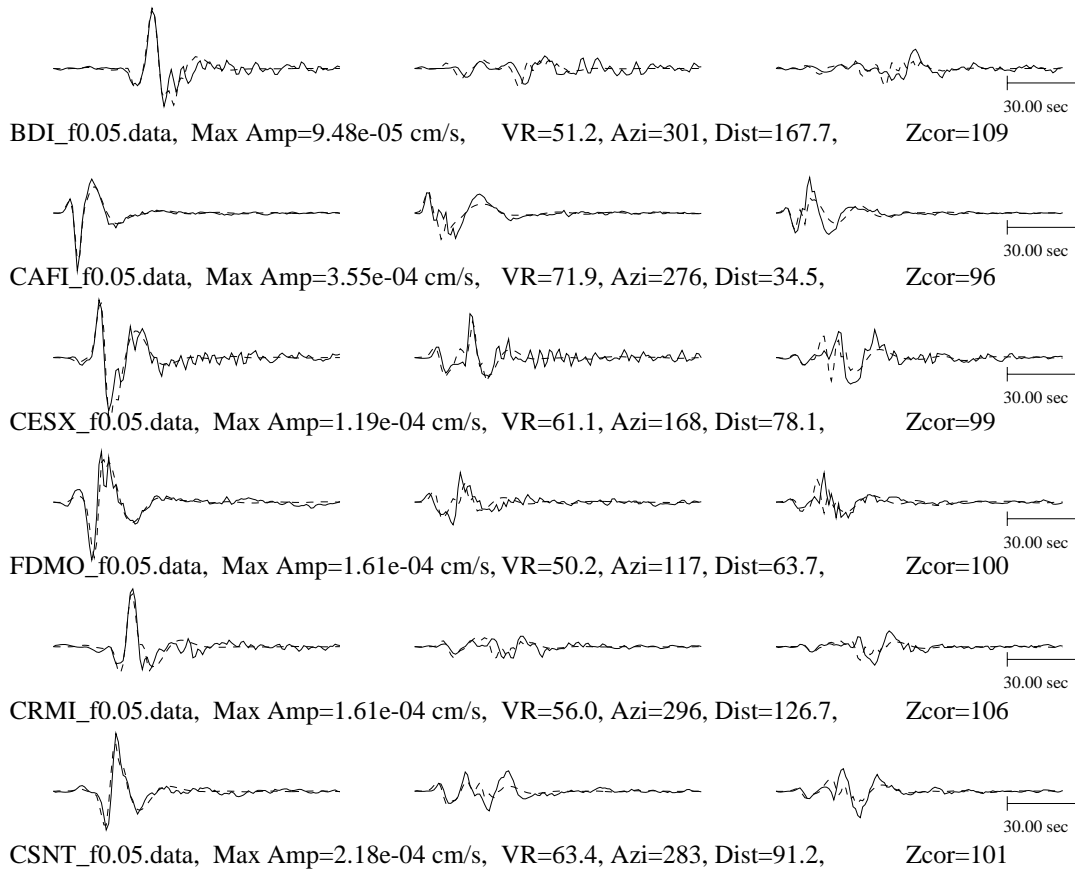
Mxx=9.54e+21 Myy=1.84e+22
 Mxy=1.48e+22 Myz=-3.32e+21
 Mxz=-9.52e+21 Mzz=-2.79e+22

Manually revised

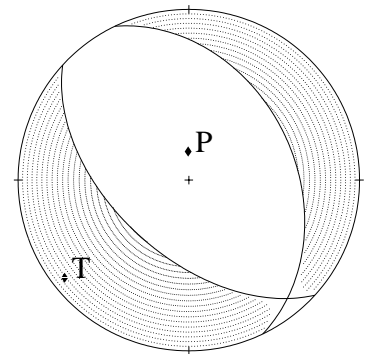
Tangential

Radial

Vertical



Depth =5 km
 Strike=132 ; 334
 Rake =-103 ; -72
 Dip =54 ; 38
 Mo =3.04e+22
 Mw =4.26
 Percent DC=97
 Percent CLVD=3
 Percent ISO=0
 Variance=3.08e-10
 Var. Red=6.08e+01
 RES/Pdc.=3.17e-12



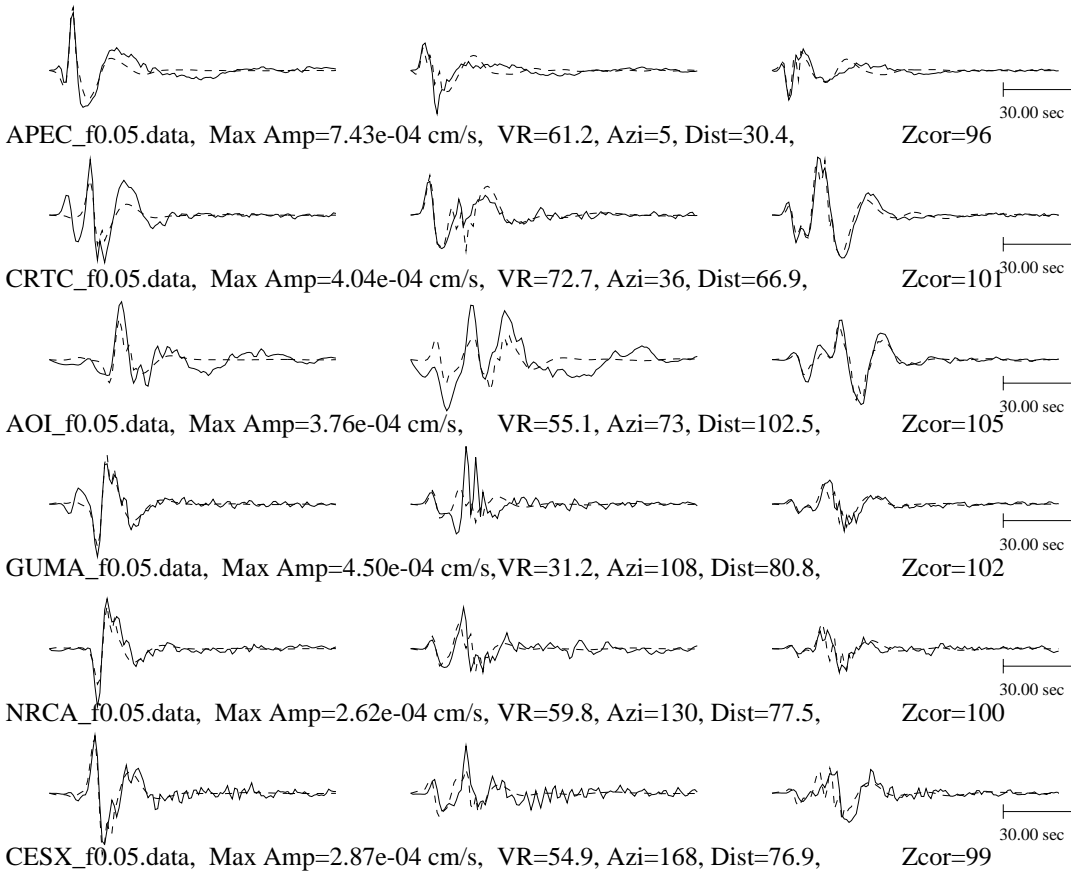
Mxx=9.54e+21 Myy=1.84e+22
 Mxy=1.48e+22 Myz=-3.32e+21
 Mxz=-9.52e+21 Mzz=-2.79e+22

Manually revised

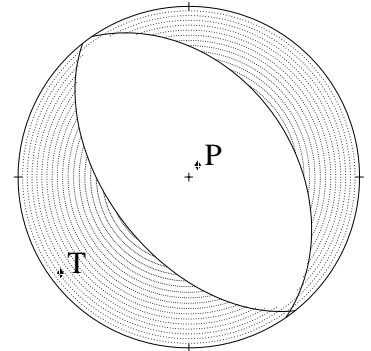
Tangential

Radial

Vertical



Depth =3 km
 Strike=142 ; 325
 Rake =-92 ; -87
 Dip =52 ; 38
 Mo =6.08e+22
 Mw =4.46
 Percent DC=98
 Percent CLVD=2
 Percent ISO=0
 Variance=2.04e-09
 Var. Red=5.83e+01
 RES/Pdc.=2.08e-11



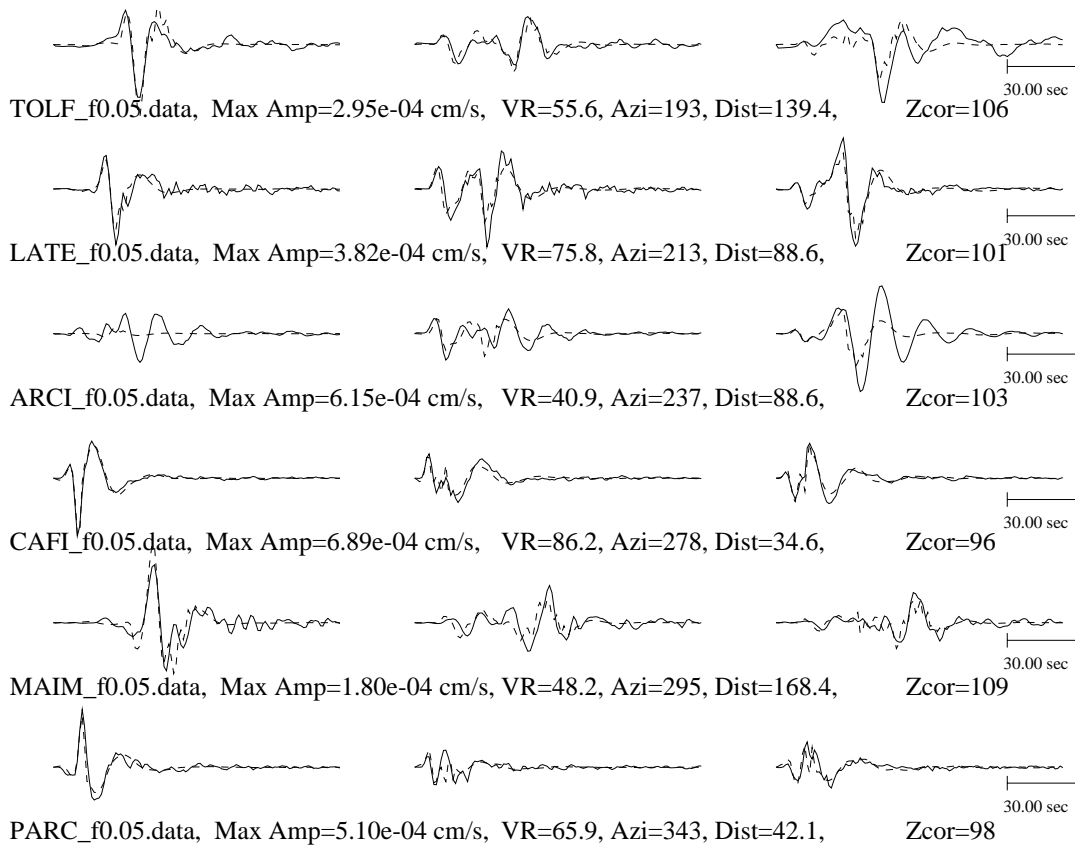
Mxx=2.12e+22 Myy=3.81e+22
 Mxy=2.79e+22 Myz=-1.01e+22
 Mxz=-1.01e+22 Mzz=-5.93e+22

Manually revised

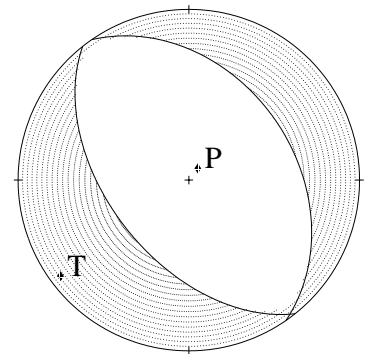
Tangential

Radial

Vertical



Depth =3 km
 Strike=142 ; 325
 Rake =-92 ; -87
 Dip =52 ; 38
 Mo =6.08e+22
 Mw =4.46
 Percent DC=98
 Percent CLVD=2
 Percent ISO=0
 Variance=2.04e-09
 Var. Red=5.83e+01
 RES/Pdc.=2.08e-11



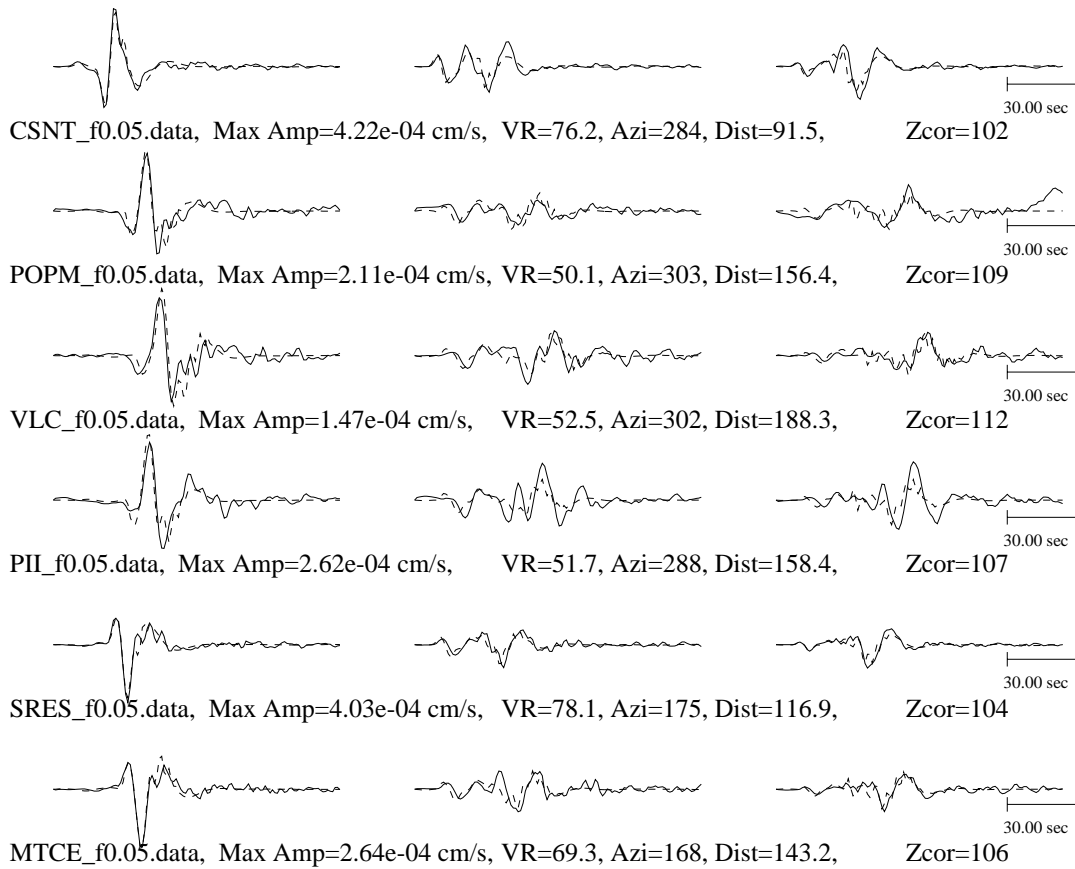
Mxx=2.12e+22 Myy=3.81e+22
 Mxy=2.79e+22 Myz=-1.01e+22
 Mxz=-1.01e+22 Mzz=-5.93e+22

Manually revised

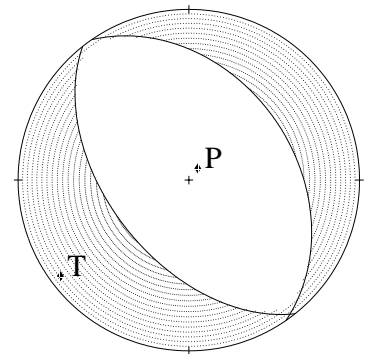
Tangential

Radial

Vertical



Depth =3 km
 Strike=142 ; 325
 Rake =-92 ; -87
 Dip =52 ; 38
 Mo =6.08e+22
 Mw =4.46
 Percent DC=98
 Percent CLVD=2
 Percent ISO=0
 Variance=2.04e-09
 Var. Red=5.83e+01
 RES/Pdc.=2.08e-11



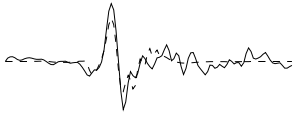
Mxx=2.12e+22 Myy=3.81e+22
 Mxy=2.79e+22 Myz=-1.01e+22
 Mxz=-1.01e+22 Mzz=-5.93e+22

Manually revised

Tangential

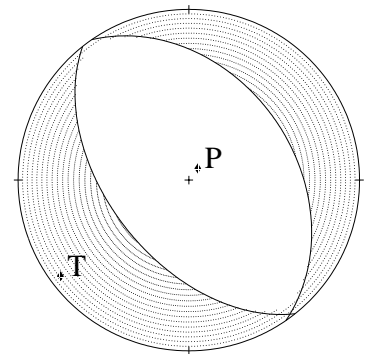
Radial

Vertical



GSCL_f0.05.data, Max Amp=1.60e-04 cm/s, VR=52.0, Azi=310, Dist=187.1, Zcor=114

Depth =3 km
Strike=142 ; 325
Rake =-92 ; -87
Dip =52 ; 38
Mo =6.08e+22
Mw =4.46
Percent DC=98
Percent CLVD=2
Percent ISO=0
Variance=2.04e-09
Var. Red=5.83e+01
RES/Pdc.=2.08e-11



Mxx=2.12e+22 Myy=3.81e+22
Mxy=2.79e+22 Myz=-1.01e+22
Mxz=-1.01e+22 Mzz=-5.93e+22

Manually revised

Bibliography

- Abercrombie, R. E. (1995). "Earthquake source scaling relationships from -1 to 5 seismograms recorded at 2.5-km depth". In: *Journal of Geophysical Research* 100.B12, pp. 24015–24036.
- Abercrombie, Rachel E. (2021). *Resolution and uncertainties in estimates of earthquake stress drop and energy release*. Vol. 379. 2196. ISBN: 0000000345. DOI: [10.1098/rsta.2020.0131](https://doi.org/10.1098/rsta.2020.0131).
- Abers, Geoffrey A, Carolyn Z Mutter, and Jia Fang (1997). "Shallow dips of normal faults during rapid extension: Earthquakes in the Woodlark-D'Entrecasteaux rift system, Papua New Guinea". In: *Journal of Geophysical Research: Solid Earth* 102.B7, pp. 15301–15317. ISSN: 2156-2202. DOI: [10.1029/97jb00787](https://doi.org/10.1029/97jb00787).
- Aden-Antoniów, F, WB Frank, and L Seydoux (2022). "An adaptable random forest model for the declustering of earthquake catalogs". In: *Journal of Geophysical Research: Solid Earth* 127.2, e2021JB023254.
- Aiken, C. and K. Obara (2021). "Data-Driven Clustering Reveals More Than 900 Small Magnitude Slow Earthquakes and Their Characteristics". In: *Geophysical Research Letters* 48.11, pp. 1–8. ISSN: 19448007. DOI: [10.1029/2020GL091764](https://doi.org/10.1029/2020GL091764).
- Anderlini, L, E Serpelloni, and M E Belardinelli (2016). "Creep and locking of a low-angle normal fault: Insights from the Altotiberina fault in the Northern Apennines (Italy)". In: *Geophysical Research Letters* 43.9, pp. 4321–4329. ISSN: 19448007. DOI: [10.1002/2016GL068604](https://doi.org/10.1002/2016GL068604).
- Anderson, R Ernest (1971). "Thin skin distension in Tertiary rocks of southeastern Nevada". In: *Geological Society of America Bulletin* 82.1, pp. 43–58.
- Anstey, Nigel Allister (1964). "Correlation techniques—a review". In: *Geophysical Prospecting* 12.4, pp. 355–382.
- Bachura, M et al. (2020). "From earthquake swarm to a mainshock-aftershocks: the 2018 activity in West Bohemia/Vogtland". In: *Geophysical Journal International*, pp. 1–30.
- Baiesi, Marco and Maya Paczuski (2004). "Scale-free networks of earthquakes and aftershocks". In: *Physical Review E - Statistical Physics, Plasmas, Fluids, and Related Interdisciplinary Topics* 69.6, p. 8. ISSN: 1063651X. DOI: [10.1103/PhysRevE.69.066106](https://doi.org/10.1103/PhysRevE.69.066106).
- Baisch, S. and H. P. Harjes (2003). "A model for fluid-injection-induced seismicity at the KTB, Germany". In: *Geophysical Journal International* 152.1, pp. 160–170. ISSN: 0956540X. DOI: [10.1046/j.1365-246X.2003.01837.x](https://doi.org/10.1046/j.1365-246X.2003.01837.x).
- Baisch, Stefan (2020). "Inferring In Situ Hydraulic Pressure From Induced Seismicity Observations: An Application to the Cooper Basin (Australia) Geothermal Reservoir". In: *Journal of Geophysical Research: Solid Earth* 125.8. ISSN: 21699356. DOI: [10.1029/2019JB019070](https://doi.org/10.1029/2019JB019070).
- Barchi, M (1998). "The CROP 03 profile: a synthesis of results on deep structures of the Northern Apennines". In: *Mem. Soc. Geol. It.* 52, pp. 383–400.
- Barchi, M et al. (2003). "Line CROP 03: Northern Apennines". In: *Mem. Descr. Carta Geol. d'It* 62, pp. 127–136.

- Báth, Markus (1965). "Lateral inhomogeneities of the upper mantle". In: *Tectonophysics* 2.6, pp. 483–514.
- Beaucé, Eric and William B Frank (2018). "Fast Matched Filter (FMF): An Efficient Seismic Matched-Filter Search for Both CPU and GPU Architectures". In: 89.1. DOI: [10.1785/0220170181](https://doi.org/10.1785/0220170181).
- Beaucé, Eric, Robert D van der Hilst, and Michel Campillo (2022). "Microseismic constraints on the mechanical state of the North Anatolian fault zone 13 years after the 1999 M7. 4 Izmit earthquake". In: *Journal of Geophysical Research: Solid Earth* 127.9, e2022JB024416.
- Beaucé, Eric et al. (2019). "Systematic Detection of Clustered Seismicity Beneath the Southwestern Alps". In: *Journal of Geophysical Research: Solid Earth*. ISSN: 21699356. DOI: [10.1029/2019JB018110](https://doi.org/10.1029/2019JB018110).
- Beeler, NM, DL Lockner, and SH Hickman (2001). "A simple stick-slip and creep-slip model for repeating earthquakes and its implication for microearthquakes at Parkfield". In: *Bulletin of the Seismological Society of America* 91.6, pp. 1797–1804.
- Biemiller, James et al. (2020). "Mechanical Implications of Creep and Partial Coupling on the World's Fastest Slipping Low-Angle Normal Fault in Southeastern Papua New Guinea". In: *Journal of Geophysical Research: Solid Earth* 125.10, pp. 1–24. ISSN: 21699356. DOI: [10.1029/2020JB020117](https://doi.org/10.1029/2020JB020117).
- Bjørnstad, Ottar N, Rolf A Ims, and Xavier Lambin (1999). "Spatial population dynamics: analyzing patterns and processes of population synchrony". In: *Trends in Ecology & Evolution* 14.11, pp. 427–432.
- Boatwright, John (1980). "A spectral theory for circular seismic sources; simple estimates of source dimension, dynamic stress drop, and radiated seismic energy". In: *Bulletin of the Seismological Society of America* 70.1, pp. 1–27.
- Boettcher, MS and TH Jordan (2004). "Earthquake scaling relations for mid-ocean ridge transform faults". In: *Journal of Geophysical Research: Solid Earth* 109.B12.
- Boncio, Paolo, Francesco Brozzetti, and Giusy Lavecchia (2000). "Architecture and seismotectonics of a regional low-angle normal fault zone in central Italy". In: *Tectonics* 19.6, pp. 1038–1055. ISSN: 02787407. DOI: [10.1029/2000TC900023](https://doi.org/10.1029/2000TC900023).
- Boschi, Enzo (1998). *I terremoti dell'Appennino umbro-marchigiano: area sud orientale dal 99 aC al 1984*. Editrice Compositori.
- Briole, Pierre et al. (2000). "Active deformation of the Corinth rift, Greece: results from repeated Global Positioning System surveys between 1990 and 1995". In: *Journal of Geophysical Research: Solid Earth* 105.B11, pp. 25605–25625.
- Brown, Justin R, Gregory C Beroza, and David R Shelly (2008). "An autocorrelation method to detect low frequency earthquakes within tremor". In: *Geophysical Research Letters* 35.16.
- Brune, James N (1970). "Tectonic stress and the spectra of seismic shear waves from earthquakes". In: *Journal of geophysical research* 75.26, pp. 4997–5009.
- Bürgmann, Roland et al. (2000). "Earthquake potential along the northern Hayward fault, California". In: *Science* 289.5482, pp. 1178–1182.
- Byerlee, J (1978). "Friction of Rocks". In: *Rock Friction and Earthquake Prediction*. Ed. by James D Byerlee and Max Wyss. Basel: Birkhäuser Basel, pp. 615–626. ISBN: 978-3-0348-7182-2. DOI: [10.1007/978-3-0348-7182-2_4](https://doi.org/10.1007/978-3-0348-7182-2_4). URL: https://doi.org/10.1007/978-3-0348-7182-2_4.
- Cabrera, Leoncio, Piero Poli, and William B. Frank (2022). "Tracking the Spatio-Temporal Evolution of Foreshocks Preceding the Mw 6.1 2009 L'Aquila Earthquake". In: *Journal of Geophysical Research: Solid Earth* 127.3, pp. 1–16. ISSN: 21699356. DOI: [10.1029/2021JB023888](https://doi.org/10.1029/2021JB023888).

- Campello, Ricardo JGB, Davoud Moulavi, and Jörg Sander (2013). "Density-based clustering based on hierarchical density estimates". In: *Advances in Knowledge Discovery and Data Mining: 17th Pacific-Asia Conference, PAKDD 2013, Gold Coast, Australia, April 14-17, 2013, Proceedings, Part II* 17. Springer, pp. 160–172.
- Cappa, Frédéric, Jonny Rutqvist, and Koji Yamamoto (2009). "Modeling crustal deformation and rupture processes related to upwelling of deep CO₂-rich fluids during the 1965–1967 Matsushiro earthquake swarm in Japan". In: *Journal of Geophysical Research: Solid Earth* 114.B10.
- Cattania, Camilla and Paul Segall (2021). "Precursory slow slip and foreshocks on rough faults". In: *Journal of Geophysical Research: Solid Earth* 126.4, e2020JB020430.
- Cesca, Simone (2020). "Seiscloud, a tool for density-based seismicity clustering and visualization". In: *Journal of Seismology* 24.3, pp. 443–457. ISSN: 1573157X. DOI: [10.1007/s10950-020-09921-8](https://doi.org/10.1007/s10950-020-09921-8).
- Chen, Kate Huihsuan, Robert M. Nadeau, and Ruey Juin Rau (2007). "Towards a universal rule on the recurrence interval scaling of repeating earthquakes?" In: *Geophysical Research Letters* 34.16, pp. 1–5. ISSN: 00948276. DOI: [10.1029/2007GL030554](https://doi.org/10.1029/2007GL030554).
- Chen, Kate Huihsuan, Robert M Nadeau, and Ruey-Juin Rau (2008). "Characteristic repeating earthquakes in an arc-continent collision boundary zone: The Chihshang fault of eastern Taiwan". In: *Earth and Planetary Science Letters* 276.3-4, pp. 262–272.
- Chen, Kate Huihsuan, Roland Bürgmann, and Robert M Nadeau (2013). "Do earthquakes talk to each other? Triggering and interaction of repeating sequences at Parkfield". In: *Journal of Geophysical Research: Solid Earth* 118.1, pp. 165–182.
- Chen, X. and P. M. Shearer (2011). "Comprehensive analysis of earthquake source spectra and swarms in the Salton Trough, California". In: *Journal of Geophysical Research: Solid Earth* 116.9, pp. 1–17. ISSN: 21699356. DOI: [10.1029/2011JB008263](https://doi.org/10.1029/2011JB008263).
- Chen, Xiaowei et al. (2017). "The Pawnee earthquake as a result of the interplay among injection, faults and foreshocks". In: *Scientific Reports* 7.1, pp. 1–18.
- Chiarabba, C and A Amato (2003). "Vp and Vp/Vs images in the Mw 6.0 Colfiorito fault region (central Italy): A contribution to the understanding of seismotectonic and seismogenic processes". In: *Journal of Geophysical Research: Solid Earth* 108.B5.
- Chiaraluce, L et al. (2007). "Architecture and mechanics of an active low-angle normal fault: Alto Tiberina Fault, northern Apennines, Italy". In: *Journal of Geophysical Research: Solid Earth* 112.10. ISSN: 21699356. DOI: [10.1029/2007JB005015](https://doi.org/10.1029/2007JB005015).
- Chiaraluce, L et al. (2011). "The anatomy of the 2009 L'Aquila normal fault system (central Italy) imaged by high resolution foreshock and aftershock locations". In: *Journal of Geophysical Research: Solid Earth* 116.B12.
- Chiaraluce, Lauro et al. (2014). "The alto Tiberina near fault observatory (northern Apennines, Italy)". In: *Annals of Geophysics* 57.3. ISSN: 15935213. DOI: [10.4401/ag-6426](https://doi.org/10.4401/ag-6426).
- Chiaraluce, Lauro et al. (2017). "The 2016 central Italy seismic sequence: A first look at the mainshocks, aftershocks, and source models". In: *Seismological Research Letters* 88.3, pp. 757–771.
- Chiodini, G et al. (2000). "Rate of diffuse carbon dioxide Earth degassing estimated from carbon balance of regional aquifers: The case of central Apennine, Italy". In: *Journal of Geophysical Research: Solid Earth* 105.B4, pp. 8423–8434.
- Chiodini, G et al. (2004). "Carbon dioxide Earth degassing and seismogenesis in central and southern Italy". In: *Geophysical Research Letters* 31.7, pp. 2–5. ISSN: 00948276. DOI: [10.1029/2004GL019480](https://doi.org/10.1029/2004GL019480).

- Chiodini, Giovanni and Roberto Cioni (1989). "Gas geobarometry for hydrothermal systems and its application to some Italian geothermal areas". In: *Applied geochemistry* 4.5, pp. 465–472.
- Cianetti, S. et al. (2008). "Modelling deformation rates in the western Gulf of Corinth: Rheological constraints". In: *Geophysical Journal International* 174.2, pp. 749–757. ISSN: 0956540X. DOI: [10.1111/j.1365-246X.2008.03845.x](https://doi.org/10.1111/j.1365-246X.2008.03845.x).
- Cochran, Elizabeth S. et al. (2018). "Induced Earthquake Families Reveal Distinctive Evolutionary Patterns Near Disposal Wells". In: *Journal of Geophysical Research: Solid Earth* 123.9, pp. 8045–8055. ISSN: 21699356. DOI: [10.1029/2018JB016270](https://doi.org/10.1029/2018JB016270).
- Collettini, C., N. De Paola, and N. R. Gouly (2006). "Switches in the minimum compressive stress direction induced by overpressure beneath a low-permeability fault zone". In: *Terra Nova* 18.3, pp. 224–231. ISSN: 09544879. DOI: [10.1111/j.1365-3121.2006.00683.x](https://doi.org/10.1111/j.1365-3121.2006.00683.x).
- Collettini, C. and R. E. Holdsworth (2004). "Fault zone weakening and character of slip along low-angle normal faults: Insights from the Zuccale fault, Elba, Italy". In: *Journal of the Geological Society* 161.6, pp. 1039–1051. ISSN: 00167649. DOI: [10.1144/0016-764903-179](https://doi.org/10.1144/0016-764903-179).
- Collettini, C et al. (2003). "The Gubbio fault: Can different methods give pictures of the same object?" In: *Journal of Geodynamics* 36.1-2, pp. 51–66. ISSN: 02643707. DOI: [10.1016/S0264-3707\(03\)00038-3](https://doi.org/10.1016/S0264-3707(03)00038-3).
- Collettini, Cristiano (2003). "Hypothesis for the mechanics and seismic behaviour of low-angle normal faults: The example of the Altotiberina fault Northern Apennines". In: *Annals of Geophysics* 45.5, pp. 683–698. ISSN: 03652556. DOI: [10.4401/ag-3531](https://doi.org/10.4401/ag-3531).
- (2011). "The mechanical paradox of low-angle normal faults: Current understanding and open questions". In: *Tectonophysics* 510.3-4, pp. 253–268. ISSN: 00401951. DOI: [10.1016/j.tecto.2011.07.015](https://doi.org/10.1016/j.tecto.2011.07.015). URL: <http://dx.doi.org/10.1016/j.tecto.2011.07.015>.
- Collettini, Cristiano and Massimiliano R Barchi (2002). "A low-angle normal fault in the Umbria region (Central Italy): A mechanical model for the related microseismicity". In: *Tectonophysics* 359.1-2, pp. 97–115. ISSN: 00401951. DOI: [10.1016/S0040-1951\(02\)00441-9](https://doi.org/10.1016/S0040-1951(02)00441-9).
- Collettini, Cristiano and Richard H Sibson (2001). "Normal faults, normal friction?" In: *Geology* 29.10, pp. 927–930.
- Collettini, Cristiano et al. (2002). "Hypothesis for the mechanics and seismic behaviour of low-angle normal faults: the example of the Altotiberina fault Northern Apennines". In: *Annals of Geophysics*.
- Collettini, Cristiano et al. (2011). "Fault structure, frictional properties and mixed-mode fault slip behavior". In: *Earth and Planetary Science Letters* 311.3-4, pp. 316–327. ISSN: 0012821X. DOI: [10.1016/j.epsl.2011.09.020](https://doi.org/10.1016/j.epsl.2011.09.020). URL: <http://dx.doi.org/10.1016/j.epsl.2011.09.020>.
- Cormack, Richard M (1971). "A review of classification". In: *Journal of the Royal Statistical Society: Series A (General)* 134.3, pp. 321–353.
- Danré, Philippe, Louis De Barros, and Frédéric Cappa (2022). "Inferring fluid volume during earthquake swarms using seismic catalogues". In: *Geophysical Journal International* 232.2, pp. 829–841. ISSN: 0956-540X. DOI: [10.1093/gji/ggac345](https://doi.org/10.1093/gji/ggac345).
- Danré, Philippe et al. (2022). "Prevalence of aseismic slip linking fluid injection to natural and anthropogenic seismic swarms". In: *Journal of Geophysical Research: Solid Earth*, e2022JB025571.

- Davis, Gregory A, Gordon S Lister, and Stephen J Reynolds (1986). "Structural evolution of the Whipple and South Mountains shear zones, southwestern United States". In: *Geology* 14.1, pp. 7–10.
- Davis, Scott D. and Cliff Frohlich (1991). "Single-Link Cluster Analysis, Synthetic Earthquake Catalogues, and Aftershock Identification". In: *Geophysical Journal International* 104.2, pp. 289–306. ISSN: 1365246X. DOI: [10.1111/j.1365-246X.1991.tb02512.x](https://doi.org/10.1111/j.1365-246X.1991.tb02512.x).
- De Barros, Louis et al. (2020). "Imbricated Aseismic Slip and Fluid Diffusion Drive a Seismic Swarm in the Corinth Gulf, Greece". In: *Geophysical Research Letters* 47.9, pp. 1–9. ISSN: 19448007. DOI: [10.1029/2020GL087142](https://doi.org/10.1029/2020GL087142).
- De Barros, Louis et al. (2021). "Migration of Fluid-Induced Seismicity Reveals the Seismogenic State of Faults". In: *Journal of Geophysical Research: Solid Earth* 126.11, e2021JB022767.
- Deschamps, A, R Scarpa, and G Selvaggi (1989). "Analisi sismologica del settore settentrionale dell'Appennino umbro-marchigiano". In: *Atti GNGTS 8th Conference*. Vol. 1, pp. 9–15.
- Di Bucci, Daniela and Stefano Mazzoli (2002). "Active tectonics of the Northern Apennines and Adria geodynamics: new data and a discussion". In: *Journal of Geodynamics* 34.5, pp. 687–707.
- Dieterich, James H (1979). "Modeling of rock friction: 1. Experimental results and constitutive equations". In: *Journal of Geophysical Research: Solid Earth* 84.B5, pp. 2161–2168.
- Dublanchet, P and L De Barros (2021). "Dual Seismic Migration Velocities in Seismic Swarms". In: *Geophysical Research Letters* 48.1, pp. 1–10. ISSN: 19448007. DOI: [10.1029/2020GL090025](https://doi.org/10.1029/2020GL090025).
- Dublanchet, Pierre, Pascal Bernard, and Pascal Favreau (2013). "Interactions and triggering in a 3-D rate-and-state asperity model". In: *Journal of Geophysical Research: Solid Earth* 118.5, pp. 2225–2245.
- Duverger, C. et al. (2018). "Dynamics of microseismicity and its relationship with the active structures in the western Corinth Rift (Greece)". In: *Geophysical Journal International* 215.1, pp. 196–221. ISSN: 1365246X. DOI: [10.1093/gji/ggy264](https://doi.org/10.1093/gji/ggy264).
- Dziewonski, A.M., J.E. Franzen, and J.H. Woodhouse (1985). "Centroid-moment tensor solutions for April–June, 1984". In: *Physics of the Earth and Planetary Interiors* 37.2, pp. 87–96. ISSN: 0031-9201. DOI: [https://doi.org/10.1016/0031-9201\(85\)90043-3](https://doi.org/10.1016/0031-9201(85)90043-3). URL: <https://www.sciencedirect.com/science/article/pii/0031920185900433>.
- Eldridge, Justin, Mikhail Belkin, and Yusu Wang (2015). "Beyond hartigan consistency: Merge distortion metric for hierarchical clustering". In: *Conference on Learning Theory*. PMLR, pp. 588–606.
- Ellsworth, William L and Lynn D Dietz (1990). "Repeating earthquakes: Characteristics and implications". In: *Proceedings of Workshop XLVI, the 7th US-Japan Seminar on Earthquake Prediction, US Geol. Surv. Open File Rep. 90*. Vol. 98, pp. 226–245.
- Elst, Nicholas J Van der et al. (2016). "Induced earthquake magnitudes are as large as (statistically) expected". In: *Journal of Geophysical Research: Solid Earth* 121.6, pp. 4575–4590.
- Eshelby, John Douglas (1957). "The determination of the elastic field of an ellipsoidal inclusion, and related problems". In: *Proceedings of the royal society of London. Series A. Mathematical and physical sciences* 241.1226, pp. 376–396.
- Essing, David and Piero Poli (2022). "Spatiotemporal Evolution of the Seismicity in the Alto Tiberina Fault System Revealed by a High-Resolution Template Matching Catalog". In: *Journal of Geophysical Research: Solid Earth* 127.10, e2022JB024845.

- Ester, Martin et al. (1996). "A density-based algorithm for discovering clusters in large spatial databases with noise." In: *kdd*. Vol. 96. 34, pp. 226–231.
- Fagereng, Åke and Richard H. Sibson (2010). "Mélange rheology and seismic style". In: *Geology* 38.8, pp. 751–754. ISSN: 00917613. DOI: [10.1130/G30868.1](https://doi.org/10.1130/G30868.1).
- Fattahi, H et al. (2015). "Coseismic and postseismic deformation due to the 2007 M5.5 Ghazaband fault earthquake, Balochistan, Pakistan". In: *Geophysical Research Letters* 42.9, pp. 3305–3312.
- Felzer, Karen R et al. (2002). "Triggering of the 1999 Mw 7.1 Hector Mine earthquake by aftershocks of the 1992 Mw 7.3 Landers earthquake". In: *Journal of Geophysical Research: Solid Earth* 107.B9, ESE–6.
- Fischer, T. et al. (2014). "Intra-continental earthquake swarms in West-Bohemia and Vogtland: A review". In: *Tectonophysics* 611, pp. 1–27. ISSN: 00401951. DOI: [10.1016/j.tecto.2013.11.001](https://doi.org/10.1016/j.tecto.2013.11.001).
- Fischer, Tomáš and Sebastian Hainzl (2017). "Effective stress drop of earthquake clusters". In: *Bulletin of the Seismological Society of America* 107.5, pp. 2247–2257. ISSN: 19433573. DOI: [10.1785/0120170035](https://doi.org/10.1785/0120170035).
- Frank, William B, Piero Poli, and Hugo Perfettini (2017). "Mapping the rheology of the Central Chile subduction zone with aftershocks". In: *Geophysical Research Letters* 44.11, pp. 5374–5382.
- Frank, William B et al. (2016). "The evolving interaction of low-frequency earthquakes during transient slip". In: *Science Advances* 2.4, pp. 1–8. ISSN: 23752548. DOI: [10.1126/sciadv.1501616](https://doi.org/10.1126/sciadv.1501616).
- Freed, Andrew M. (2005). "Earthquake triggering by static, dynamic, and postseismic stress transfer". In: *Annual Review of Earth and Planetary Sciences* 33.October 1999, pp. 335–367. ISSN: 00846597. DOI: [10.1146/annurev.earth.33.092203.122505](https://doi.org/10.1146/annurev.earth.33.092203.122505).
- Freiberger, Walter F (1963). "An approximate method in signal detection". In: *Quarterly of Applied Mathematics* 20.4, pp. 373–378.
- Frepoli, A and A Amato (1997). "Contemporaneous extension and compression in the Northern Apennines from earthquake fault-plane solutions". In: *Geophysical Journal International* 129.2, pp. 368–388.
- Frohlich, Cliff and Scott D. Davis (1990). "Single-Link Cluster Analysis As A Method to Evaluate Spatial and Temporal Properties of Earthquake Catalogues". In: *Geophysical Journal International* 100.1, pp. 19–32. ISSN: 1365246X. DOI: [10.1111/j.1365-246X.1990.tb04564.x](https://doi.org/10.1111/j.1365-246X.1990.tb04564.x).
- Gao, Haiying, David A. Schmidt, and Ray J. Weldon (2012). "Scaling relationships of source parameters for slow slip events". In: *Bulletin of the Seismological Society of America* 102.1, pp. 352–360. ISSN: 00371106. DOI: [10.1785/0120110096](https://doi.org/10.1785/0120110096).
- Gardner, JK and Leon Knopoff (1974). "Is the sequence of earthquakes in Southern California, with aftershocks removed, Poissonian?" In: *Bulletin of the seismological society of America* 64.5, pp. 1363–1367.
- Gibbons, SJ and F Ringdal (2004). "A waveform correlation procedure for detecting decoupled chemical explosions". In: *NORSAR Scientific Report: Semiannual Technical Summary 2-2004*, pp. 41–50.
- Gibbons, Steven J and Frode Ringdal (2006). "The detection of low magnitude seismic events using array-based waveform correlation". In: *Geophysical Journal International* 165.1, pp. 149–166. ISSN: 0956540X. DOI: [10.1111/j.1365-246X.2006.02865.x](https://doi.org/10.1111/j.1365-246X.2006.02865.x).
- Goebel, Thomas HW et al. (2016). "Wastewater disposal and earthquake swarm activity at the southern end of the Central Valley, California". In: *Geophysical Research Letters* 43.3, pp. 1092–1099.

- Gu, Ji-Cheng et al. (1984). "Slip motion and stability of a single degree of freedom elastic system with rate and state dependent friction". In: *Journal of the Mechanics and Physics of Solids* 32.3, pp. 167–196.
- Gualandi, A et al. (2017). "Aseismic deformation associated with an earthquake swarm in the northern Apennines (Italy)". In: *Geophysical Research Letters* 44.15, pp. 7706–7714. ISSN: 19448007. DOI: [10.1002/2017GL073687](https://doi.org/10.1002/2017GL073687).
- Guglielmi, Yves et al. (2015). "Seismicity triggered by fluid injection–induced aseismic slip". In: *Science* 348.6240, pp. 1224–1226.
- Gulia, Laura and Paolo Gasperini (2021). "Contamination of Frequency–Magnitude Slope (b-Value) by Quarry Blasts: An Example for Italy". In: *Seismological Research Letters* 92.6, pp. 3538–3551.
- Haessler, H et al. (1988). "The Perugia (Italy) earthquake of 29, April 1984: a microearthquake survey". In: *Bulletin of the Seismological Society of America* 78.6, pp. 1948–1964.
- Hainzl, Sebastian (2004). "Seismicity patterns of earthquake swarms due to fluid intrusion and stress triggering". In: *Geophysical Journal International* 159.3, pp. 1090–1096.
- Hainzl, Sebastian, Tomas Fischer, and Torsten Dahm (2012). "Seismicity-based estimation of the driving fluid pressure in the case of swarm activity in Western Bohemia". In: *Geophysical Journal International* 191.1, pp. 271–281.
- Hainzl, Sebastian and Yosihiko Ogata (2005). "Detecting fluid signals in seismicity data through statistical earthquake modeling". In: *Journal of Geophysical Research: Solid Earth* 110.5, pp. 1–10. ISSN: 21699356. DOI: [10.1029/2004JB003247](https://doi.org/10.1029/2004JB003247).
- Hayman, Nicholas W (2006). "Shallow crustal fault rocks from the Black Mountain detachments, Death Valley, CA". In: *Journal of Structural Geology* 28.10, pp. 1767–1784.
- Helmstetter, Agnes, Yan Y Kagan, and David D Jackson (2005). "Importance of small earthquakes for stress transfers and earthquake triggering". In: *Journal of Geophysical Research: Solid Earth* 110.B5.
- Helmstetter, Agnes and Didier Sornette (2002). "Subcritical and supercritical regimes in epidemic models of earthquake aftershocks". In: *Journal of Geophysical Research: Solid Earth* 107.B10, ESE–10.
- Herrmann, Marcus and Warner Marzocchi (2021). "Inconsistencies and Lurking Pitfalls in the Magnitude–Frequency Distribution of High-Resolution Earthquake Catalogs". In: *Seismological Research Letters* 92.2A, pp. 909–922. ISSN: 0895-0695. DOI: [10.1785/0220200337](https://doi.org/10.1785/0220200337).
- Hill, David P (1977). "A Model for Earthquake Swarms stress". In: *J Geophys. Res.* 82.8, pp. 1347–1352.
- Hirose, Hitoshi and Kazushige Obara (2006). "Short-term slow slip and correlated tremor episodes in the Tokai region, central Japan". In: *Geophysical Research Letters* 33.17.
- Hirose, Hitoshi et al. (2014). "The Boso slow slip events in 2007 and 2011 as a driving process for the accompanying earthquake swarm". In: *Geophysical Research Letters* 41.8, pp. 2778–2785.
- Hreinsdóttir, Sigrún and Richard A Bennett (2009). "Active aseismic creep on the Alto Tiberina low-angle normal fault, Italy". In: *Geology* 37.8, pp. 683–686. ISSN: 00917613. DOI: [10.1130/G30194A.1](https://doi.org/10.1130/G30194A.1).
- Ide, Satoshi et al. (2007). "A scaling law for slow earthquakes". In: *Nature* 447.7140, pp. 76–79.

- Igarashi, Toshihiro, Toru Matsuzawa, and Akira Hasegawa (2003). "Repeating earthquakes and interplate aseismic slip in the northeastern Japan subduction zone". In: *Journal of Geophysical Research: Solid Earth* 108.B5.
- Jolivet, Laurent et al. (1998). "Midcrustal shear zones in postorogenic extension: example from the northern Tyrrhenian Sea". In: *Journal of Geophysical Research: Solid Earth* 103.B6, pp. 12123–12160.
- Jolivet, Laurent et al. (2010). "The north cycladic detachment system". In: *Earth and Planetary Science Letters* 289.1-2, pp. 87–104.
- Jolivet, R and W B Frank (2020). "The Transient and Intermittent Nature of Slow Slip". In: *AGU Advances* 1.1. ISSN: 2576-604X. DOI: [10.1029/2019av000126](https://doi.org/10.1029/2019av000126).
- Kagan, Yan Y and David D Jackson (1991). "Long-Term Earthquake Clustering". In: *Geophysical Journal International* 104.1, pp. 117–134. ISSN: 1365246X. DOI: [10.1111/j.1365-246X.1991.tb02498.x](https://doi.org/10.1111/j.1365-246X.1991.tb02498.x).
- Kanamori, Hiroo (1977). "The energy release in great earthquakes". In: *Journal of geophysical research* 82.20, pp. 2981–2987.
- Kato, Aitaro et al. (2012). "Propagation of slow slip leading up to the 2011 M w 9.0 Tohoku-Oki earthquake". In: *Science* 335.6069, pp. 705–708.
- Knett, Joseph (1899). *Das erzgebirgische Schwarmbeben zu Hartenberg vom 1. Jänner bis 5. Feber 1824*. Mercy.
- Kwiatek, Grzegorz et al. (2019). "Controlling fluid-induced seismicity during a 6.1-km-deep geothermal stimulation in Finland". In: *Science Advances* 5.5, eaav7224.
- Küperkoch, L. et al. (May 2010). "Automated determination of P-phase arrival times at regional and local distances using higher order statistics". In: *Geophysical Journal International* 181.2, pp. 1159–1170. ISSN: 0956-540X. DOI: [10.1111/j.1365-246X.2010.04570.x](https://doi.org/10.1111/j.1365-246X.2010.04570.x). eprint: <https://academic.oup.com/gji/article-pdf/181/2/1159/1912611/181-2-1159.pdf>. URL: <https://doi.org/10.1111/j.1365-246X.2010.04570.x>.
- Lambotte, S. et al. (2014). "Reassessment of the rifting process in the Western Corinth Rift from relocated seismicity". In: *Geophysical Journal International* 197.3, pp. 1822–1844. ISSN: 1365246X. DOI: [10.1093/gji/ggu096](https://doi.org/10.1093/gji/ggu096).
- Latorre, D et al. (2016). "Assessment of earthquake locations in 3-D deterministic velocity models: A case study from the Altotiberina Near Fault Observatory (Italy)". In: *Journal of Geophysical Research: Solid Earth* 121.11, pp. 8113–8135. ISSN: 21699356. DOI: [10.1002/2016JB013170](https://doi.org/10.1002/2016JB013170).
- Latorre, Diana et al. (2014). "Man-induced low-frequency seismic events in Italy". In: *Geophysical Research Letters* 41.23, pp. 8261–8268. ISSN: 19448007. DOI: [10.1002/2014GL062044](https://doi.org/10.1002/2014GL062044).
- Le Pourhiet, Laetitia, Evgenii Burov, and Isabelle Moretti (2003). "Initial crustal thickness geometry controls on the extension in a back arc domain: Case of the Gulf of Corinth". In: *Tectonics* 22.4. ISSN: 02787407. DOI: [10.1029/2002TC001433](https://doi.org/10.1029/2002TC001433).
- Lengliné, O and D Marsan (2009). "Inferring the coseismic and postseismic stress changes caused by the 2004 Mw = 6 Parkfield earthquake from variations of recurrence times of microearthquakes". In: *Journal of Geophysical Research: Solid Earth* 114.10, pp. 1–19. ISSN: 21699356. DOI: [10.1029/2008JB006118](https://doi.org/10.1029/2008JB006118).
- Lengliné, O. et al. (2017). "Imbricated slip rate processes during slow slip transients imaged by low-frequency earthquakes". In: *Earth and Planetary Science Letters* 476, pp. 122–131. ISSN: 0012821X. DOI: [10.1016/j.epsl.2017.07.032](https://doi.org/10.1016/j.epsl.2017.07.032). URL: <http://dx.doi.org/10.1016/j.epsl.2017.07.032>.
- Liu, Yuan Kai et al. (2022). "A unified perspective of seismicity and fault coupling along the San Andreas Fault". In: *Science Advances* 8.8, pp. 1–7. ISSN: 23752548. DOI: [10.1126/sciadv.abk1167](https://doi.org/10.1126/sciadv.abk1167).

- Lloyd, Stuart (1982). "Least squares quantization in PCM". In: *IEEE transactions on information theory* 28.2, pp. 129–137.
- Lohman, R. B. and J. J. McGuire (2007). "Earthquake swarms driven by aseismic creep in the Salton Trough, California". In: *Journal of Geophysical Research: Solid Earth* 112.4, pp. 1–10. ISSN: 21699356. DOI: [10.1029/2006JB004596](https://doi.org/10.1029/2006JB004596).
- Longwell, Chester R (1945). "Low-angle normal faults in the basin-and-range province". In: *Eos, Transactions American Geophysical Union* 26.1, pp. 107–118.
- Lowen, Steven Bradley and Malvin Carl Teich (2005). *Fractal-based point processes*. John Wiley & Sons.
- Madariaga, Raul (1976). "Dynamics of an expanding circular fault". In: *Bulletin of the Seismological Society of America* 66.3, pp. 639–666.
- Mai, P Martin and Gregory C Beroza (2000). "Source scaling properties from finite-fault-rupture models". In: *Bulletin of the Seismological Society of America* 90.3, pp. 604–615.
- Majstorović, Josipa, Sophie Giffard-Roisin, and Piero Poli (2021). "Designing convolutional neural network pipeline for near-fault earthquake catalog extension using single-station waveforms". In: *Journal of Geophysical Research: Solid Earth* 126.7, e2020JB021566.
- Marsan, David and Suleyman S Nalbant (2005). "Methods for measuring seismicity rate changes: a review and a study of how the M w 7.3 landers earthquake affected the aftershock sequence of the M w 6.1 Joshua Tree earthquake". In: *Pure and Applied Geophysics* 162, pp. 1151–1185.
- Martínez-Garzón, Patricia et al. (2021). "Near-fault monitoring reveals combined seismic and slow activation of a fault branch within the istanbul-marmara seismic gap in northwest turkey". In: *Seismological Research Letters* 92.6, pp. 3743–3756. ISSN: 19382057. DOI: [10.1785/0220210047](https://doi.org/10.1785/0220210047).
- Marzorati, Simone et al. (2014). "Very detailed seismic pattern and migration inferred from the April 2010 Pietralunga (northern Italian Apennines) micro-earthquake sequence". In: *Tectonophysics* 610. April 2010, pp. 91–109. ISSN: 00401951. DOI: [10.1016/j.tecto.2013.10.014](https://doi.org/10.1016/j.tecto.2013.10.014). URL: <http://dx.doi.org/10.1016/j.tecto.2013.10.014>.
- McGuire, Jeffrey J., Margaret S. Boettcher, and Thomas H. Jordan (2005). "Erratum: Foreshock sequences and short-term earthquake predictability on East Pacific Rise transform faults (Nature (2005) 434 (457-461))". In: *Nature* 435.7041, p. 528. ISSN: 00280836. DOI: [10.1038/nature03621](https://doi.org/10.1038/nature03621).
- Miller, Stephen A et al. (2004). "Aftershocks driven by a high-pressure CO2 source at depth". In: *Nature* 427.6976, pp. 724–727.
- Mirabella, F et al. (2004). "The Gubbio normal fault (Central Italy): Geometry, displacement distribution and tectonic evolution". In: *Journal of Structural Geology* 26.12, pp. 2233–2249. ISSN: 01918141. DOI: [10.1016/j.jsg.2004.06.009](https://doi.org/10.1016/j.jsg.2004.06.009).
- Mirabella, F et al. (2011). "Tectonic evolution of a low-angle extensional fault system from restored cross-sections in the Northern Apennines (Italy)". In: *Tectonics* 30.6. ISSN: 02787407. DOI: [10.1029/2011TC002890](https://doi.org/10.1029/2011TC002890).
- Mogi, Kiyoo (1963). *Some discussions on aftershocks, foreshocks and earthquake swarms - the fracture of a semi-infinite body caused by an inner stress origin and its relation to the earthquake phenomena*.
- Münchmeyer, Jannes et al. (2022). "Which picker fits my data? A quantitative evaluation of deep learning based seismic pickers". In: *Journal of Geophysical Research: Solid Earth* 127.1, e2021JB023499.

- Nadeau, Robert M, W Foxall, and TV McEvelly (1995). "Clustering and periodic recurrence of microearthquakes on the San Andreas fault at Parkfield, California". In: *Science* 267.5197, pp. 503–507.
- Nadeau, Robert M. and Lane R. Johnson (1998). "Seismological studies at Parkfield VI: moment release rates and estimates of source parameters for small repeating earthquakes". In: *Bulletin of the Seismological Society of America* 88.3, pp. 790–814. ISSN: 00371106.
- Nadeau, Robert M and Thomas V McEvelly (1999). "Fault slip rates at depth from recurrence intervals of repeating microearthquakes". In: *Science* 285.5428, pp. 718–721. ISSN: 00368075. DOI: [10.1126/science.285.5428.718](https://doi.org/10.1126/science.285.5428.718).
- Obara, Kazushige (2002). "Nonvolcanic deep tremor associated with subduction in southwest Japan". In: *Science* 296.5573, pp. 1679–1681.
- Ogata, Yoshihiko, Tokuji Utsu, and Koichi Katsura (1995). "Statistical features of foreshocks in comparison with other earthquake clusters". In: *Geophysical Journal International* 121.1, pp. 233–254.
- Omori, Fusakichi (1894). "On after-shocks". In: *Rep. Imp. Earthq. Inv. Com.* 2, pp. 103–138.
- Ozawa, Shinzaburo et al. (2003). "Characteristic silent earthquakes in the eastern part of the Boso peninsula, Central Japan". In: *Geophysical Research Letters* 30.6.
- Palano, Mimmo (2015). "On the present-day crustal stress, strain-rate fields and mantle anisotropy pattern of Italy". In: *Geophysical Journal International* 200.2, pp. 969–985.
- Passarelli, Luigi et al. (2018). "Scaling and spatial complementarity of tectonic earthquake swarms". In: *Earth and Planetary Science Letters* 482, pp. 62–70. ISSN: 0012821X. DOI: [10.1016/j.epsl.2017.10.052](https://doi.org/10.1016/j.epsl.2017.10.052). URL: <https://doi.org/10.1016/j.epsl.2017.10.052>.
- Passarelli, Luigi et al. (2021). "The source scaling and seismic productivity of slow slip transients". In: *Science Advances* 7.32, pp. 1–12. ISSN: 23752548. DOI: [10.1126/sciadv.abg9718](https://doi.org/10.1126/sciadv.abg9718).
- Pauselli, Cristina et al. (2006). "The crustal structure of the Northern Apennines (Central Italy): An insight by the CROP03 seismic line". In: *American Journal of Science* 306.6, pp. 428–450. ISSN: 00029599. DOI: [10.2475/06.2006.02](https://doi.org/10.2475/06.2006.02).
- Pedregosa, Fabian et al. (2011). "Scikit-learn: Machine learning in Python". In: *the Journal of machine Learning research* 12, pp. 2825–2830.
- Peng, Wei et al. (2021). "Earthquake swarms in Taiwan: A composite declustering method for detection and their spatial characteristics". In: *Earth and Planetary Science Letters* 574, p. 117160. ISSN: 0012821X. DOI: [10.1016/j.epsl.2021.117160](https://doi.org/10.1016/j.epsl.2021.117160). URL: <https://doi.org/10.1016/j.epsl.2021.117160>.
- Peng, Zhigang and Yehuda Ben-Zion (2005). "Spatiotemporal variations of crustal anisotropy from similar events in aftershocks of the 1999 M7.4 İzmit and M7.1 Düzce, Turkey, earthquake sequences". In: *Geophysical Journal International* 160.3, pp. 1027–1043. ISSN: 0956540X. DOI: [10.1111/j.1365-246X.2005.02569.x](https://doi.org/10.1111/j.1365-246X.2005.02569.x).
- Peng, Zhigang and Joan Gomberg (2010). "An integrated perspective of the continuum between earthquakes and slow-slip phenomena". In: *Nature Geoscience* 3.9, pp. 599–607. ISSN: 17520894. DOI: [10.1038/ngeo940](https://doi.org/10.1038/ngeo940). URL: <http://dx.doi.org/10.1038/ngeo940>.
- Peng, Zhigang and Peng Zhao (2009). "Migration of early aftershocks following the 2004 Parkfield earthquake". In: *Nature Geoscience* 2.12, pp. 877–881. ISSN: 17520894. DOI: [10.1038/ngeo697](https://doi.org/10.1038/ngeo697). URL: <http://dx.doi.org/10.1038/ngeo697>.
- Perfettini, H and J-P Avouac (2004). "Postseismic relaxation driven by brittle creep: A possible mechanism to reconcile geodetic measurements and the decay rate of

- aftershocks, application to the Chi-Chi earthquake, Taiwan". In: *Journal of Geophysical Research: Solid Earth* 109.B2.
- Piana Agostinetti, Nicola, Genny Giacomuzzi, and Claudio Chiarabba (2017). "Seismic swarms and diffuse fracturing within Triassic evaporites fed by deep degassing along the low-angle Alto Tiberina normal fault (central Apennines, Italy)". In: *Journal of Geophysical Research: Solid Earth* 122.1, pp. 308–331. ISSN: 21699356. DOI: [10.1002/2016JB013295](https://doi.org/10.1002/2016JB013295).
- Piccinini, Davide et al. (2003). "A microseismic study in a low seismicity area of Italy: The Città di Castello 2000-2001 experiment". In: *Annals of Geophysics* 46.6, pp. 1315–1324. ISSN: 15935213. DOI: [10.4401/ag-3476](https://doi.org/10.4401/ag-3476).
- Piegari, Ester, Marcus Hermann, and Warner Marzocchi (2022). "3D spatial cluster analysis of seismic sequences through density-based algorithms". In: *Geophysical Journal International*.
- Pinzon-Rincon, Laura et al. (2021). "Humming trains in seismology: an opportune source for probing the shallow crust". In: *Seismological Research Letters* 92.2A, pp. 623–635.
- Poli, P et al. (2022). "Volcanic origin of a long-lived swarm in the Central Bransfield Basin, Antarctica". In: *Geophysical Research Letters* 49.1, e2021GL095447.
- Poli, Piero et al. (2020). "The 2020 coronavirus lockdown and seismic monitoring of anthropic activities in Northern Italy". In: *Scientific Reports* 10.1, pp. 1–8. ISSN: 20452322. DOI: [10.1038/s41598-020-66368-0](https://doi.org/10.1038/s41598-020-66368-0). URL: <http://dx.doi.org/10.1038/s41598-020-66368-0>.
- Pondrelli, S. et al. (2002). "European–Mediterranean regional centroid-moment tensors: 1997–2000". In: *Physics of the Earth and Planetary Interiors* 130.1, pp. 71–101. ISSN: 0031-9201. DOI: [https://doi.org/10.1016/S0031-9201\(01\)00312-0](https://doi.org/10.1016/S0031-9201(01)00312-0). URL: <https://www.sciencedirect.com/science/article/pii/S0031920101003120>.
- Prim, Robert Clay (1957). "Shortest connection networks and some generalizations". In: *The Bell System Technical Journal* 36.6, pp. 1389–1401.
- Pucci, Stefano et al. (2003). "Geomorphology of the Gubbio Basin (Central Italy): Understanding the active tectonics and earthquake potential". In: *Annals of Geophysics* 46.5, pp. 837–864. ISSN: 15935213. DOI: [10.4401/ag-3458](https://doi.org/10.4401/ag-3458).
- Ransome, Frederick Leslie, William Harvey Emmons, and George H Garrey (1910). *Geology and ore deposits of the Bullfrog district, Nevada*. 407. US Government Printing Office.
- Reasenber, Paul (1985). "Second-order moment of central California seismicity, 1969–1982". In: *Journal of Geophysical Research: Solid Earth* 90.B7, pp. 5479–5495.
- Reverso, T., D. Marsan, and A. Helmstetter (2015). "Detection and characterization of transient forcing episodes affecting earthquake activity in the Aleutian Arc system". In: *Earth and Planetary Science Letters* 412, pp. 25–34. ISSN: 0012821X. DOI: [10.1016/j.epsl.2014.12.012](https://doi.org/10.1016/j.epsl.2014.12.012). URL: <http://dx.doi.org/10.1016/j.epsl.2014.12.012>.
- Rietbrock, Andreas et al. (1996). "Seismic slip on a low angle normal fault in the Gulf of Corinth: Evidence from high-resolution cluster analysis of microearthquakes". In: *Geophysical Research Letters* 23.14, pp. 1817–1820. ISSN: 00948276. DOI: [10.1029/96GL01257](https://doi.org/10.1029/96GL01257).
- Rigo, A et al. (1996). "A microseismic study in the western part of the Gulf of Corinth (Greece): implications for large-scale normal faulting mechanisms". In: *Geophysical Journal International* 126.3, pp. 663–688.
- Rogers, Garry and Herb Dragert (2003). "Episodic tremor and slip on the Cascadia subduction zone: The chatter of silent slip". In: *Science* 300.5627, pp. 1942–1943.

- Roland, Emily and Jeffrey J McGuire (2009). "Earthquake swarms on transform faults". In: *Geophysical Journal International* 178.3, pp. 1677–1690.
- Rovida, A et al. (2011). "CPTI11, the 2011 version of the Parametric Catalogue of Italian Earthquakes". In: *Milano, Bologna*.
- Ruhl, CJ et al. (2016). "Complex spatiotemporal evolution of the 2008 Mw 4.9 Mogul earthquake swarm (Reno, Nevada): Interplay of fluid and faulting". In: *Journal of Geophysical Research: Solid Earth* 121.11, pp. 8196–8216.
- Ruina, Andy (1983). "Slip instability and state variable friction laws". In: *Journal of Geophysical Research: Solid Earth* 88.B12, pp. 10359–10370.
- Sánchez-Reyes, Hugo et al. (2020). "The imbricated foreshock and aftershock activities of the Balsorano (Italy) M w 4 . 4 normal fault earthquake and implications for earthquake initiation". In: pp. 1–15.
- Schaff, David P and Felix Waldhauser (2005). "Waveform cross-correlation-based differential travel-time measurements at the Northern California Seismic Network". In: *Bulletin of the Seismological Society of America* 95.6, pp. 2446–2461.
- Schmittbuhl, J et al. (2016). "Long-lasting seismic repeaters in the Central Basin of the Main Marmara fault". In: *Geophysical Research Letters* 43.18, pp. 9527–9534.
- Schoenball, Martin and William L Ellsworth (2017). "A Systematic Assessment of the Spatiotemporal Evolution of Fault Activation Through Induced Seismicity in Oklahoma and Southern Kansas". In: *Journal of Geophysical Research: Solid Earth* 122.12, pp. 110–189. ISSN: 21699356. DOI: [10.1002/2017JB014850](https://doi.org/10.1002/2017JB014850).
- Scholz, CH (1968). "The frequency-magnitude relation of microfracturing in rock and its relation to earthquakes". In: *Bulletin of the seismological society of America* 58.1, pp. 399–415.
- Scuderi, MM, Cristiano Collettini, and C Marone (2017). "Frictional stability and earthquake triggering during fluid pressure stimulation of an experimental fault". In: *Earth and Planetary Science Letters* 477, pp. 84–96.
- Seno, Tetsuzo and Tadashi Yamasaki (2003). "Low-frequency tremors, intraslab and interplate earthquakes in Southwest Japan—from a viewpoint of slab dehydration". In: *Geophysical Research Letters* 30.22.
- Serpelloni, E et al. (2005). "Crustal velocity and strain-rate fields in Italy and surrounding regions: New results from the analysis of permanent and non-permanent GPS networks". In: *Geophysical Journal International* 161.3, pp. 861–880. ISSN: 0956540X. DOI: [10.1111/j.1365-246X.2005.02618.x](https://doi.org/10.1111/j.1365-246X.2005.02618.x).
- Shapiro, Sergei A, Ernst Huenges, and Günter Borm (1997). "Estimating the crust permeability from fluid-injection-induced seismic emission at the KTB site". In: *Geophysical Journal International* 131.2, F15–F18.
- Shearer, Peter M (2012). "Space-time clustering of seismicity in California and the distance dependence of earthquake triggering". In: *Journal of Geophysical Research: Solid Earth* 117.B10.
- Shelly, David R (2020). "A high-resolution seismic catalog for the initial 2019 ridge-crest earthquake sequence: Foreshocks, aftershocks, and faulting complexity". In: *Seismological Research Letters* 91.4, pp. 1971–1978. ISSN: 19382057. DOI: [10.1785/0220190309](https://doi.org/10.1785/0220190309).
- Shelly, David R and Kaj M Johnson (2011). "Tremor reveals stress shadowing, deep postseismic creep, and depth-dependent slip recurrence on the lower-crustal San Andreas fault near Parkfield". In: *Geophysical Research Letters* 38.13.
- Shelly, David R and Weston A Thelen (2019). "Anatomy of a caldera collapse: Kīlauea 2018 summit seismicity sequence in high resolution". In: *Geophysical Research Letters* 46.24, pp. 14395–14403.

- Shelly, David R. et al. (2006). "Low-frequency earthquakes in Shikoku, Japan, and their relationship to episodic tremor and slip". In: *Nature* 442.7099, pp. 188–191. ISSN: 14764687. DOI: [10.1038/nature04931](https://doi.org/10.1038/nature04931).
- Sibson, Richard H (1985). "A note on fault reactivation". In: *Journal of Structural Geology* 7.6, pp. 751–754.
- Smith, SAF et al. (2011). "The microstructural character and mechanical significance of fault rocks associated with a continental low-angle normal fault: The Zuccale Fault, Elba Island, Italy". In: *Geological Society, London, Special Publications* 359.1, pp. 97–113.
- Stevens, J et al. (2004). "Analysis and simulation of cavity-decoupled explosions". In: *Proc. 26 Seis. Res. Rev., Orlando, Florida, September 2004. Trends in Nuclear Explosion Monitoring*, pp. 495–502.
- Tan, Yen Joe and David Marsan (2020). "Connecting a broad spectrum of transient slip on the San Andreas fault". In: *Science Advances* 6.33, pp. 1–9. ISSN: 23752548. DOI: [10.1126/sciadv.abb2489](https://doi.org/10.1126/sciadv.abb2489).
- Trugman, Daniel T and Peter M Shearer (2017). "GrowClust: A Hierarchical clustering algorithm for relative earthquake relocation, with application to the Spanish Springs and Sheldon, Nevada, earthquake sequences". In: *Seismological Research Letters* 88.2, pp. 379–391. ISSN: 19382057. DOI: [10.1785/0220160188](https://doi.org/10.1785/0220160188).
- Trugman, Daniel T. et al. (2015). "Synchronous low frequency earthquakes and implications for deep San Andreas Fault slip". In: *Earth and Planetary Science Letters* 424, pp. 132–139. ISSN: 0012821X. DOI: [10.1016/j.epsl.2015.05.029](https://doi.org/10.1016/j.epsl.2015.05.029). URL: <http://dx.doi.org/10.1016/j.epsl.2015.05.029>.
- Tryon, Robert Choate (1939). "Cluster analysis: correlation profile and orthometric (factor) analysis for the isolation of unities in mind and personality. Edwards brother, Incorporated". In: *Ann Arbor*.
- Uchida, Naoki (2019). "Detection of repeating earthquakes and their application in characterizing slow fault slip". In: *Progress in Earth and Planetary Science* 6.1. ISSN: 21974284. DOI: [10.1186/s40645-019-0284-z](https://doi.org/10.1186/s40645-019-0284-z).
- Uchida, Naoki and Roland Bürgmann (2019). "Repeating earthquakes". In: *Annual Review of Earth and Planetary Sciences* 47, pp. 305–332.
- Uchida, Naoki et al. (2003). "Interplate quasi-static slip off Sanriku, NE Japan, estimated from repeating earthquakes". In: *Geophysical Research Letters* 30.15.
- Utsu, Tokuji, Yoshihiko Ogata, et al. (1995). "The centenary of the Omori formula for a decay law of aftershock activity". In: *Journal of Physics of the Earth* 43.1, pp. 1–33.
- Vadacca, Luigi et al. (2016). "On the mechanical behaviour of a low-angle normal fault: The Alto Tiberina fault (Northern Apennines, Italy) system case study". In: *Solid Earth* 7.6, pp. 1537–1549. ISSN: 18699529. DOI: [10.5194/se-7-1537-2016](https://doi.org/10.5194/se-7-1537-2016).
- Valoroso, Luisa et al. (2017). "Mixed-Mode Slip Behavior of the Altotiberina Low-Angle Normal Fault System (Northern Apennines, Italy) through High-Resolution Earthquake Locations and Repeating Events". In: *Journal of Geophysical Research: Solid Earth* 122.12, pp. 210–220. ISSN: 21699356. DOI: [10.1002/2017JB014607](https://doi.org/10.1002/2017JB014607).
- Van Gessel, Serge et al. (2021). "A European Fault Database as a stepping stone towards improved subsurface evaluation of hazards and resources". In: *EGU General Assembly Conference Abstracts*, EGU21–16232.
- VanderPlas, Jacob T (2017). "Understanding the Lomb-Scargle Periodogram". In: DOI: [10.3847/1538-4365/aab766](https://doi.org/10.3847/1538-4365/aab766).
- Vidale, JE et al. (1994). "Variations in rupture process with recurrence interval in a repeated small earthquake". In: *Nature* 368.6472, pp. 624–626.

- Vidale, John E., Katie L. Boyle, and Peter M. Shearer (2006). "Crustal earthquake bursts in California and Japan: Their patterns and relation to volcanoes". In: *Geophysical Research Letters* 33.20, pp. 1–5. ISSN: 00948276. DOI: [10.1029/2006GL027723](https://doi.org/10.1029/2006GL027723).
- Vidale, John E and Peter M Shearer (2006). "A survey of 71 earthquake bursts across southern California: Exploring the role of pore fluid pressure fluctuations and aseismic slip as drivers". In: *Journal of Geophysical Research: Solid Earth* 111.5, pp. 1–12. ISSN: 21699356. DOI: [10.1029/2005JB004034](https://doi.org/10.1029/2005JB004034).
- Vuan, A et al. (2020). "Intermittent Slip along the Alto Tiberina Low-angle Normal Fault in Central Italy". In: DOI: [10.1029/2020GL089039](https://doi.org/10.1029/2020GL089039).
- Ward Jr, Joe H (1963). "Hierarchical grouping to optimize an objective function". In: *Journal of the American statistical association* 58.301, pp. 236–244.
- Wells, D. L. and K. J. Coppersmith (1994). "New empirical relationships among magnitude, rupture length, rupture width, rupture area, and surface displacement". In: *Bulletin - Seismological Society of America* 84.4, pp. 974–1002.
- Wernicke, Brian (1981). "Low-angle normal faults in the Basin and Range Province: nappe tectonics in an extending orogen". In: *Nature* 291, pp. 645–648.
- (1995). "Low-angle normal faults and seismicity: A review". In: *Journal of Geophysical Research: Solid Earth* 100.B10, pp. 20159–20174. ISSN: 0148-0227. DOI: [10.1029/95jb01911](https://doi.org/10.1029/95jb01911).
- Williams, William Thomas and Joyce M Lambert (1959). "Multivariate methods in plant ecology: I. Association-analysis in plant communities". In: *The Journal of Ecology*, pp. 83–101.
- Wilmink, Frederik W and Hilde T Uytterschaut (1984). "Cluster analysis, history, theory and applications". In: *Multivariate Statistical Methods in Physical Anthropology: A Review of Recent Advances and Current Developments*, pp. 135–175.
- Wu, Chunquan et al. (2015). "Spatial-temporal variation of low-frequency earthquake bursts near Parkfield, California". In: *Geophysical Journal International* 202.2, pp. 914–919. ISSN: 1365246X. DOI: [10.1093/gji/ggv194](https://doi.org/10.1093/gji/ggv194).
- Yao, Dongdong et al. (2017). "Detailed spatiotemporal evolution of microseismicity and repeating earthquakes following the 2012 Mw 7.6 Nicoya earthquake". In: *Journal of Geophysical Research: Solid Earth* 122.1, pp. 524–542.
- Zaliapin, Ilya and Yehuda Ben-Zion (2013a). "Earthquake clusters in southern California I: Identification and stability". In: *Journal of Geophysical Research: Solid Earth* 118.6, pp. 2847–2864. ISSN: 21699356. DOI: [10.1002/jgrb.50179](https://doi.org/10.1002/jgrb.50179).
- (2013b). "Earthquake clusters in southern California II: Classification and relation to physical properties of the crust". In: *Journal of Geophysical Research: Solid Earth* 118.6, pp. 2865–2877.
- Zaliapin, Ilyar et al. (2008). "Clustering analysis of seismicity and aftershock identification". In: *Physical Review Letters* 101.1, pp. 4–7. ISSN: 00319007. DOI: [10.1103/PhysRevLett.101.018501](https://doi.org/10.1103/PhysRevLett.101.018501).
- Zhang, Qiong and Peter M. Shearer (2016). "A new method to identify earthquake swarms applied to seismicity near the San Jacinto Fault, California". In: *Geophysical Journal International* 205.2, pp. 995–1005. ISSN: 1365246X. DOI: [10.1093/gji/ggw073](https://doi.org/10.1093/gji/ggw073).
- Zhu, Weiqiang and Gregory C Beroza (2019). "PhaseNet: a deep-neural-network-based seismic arrival-time picking method". In: *Geophysical Journal International* 216.1, pp. 261–273.